LÍVIA PUGENS MATTE

Unraveling the influence of the CeO_{2-x} ($0 \leq x \leq 0.5$) properties on the reactivity of the Cu-CeO_{2-x} nanoparticles towards the CO oxidation reaction

Porto Alegre, RS, Brazil
December, 2019.

LÍVIA PUGENS MATTE

Desvendando a influência das propriedades do CeO_{2-x} ($0 \leq x \leq 0,5$) na reatividade de nanopartículas de Cu-CeO_{2-x} na reação de oxidação de CO

Dissertação realizada sob a orientação do Prof. Dr. Fabiano Bernardi e da Profª. Drª. Fernanda Poletto, apresentada no Instituto de Física da Universidade Federal do Rio Grande do Sul, em preenchimento parcial dos requisitos para a obtenção do título de Mestre em Física.

Universidade Federal do Rio Grande do Sul

Instituto de Física

Programa de Pós-Graduação

Orientador: Prof. Dr. Fabiano Bernardi

Co-Orientadora: Profª. Drª. Fernanda Poletto

Porto Alegre, RS, Brasil.
Dezembro, 2019.

ACKNOWLEDGEMENT

I would like to thank to everyone that contributed to this work, in special:

Prof. Fabiano Bernardi for his advisement, teachings, motivation, patience, dedication and friendship.

Prof. Fernanda Poletto for all the constructive discussions, teachings, patience and friendship.

Prof. Fernanda Poletto, Francielle O. Lobato and Prof. Jairton Dupont from IQ-UFRGS for synthesizing the nanoparticles used in this work.

CMM/UFRGS, for the dedication and help of its staff during the MET measures.

Mr. Otelo José Machado, for the quality of the XRD measurements. LCN/UFRGS, for the SEM-EDS measurements. LNLS/CNPEM for providing access to the Brazilian Synchrotron in order to perform the XAS measurements presented in this work and the financial support. The LNLS staff for the assistance during the measurements. LME/CNPEM for the operation training of the xxx TE microscope and possibility of using for the HRTEM measurements. It's staff for all the planing and assistance during the measurements. The LNNano/CNPEM and its staff for the XPS measurements.

The Coordenação de Aperfeiçoamento de Pessoal de Nível Superior (Capes) for the Master's fellowship.

Also, I thank my parents for providing me with unfailing support and continuous encouragement. My brother, for teaching me self-confidence and my sister for teaching me the value of life. I'd also like to thank my grandparents for encouraging me to study always and teaching me to focus on the good things. Wallace for his support and love. Carol, Alef and Anderson for the good conversations and friendship. The Physics of Nanostructures Laboratory group for all the discussions, friendship and support.

To my grandparents

RESUMO PARA PÚBLICO LEIGO

O monóxido de carbono (CO) é um gás tóxico, que não possui cor, cheiro ou gosto. Este gás é formado a partir da queima de matéria orgânica, como gasolina e vegetação. O excesso de CO na atmosfera, causado pela ação humana, é um sério problema ambiental. Para eliminá-lo antes de chegar na atmosfera, é possível transformá-lo em gás carbônico, que é menos tóxico, através da sua reação com oxigênio. No entanto, essa reação normalmente é muito lenta. Para acelerá-la, deve-se utilizar compostos conhecidos como catalisadores, que aumentam a velocidade de reações sem serem degradados nesse processo. Há vários tipos de compostos que podem atuar como catalisadores. Na indústria, a reação entre oxigênio e CO é catalisada por metais nobres, tais como platina, paládio e ródio. Isto torna a transformação de CO em gás carbônico muito cara. Alternativas mais baratas vem sendo buscadas. Uma delas é utilizar nanopartículas de cobre como catalisadores. Nanopartículas são estruturas muito pequenas, invisíveis a olho nu. O desempenho das nanopartículas de cobre aumenta quando são colocadas na superfície de nanopartículas de óxido de cério, o qual é um material que compõe alguns tipos de cerâmicas. Nanopartículas de óxido de cério possuem a propriedade de doar e captar oxigênio. A facilidade em captar e doar oxigênio depende de características das nanopartículas de óxido de cério, tais como seu tamanho, quantidade e volume de poros em sua superfície, além de suas propriedades eletrônicas. Estas estão relacionadas à quantidade de elétrons que o elemento cério possui no início da reação, que pode variar dependendo da forma como as nanopartículas de óxido de cério foram preparadas. No catalisador de nanopartículas de cobre misturadas com nanopartículas de óxido de cério, a reação entre oxigênio e CO ocorre na superfície do cobre. O principal objetivo deste estudo foi investigar quais características deste sistema tornam-no mais efetivo para transformar CO em gás carbônico. Com isso, espera-se desenvolver catalisadores mais baratos e eficientes no futuro. Observou-se que uma maior eficiência (ou seja, mais gás carbônico formado a partir de CO) é alcançada quando o óxido de cério tem maior facilidade para doar e receber oxigênio e quando o cobre está na forma de óxido de cobre (CuO), que é um estado do cobre bastante comum em certos minérios. O oxigênio que reage com o CO é doado pelo CuO, que assume o estado Cu_2O devido a isso. Nesse processo, após doar seu oxigênio para o CO, o cobre na forma Cu_2O capta oxigênio doado pelo óxido de

cério para voltar à forma CuO. Quanto mais CuO no catalisador, mais eficiente é a transformação de CO em gás carbônico. Além disso, foi observado que o arranjo dos átomos das nanopartículas de cobre, durante a reação, também influencia na eficiência deste sistema. Nas nanopartículas, os átomos se ordenam espacialmente de modo a formar camadas ao redor dos átomos vizinhos. Nestas camadas, todos os átomos estão, aproximadamente, à mesma distância de um átomo central. Por exemplo, no CuO, os átomos de cobre possuem ao seu redor uma camada de átomos de oxigênio, e a uma distância um pouco maior, uma camada de átomos de cobre. Foi observado que o catalisador torna-se mais eficiente quando aumenta o número de átomos nas camadas em torno do átomo de cobre, e quando estas camadas estão mais desordenadas no que se refere às posições dos átomos. Além disso, há um aumento da reatividade quando a camada ocupada por átomos de oxigênio está mais próxima dos átomos de cobre. As nanopartículas de óxido de cério empregadas neste estudo mostraram-se superiores àquelas de origem comercial, devido às suas características particulares que permitem maior facilidade de captação e doação de oxigênio em sua superfície. O estudo desenvolvido nesta dissertação de mestrado poderá futuramente auxiliar no desenvolvimento de catalisadores mais baratos e eficientes para a reação de CO com oxigênio.

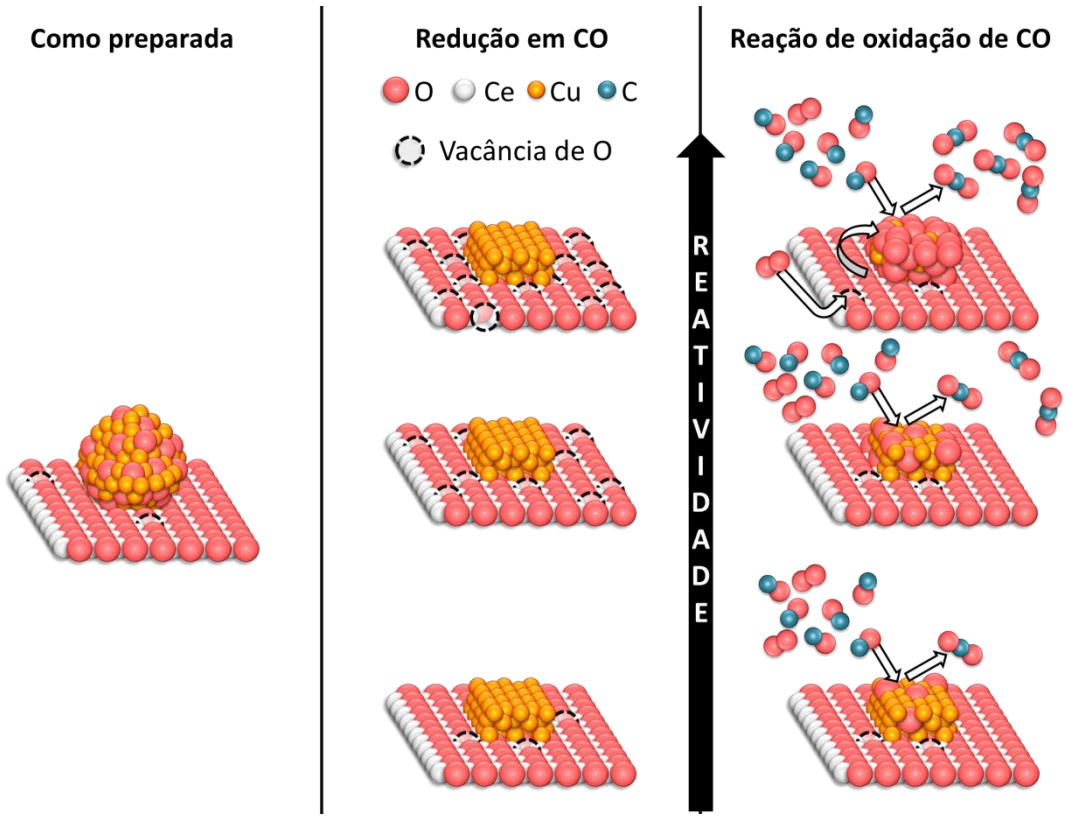

ABSTRACT

Carbon monoxide is a poisonous, odor- and colorless gas, formed by incomplete combustion of organic matter, such as fossil fuels and vegetation. An efficient way to reduce the emission of this gas in the atmosphere is by the use of an oxidation reaction, typically performed with the use of catalysts. The catalysts currently used contain noble metals, such as Pt, Pd and Rh. Cheaper catalysts, like Cu-based catalysts, with higher efficiencies would attract attention from industries. This work presents the study about the influence of the electronic and structural properties of CeO_{2-x} ($0 \leq x \leq 0.5$) nanoparticles on the reactivity of Cu-CeO_{2-x} nanoparticles in the CO oxidation reaction. Cu nanoparticles were mixed with CeO_{2-x} nanoparticles showing different properties. A commercial standard of CeO_{2-x} was also used for comparison. The control of electronic and structural properties of the CeO_{2-x} nanoparticles was obtained by changing the synthetic parameters of the precipitation method, like the solvent (type and concentration) and the temperature of synthesis. The as-prepared Cu-CeO_{2-x} nanoparticles were characterized by TEM (Transmission Electron Microscopy), EDS (Energy Dispersive Spectroscopy), XRD (X-Ray Diffraction) and XPS (X-Ray Photoemission Spectroscopy). After, the nanoparticles were heated to 400 °C under a reductive CO atmosphere and then cooled to 250 °C or 150 °C, where the CO oxidation reaction occurred. *In situ* XAS (X-ray Absorption Spectroscopy) and *in situ* time-resolved XAS measurements at the Cu K and Ce L_3 edges were performed during reduction and CO oxidation reaction and the reactivity towards CO oxidation was studied by time-resolved Mass Spectrometry measurements. The morphology changes in the Cu nanoparticles after reduction treatment were probed by XPS and High Resolution TEM (HRTEM) techniques. It was observed that the Cu nanoparticles spread over the CeO_{2-x} surface during reduction treatment, then changing the shape. Moreover, it was observed that the higher reactivity towards CO oxidation reaction the higher the Ce(III) fraction during the reduction treatment, the higher CuO fraction during CO oxidation reaction and the lower the Ce(III) fraction during CO oxidation reaction. The local atomic order around Cu atoms during CO oxidation reaction also influences on the reactivity, which is higher for bigger Cu-O and Cu-Cu coordination numbers and Debye-Waller factors and shorter Cu-O distances. It was demonstrated that the CO oxidation reaction occurs with the CO adsorption at the CuO nanoparticles, where it is oxidized to CO_2. Then the CeO_{2-x} nanoparticles transfer O to the Cu

nanoparticles and are re-oxidized by the O_2 atmosphere. Finally, it was observed an improved reactivity in the Cu-CeO_{2-x} nanoparticles containing the synthesized CeO_{2-x} nanoparticles when compared to the nanoparticles containing the CeO_{2-x} commercial standard, where the reactivity can be tuned by the synthetic parameters used.

RESUMO

O monóxido de carbono é um gás tóxico, inodoro e incolor, formado pela combustão incompleta de matéria orgânica, como combustíveis fósseis e vegetação. Uma maneira eficiente de reduzir a emissão desse gás na atmosfera é pelo uso de uma reação de oxidação, normalmente realizada com o uso de catalisadores. Os catalisadores usados atualmente contêm metais nobres, como Pt, Pd e Rh. Catalisadores mais baratos, como catalisadores à base de Cu, com maior eficiência atrairiam a atenção das indústrias. Este trabalho apresenta o estudo sobre a influência das propriedades eletrônicas e estruturais das nanopartículas de CeO_{2-x} ($0 \leq x \leq 0,5$) na reatividade das nanopartículas de Cu-CeO_{2-x} na reação de oxidação do CO. Nanopartículas de Cu foram misturadas com nanopartículas de CeO_{2-x} que apresentam diferentes propriedades. Um padrão comercial foi utilizado para comparação. O controle das propriedades eletrônicas e estruturais das nanopartículas de CeO_{2-x} foi obtido pela mudança dos parâmetros de síntese do método de precipitação, como o solvente (tipo e concentração) e a temperatura de síntese. As nanopartículas de Cu-CeO_{2-x} preparadas foram caracterizadas por TEM (Microscopia Eletrônica de Transmissão), EDS (Espectroscopia Dispersiva em Energia), XRD (Difração de Raios-X) e XPS (Espectroscopia de Fotoemissão por Raios-X). Após, as nanopartículas foram aquecidas a 400 °C sob uma atmosfera redutora de CO e, em seguida, resfriadas a 250 °C ou 150 °C, onde a reação de oxidação de CO ocorreu. As medidas de XAS (Espectroscopia de Absorção de Raios-X) *in situ* e XAS *in situ* resolvida no tempo nas bordas K do Cu e L_3 do Ce foram realizadas durante redução e reação de oxidação de CO e a reatividade na reação de oxidação de CO foi estudada por medidas de Espectrometria de Massas resolvidas no tempo. As alterações morfológicas nas nanopartículas de Cu após tratamento de redução foram investigadas pelas técnicas de XPS e TEM de Alta Resolução (HRTEM). As nanopartículas de Cu se espalharam sobre a superfície de CeO_{2-x} durante o tratamento de redução, alterando, assim, a forma. Além disso, observou-se que quanto maior a reatividade na reação de oxidação de CO, maior a fração de Ce (III) durante o tratamento de redução, maior a fração de CuO durante a reação de oxidação do CO e menor a fração de Ce (III) durante a reação de oxidação de CO. A ordem atômica local em torno dos átomos de Cu durante a reação de oxidação de CO também influencia na reatividade, que é maior para números de coordenação e fatores de Debye-Waller Cu-O e Cu-Cu maiores e distâncias Cu-O menores. Foi demonstrado que a reação de oxidação do CO ocorre com a

adsorção de CO nas nanopartículas de CuO, onde é oxidado formando CO_2. Em seguida, as nanopartículas de CeO_{2-x} transferem O para as nanopartículas de Cu e são reoxidadas pelo O_2 da atmosfera. Finalmente, foi observada uma melhor reatividade nas nanopartículas de Cu-CeO_{2-x} contendo as nanopartículas de CeO_{2-x} sintetizadas quando comparadas às nanopartículas que contêm o padrão comercial de CeO_{2-x}, onde a reatividade pode ser ajustada pelos parâmetros de síntese utilizados.

CONTENTS

ABSTRACT VII
RESUMO IX
1. INTRODUCTION 26
2. LITERATURE REVIEW 27
2.1 Carbon monoxide (CO) 27
2.2 Catalysts.. 29
2.3 Catalysts used in the CO oxidation reaction 32
2.4 CO oxidation reaction on CeO_{2-x} nanoparticles 35
2.5 CO oxidation reaction on metallic nanoparticles supported on CeO_{2-x} 38
3. ANALYSIS TECHNIQUES 44
3.1 Transmission Electron Microscopy (TEM) 44
3.2 X-Ray Diffraction (XRD) 47
3.3 X-Ray Photoelectron Spectroscopy (XPS) 54
3.4 Mass Spectrometry 61
3.5 Synchrotron Radiation 63
3.6 X-Ray Absorption Spectroscopy (XAS) 65
3.6.1 X-Ray Absorption Near Edge Structure (XANES) 68
3.6.2 Extended X-Ray Absorption Fine Structure (EXAFS) 70
4. EXPERIMENTAL DESCRIPTION 77
4.1 Synthesis of the nanoparticles 77
4.2 EDS Compositional Maps 80
4.3 TEM measurements 80
4.4 XRD measurements 81
4.5 XPS measurements 82
4.6 Time-resolved Mass Spectrometry measurements 83
4.7 *In situ* time-resolved XANES measurements 84
4.8 *In situ* EXAFS measurements 86
5. RESULTS AND DISCUSSION 88
5.1 Characterization of the as-prepared nanoparticles 88
5.1.1 TEM measurements 88
5.1.2 EDS Compositional Maps 90

5.1.3 XRD measurements 92
5.1.4 XPS measurements 95
5.1.5 XANES measurements 99
5.2 Characterization of the nanoparticles during and after the CO oxidation reaction 101
5.2.1 Time-resolved Mass Spectrometry measurements 101
5.2.2 *In situ* time-resolved XANES measurements 105
5.2.3 *In situ* EXAFS measurements 115
5.2.4 XPS measurements 120
5.2.5 HRTEM measurements 125
5.3 Atomic model for the CO oxidation reaction of Cu-CeO_{2-x} nanoparticles 127
6. CONCLUSIONS AND PERSPECTIVES 130
BIBLIOGRAPHY 131

LIST OF FIGURES

Figure 2.1: Schematic representation of the energy diagram indicating the activation energy for the CO oxidation reaction. The dotted region represents the reaction without catalyst and the solid line represents the reaction with a Pt catalyst. Adapted from [16]. 30

Figure 2.2: (a) Schematic representation of the possible active sites of a catalyst where the atoms are represented by cubes. (b) HRTEM image from $Ce_{0.5}Zr_{0.5}O_2$ crystals, presenting defect regions and possible active sites [17]..... 31

Figure 2.3: Schematic representation of a Three Way Catalyst used in car exhaust, adapted from [21]. 33

Figure 2.4: Schematic representation of the CO oxidation mechanism over metals from the platinum group [22]. 34

Figure 2.5 Schematic representation of the *Mars-van Krevelen* mechanism for the CO oxidation reaction on systems composed by Cu-CeO_2 nanoparticles [36]..... 39

Figure 3.1: Comparison between the schematic representation of the optical microscope (on the left) and electronic microscope (on the right) [59]..... 44

Figure 3.2: Example of a TEM image in the bright field mode of Au-Co nanoparticles, where the core region contains Au atoms while the shell, Co atoms [61]. 46

Figure 3.3: Schematic representation of X-ray diffraction phenomenon in a crystalline material [63]. 48

Figure 3.4: Schematic representation of diffractograms from a crystalline and an amorphous material [64]..... 49

Figure 3.5: Schematic representation of a conventional X-ray diffractometer [64]..... 52

Figure 3.6: Schematic representation of an X-ray source where the electrons are emitted by a tungsten filament and accelerated towards the metallic target, where they collide with the material, emitting X-rays [65]. 53

Figure 3.7: X-ray spectra coming from a Mo X-ray source as a function of the

operational voltage of the X-ray tube [65]. 54

Figure 3.8: Schematic representation of the photoelectron effect where an incoming photon transfers its energy to an inner electron with a binding energy (E_{B2}). The electron is then emitted from the atom with a given kinetic energy (E_{k2}) and enters into the analyzer with a kinetic energy (E_k^a) which depends on the X-ray energy (hν), the binding energy of the electron and the work function (φ_{an}) of the analyzer, adapted from [66]. 55

Figure 3.9: Comparison of the long scan spectra of Cu-CeO_2 nanoparticles using two different X-ray sources. 56

Figure 3.10: XPS spectra at the Cu 2p region of (a) Cu(0) and (b) CuO standards [67]. 58

Figure 3.11: Inelastic mean free path of the photoelectrons in a solid as a function of the kinetic energy of the emitted photoelectron [68]..... 59

Figure 3.12: Schematic representation of a HSA analyzer where only electrons with a specific kinetic energy arrive at the detector [71]. 61

Figure 3.13: Mass spectrum of the CO_2 molecule [72]. 62

Figure 3.14: Schematic representation of a mass spectrometer equipment [74]. 63

Figure 3.15: Schematic representation of the main components of a synchrotron light source [75]. 64

Figure 3.16: XAS spectrum at the Cu K edge of a Cu(0) standard sample. 67

Figure 3.17: Schematic representation of the DXAS-LNLS beamline showing the optical system, a curved Si monochromator and a CCD detector [77]. 68

Figure 3.18: Comparison between XANES spectra measured at the Cu K edge for different Cu compounds. 69

Figure 3.19: Schematic representation of the photoelectron backscattering process by the neighboring atoms [79]. 71

Figure 3.20: XAS measurements at the Kr K edge for a Kr sample in the gas, liquid and solid phase [75]..... 71

Figure 3.21: (a) XAS measurement at the Cu K edge for a Cu(0) standard (μ(E)) and the calculated single atom contribution (μ_0(E)), (b) the respective EXAFS oscillations and (c) Fourier Transform. 72

Figure 3.22: Schematic representation of (a) one-dimensional and (b) two-dimensional muffin-tin potential. The atoms are represented by a symmetrically spherical potential, with a constant potential in the region between the atoms [78]. 74

Figure 3.23: Example of the different scattering paths the photoelectron can take including single- and multiple-scattering paths. 75

Figure 4.1: Pore size distribution of the CeO_{2-x} (low TR), CeO_{2-x} (high TR) and CeO_{2-x} (std) nanoparticles, obtained from the BET measurements, adapted from [34]. 79

Figure 4.2: Schematic representation of method used for the mixture of the Cu and CeO_{2-x} nanoparticles using an ultrasonic bath. 80

Figure 4.3: Schematic representation of the sequential thermal treatment applied to the Cu-CeO_{2-x} nanoparticles. 84

Figure 5.1 (a) and (c) TEM image and the corresponding (b) and (c) size distribution histogram of the Cu nanoparticles from the (a) and (b) non-supported Cu and (c) and (d) Cu-CeO_{2-x} (low TR) nanoparticles. 89

Figure 5.2: TEM image of the Cu nanoparticles supported on a CeO_{2-x} agglomerate for the Cu-CeO_{2-x} (high TR) nanoparticles. 90

Figure 5.3: Ce (on the left) and Cu (middle) compositional maps and a typical EDS spectrum (on the right) for the (a) Cu-CeO_{2-x} (low TR); (b) Cu-CeO_{2-x} (high TR) and (c) Cu-CeO_{2-x} (std) nanoparticles. 91

Figure 5.4: XRD diffractograms and the respective Rietveld refinement, presented as a solid black line, obtained for the Cu-CeO_{2-x} (low TR) (red), Cu-CeO_{2-x} (high TR) (blue) and Cu-CeO_{2-x} (std) (green) nanoparticles. 92

Figure 5.5: XPS long scan spectra of the as-prepared Cu-CeO_{2-x} (low TR), Cu-CeO_{2-x} (high TR) and Cu-CeO_{2-x} (std) nanoparticles, measured using Al Kα X-ray source (hν = 1486.7 eV). 95

Figure 5.6: Ce 3d XPS spectra for the as-prepared Cu-CeO_{2-x} nanoparticles. The black

points represent the Shirley background used, the black solid line total the fit performed using the dark gray (corresponding to Ce(IV) component) and light gray (representing the Ce(III) component) peaks. 96

Figure 5.7: Cu $2p_{3/2}$ XPS spectra of the as-prepared Cu-CeO_{2-x} (low TR), Cu-CeO_2.x (high TR) and Cu-CeO_2.x (std) nanoparticles. The black points represent the Shirley background, the black solid line the fit obtained, the dark gray solid line the Cu(I) component, the light gray solid line the Cu(II) component and the brown solid line the Cu $2p_{3/2}$ satellites. 98

Figure 5.8: XANES spectra measured at the Cu K edge for the as-prepared nanoparticles and Cu standards (CuO, $Cu(OH)_2$, Cu-Cl and Cu(0)). 99

Figure 5.9: Time-resolved Mass Spectrometry measurements of the CO_2 production during the CO oxidation reaction at 250 °C for different nanoparticles. The CO_2 current signal was normalized by sum of the CO andCO_2 signal measured at the same time and the CuO-CeO_2 mass used during the measurement. The time scale meaning is described in Figure 4.1 and corresponds to the CO oxidation reaction period. 102

Figure 5.10: Time-resolved Mass Spectrometry measurements of the CO_2 production during the CO oxidation reaction at 150 °C for different nanoparticles. The CO_2 current signal was normalized by the sum of the CO and CO_2 signal measured at the same time and the CuO-CeO_2 mass used during the measurement. The time scale meaning is described in Figure 4.1 and corresponds to the CO oxidation reaction period. 104

Figure 5.11: (a) *In situ* time-resolved XANES spectra measured at the Ce L_3 edge of the Cu-CeO_{2-x} (low TR) nanoparticles during the full thermal treatment applied. The spectra in orange, brown and dark green represent the heating treatment in CO atmosphere, the isothermal reduction treatment in CO atmosphere and the isothermal CO oxidation reaction in CO + ½ O_2 atmosphere, respectively. (b) Typical XANES spectrum at the Ce L_3 edge and the respective fitting for the CeO_{2-x} (low TR) nanoparticles at 400 °C exposed to the CO reducing atmosphere, and the CeO_2 and $CeOHCO_3$ standards spectra, related to the Ce(IV) and Ce(III) oxidation states, respectively. (c) Time evolution of the Ce(III) fraction for the nanoparticles as a function of the time, related to the temperature and atmosphere used as presented in the Figure 4.3. The region filled with diagonal lines refers to the heating (diagonal lines increasing to the right) and cooling (diagonal lines increasing to the left) under CO atmosphere. The areas filled with solid colors refers to the isothermal processes related to the reduction at 400 °C

under CO atmosphere (gray area) and the CO oxidation reaction at 250 °C and 150 °C under CO + ½ O_2 atmosphere (white area). 106

Figure 5.12: (a) Typical *in situ* time-resolved XANES spectra measured at the Cu K edge of the Cu-CeO_{2-x} (low TR) nanoparticles during the full thermal treatment applied. The spectra in orange, brown and dark green represent the heating treatment in CO atmosphere, the isothermal reduction treatment in CO atmosphere and the isothermal CO oxidation reaction in CO + 1/2 O_2 atmosphere, respectively. (b) XANES measurement at the Cu K edge and the respective fitting for the as-prepared Cu-CeO_{2-x} (low TR) nanoparticles and the Cu, CuO, Cu-Cl and $Cu(OH)_2$ standard spectra. 110

Figure 5.13: Time evolution of the (a) CuO, (b) Cu_2O and (c) Cu(0) compounds fractions obtained from the fit of the time-resolved *in situ* XANES spectra measured at the Cu K edge. The region filled with diagonal lines refers to the heating (diagonal lines increasing to the right) and cooling (diagonal lines increasing to the left) under CO atmosphere. The areas filled with solid colors refers to the isothermal process related to the reduction at 400 °C under CO atmosphere (gray area) and the CO oxidation reaction at 250 °C and 150 °C under CO + ½ O_2 atmosphere (white area). 111

Figure 5.14: Typical time-evolution of the Fourier Transform obtained from the EXAFS oscillations of the *in situ* XAS spectra measured at the Cu K edge during reduction treatment at 400 ^oC and CO oxidation reaction at (a) 250 ^oC and (b) 150 ^oC for the Cu-CeO_{2-x} (low TR) nanoparticles. 115

Figure 5.15: EXAFS oscillations ((a) and (c)) and the corresponding Fourier Transforms ((b) and (d)) at the Cu K edge during reduction treatment ((a) and (b)) and CO oxidation reaction ((c) and (d)) at 250 °C..... 117

Figure 5.16: Ce 3d XPS spectra for the Cu-CeO_{2-x} nanoparticles after reduction treatment. The black points represent the Shirley background used, the black solid line the total fit performed using the dark gray (corresponding to Ce(IV) component) and light gray (corresponding to the Ce(III) component) peaks. 121

Figure 5.17: Cu $2p_{3/2}$ XPS spectra of the Cu-CeO_{2-x} (low TR), Cu-CeO_2-x (high TR) and Cu-CeO_2-x (std) nanoparticles after reduction treatment. The black points represent the Shirley background, the black solid line the fit obtained, the dark gray solid line the Cu(I) component, the light gray solid line the Cu(II) component and the brown solid line the Cu $2p_{3/2}$ satellites..... 123

Figure 5.18: (a) HRTEM and (b) EDS linescan measurements performed in the Cu-CeO_{2-x} (std) nanoparticles after the reduction treatment under CO atmosphere for 30 min at 400 °C. The red arrow presented in (a) represent the line scan and direction of the EDS measurements. (c) Representation of the CeO_{2-x} nanoparticles, in blue, and Cu nanoparticle, in orange. 126

LIST OF TABLES

Table 2.1: WHO guidelines for CO exposure, adapted from [4]. 28

Table 4.1: Main electronic and structural characteristics of the synthesized CeO_{2-x} nanoparticles. The uncertainty associated to the specific surface area and pore volume values are 5 m^2g^{-1} and 0.002 cm^3g^{-1}, respectively. The typical uncertainty associated to the Ce(III) fraction values is around 10% of the Ce(III) fraction value. Adapted from [34]. 78

Table 5.1: Weight percent value of the CuO and NaCl compounds present in the samples. The estimated error for this analysis is 20% of the value obtained. 92

Table 5.3: Comparison between the mean diameter obtained by TEM and the crystallite size obtained by XRD analysis. The typical uncertainty associated to the XRD analysis is around 5% of the values obtained. 93

Table 5.2: Lattice parameter (*a*) of the CeO_{2-x} crystalline phase obtained from the Rietveld refinement and Ce(III) fraction obtained by XRD analysis. The estimated error for the Ce(III) fraction is around 5 % of the obtained values. 94

Table 5.4: Ce(III) fraction at the surface of the as-prepared nanoparticles obtained from the Ce 3d XPS spectra. The typical uncertainty associated to the analysis is around 10% of the values obtained. 97

Table 5.5: Percentage of the chemical components used in the fitting of the Cu $2p_{3/2}$ XPS region for the as-prepared Cu-CeO_{2-x} nanoparticles. 98

Table 5.6: Percentage of the chemical components of the as-prepared Cu-CeO_{2-x} nanoparticles obtained from the XANES measurements at the Cu K edge. The typical uncertainty associated to the XANES results is around 10% of the value obtained. ... 100

Table 5.7: Parameters obtained from the quantitative analysis of the EXAFS data for the Cu-CeO_{2-x} nanoparticles measured at the Cu K edge during reduction treatment at 250 °C. 118

Table 5.8: Parameters obtained from the quantitative analysis of the EXAFS data for the Cu-CeO_{2-x} nanoparticles measured at the Cu K edge during CO oxidation reaction at 250 °C. 119

Table 5.9: Ce(III) fraction at the surface of the Cu-CeO_{2-x} nanoparticles obtained from the Ce 3d XPS spectra after reduction treatment. The typical uncertainty associated to the analysis is around 10% of the values obtained. 122

Table 5.10: Percentage of the chemical components used in the fitting of the Cu $2p_{3/2}$ XPS region for the Cu-CeO_{2-x} nanoparticles after reduction treatment. 123

Table 5.11: (Cu 2p)/(Ce 3d) ($\lambda_{IMFP} \approx 11$ Å) and (Cu 3p)/(Ce 4d) ($\lambda_{IMFP} \approx 22$ Å) normalized ratios obtained from the XPS measurements of the as-prepared and after reduction treatment Cu-CeO_{2-x} nanoparticles. 124

LIST OF SYMBOLS AND ABBREVIATIONS

*	Oxygen ions
$\square^{2-}$	Charged oxygen vacancy
a	Absorbing atom
a	Lattice parameter
AF	Absorption Factor
arb. un.	Arbitrary units
$\vec{B}$	Magnetic field
BET	Brunauer-Emmett-Teller techniques
BF	Bright Field
BN	Boron nitride
c	Velocity of light
CAE	Constant Analyzer Energy mode
CCD	Charge-Coupled Devise
Cetesb	Companhia Ambiental do Estado de São Paulo
CMA	Cylindrical Mirror Analyzer
CMM	Centro de Microscopia e Microanálise
CNPEM	Centro Nacional de Pesquisa em Energia e Materiais
CRR	Constant Retard Ratio mode
d	Interplanar distance
D	Particle's mean diameter
DRIFTS	Diffuse Reflectance Infrared Fourier Transform
DXAS	Dispersive X-ray Absorption Spectroscopy
e	Charge of the electron
ê	Polarization vector

E_b	Binding energy
E_k	Kinetic energy
$\hat{e}_r$	Unit vector in the radial direction
EDS	Energy Dispersive Spectroscopy
EPR	Electron Paramagnetic Resonance
EXAFS	Extended X-Ray Absorption Fine Structure
$\|f\rangle$	Final state of the atom
F_{hkl}	Structure factor for a given hkl plane
f_j	Atomic scattering factor
$\overrightarrow{F_m}$	Force
F_x	X-ray flux on the sample
FIB	Focused Ion Beam
G	Green function
FWHM	Full Width at Half Maximum
$\hbar$	Reduced Planck constant
$\mathcal{H}$	Hamiltonian
HRTEM	High-Resolution Transmission Electron Microscopy
HSA	Hemispherical Sector Analyzer
hν	Photon's energy
$\|i\rangle$	Initial state of the atom
I	Intensity
I_o	Incident beam intensity
ICDS	Inorganic Crystal Structure Database
Im(*f*)	Imaginary part of the *f* function
IRF	Instrumental resolution function
j	Lattice atom
k	Photoelectron's wave vector

K	Form factor
$\vec{K}$	Difference between the incident and diffracted wave vectors
LCA	Linear Combination Analyzer
LCN	Laboratório de Conformação Nanométrica
LF	Lorentz factor
LNLS	Laboratório Nacional de Luz Sincrotron
LNNano	Brazilian Nanotechnology National Laboratory
m_e	Electron mass
m_i	Ion mass
n(z)	Atomic concentration at the z depth
N_j	Coordination number
NAP-XPS	Near Ambiente Pressure X-Ray Photoelectron Spectroscopy
NTP	Normal Temperature and Pressure
p	Multiplicity factor
P	Pressure
q	Charge of the particle
R	Radius
$\overrightarrow{R_j}$	Position vector of the jth atom
R-factor	Indicates the quality of the XAS fit
S_o^2	Amplitude reduction factor
$S(E_k)$	Analyzer efficiency
SEM	Scanning Electron Microscopy
SMSI	Strong Metal Support Interaction
Std	Standard
STEM	Scanning Transmission Electron Microscopy
t	Sample thickness

TEM	Transmission Electron Microscopy
TPR	Temperature Programmed Reduction
TR	Temperature of Reduction
TWC	Three Way Catalyst
$\vec{v}$	Velocity
V	Electrostatic potential
WGS	Water Gas Shift reaction
WHO	World Health Organization
wt.	Weight
XAFS	X-Ray Absorption Fine Structure
XANES	X-ray Absorption Near Edge Structure
XAS	X-Ray Absorption Spectroscopy
XPS	X-Ray Photoelectron Spectroscopy
XRD	X-Ray Diffraction
XRF	X-Ray Fluorescence
z	Depth below the surface where the photoelectron is emitted
α	Angle between the direction of the incident beam and the emission of the photoelectron
β	Full width at half maximum
β_{nl}	Angular asymmetry factor
δ_j	Phase shift
ΔV	Potential difference
δV	Scattering potential of the ion
θ	Scattering angle
$\Theta(E-E_F)$	Heaviside step function
θ_B	Bragg's angle
λ	Radiation wavelength

λ_{IMFP}	Inelastic mean free path
λ_e	de Broglie wavelength
μ	Absorption coefficient
σ_j	Debye-Waller factor
σ_{nl}	Photoionization cross-section at the atomic level nl
τ	Crystallite size
γ	Angle between the polarization of the incident beam and the photoemission direction
ϕ	Take-off angle
φ_{an}	Analyzer's work function
$\chi(k)$	EXAFS oscillations
Ω	Detector's solid angle

1. INTRODUCTION

Carbon monoxide is a toxic gas formed by the incomplete combustion of organic matter. When inhaled, CO binds to the hemoglobin forming carboxyhemoglobin, which decreases the O_2 blood transport capability. The exposition to CO may cause many symptoms depending on the CO concentration in blood, such as dizziness, headache and, in higher concentrations, death. Besides the health issues, CO may cause the poisoning of catalysts used, for example, in full cells, decreasing the reactivity of the catalyst for the desired reaction. In this way, the use of catalysts that improve the CO oxidation reaction, avoiding the emission of this gas, is highly important in vehicles and industrial exhaust fans. However, the catalysts currently used contain noble metals such as Pt, Pd and Rh, making them expensive. Thus, cheaper catalysts with high efficiency may attract attention from the industry.

Cerium oxide (CeO_{2-x}) is a widely studied material for reduction and oxidation reactions due to its facility to absorb and donate O from the atmosphere. CeO_{2-x} nanoparticles are currently used for the CO oxidation reaction in the car exhaust fans, for example. The efficiency of exchanging O depends on the morphological properties of the CeO_{2-x} nanoparticles, such as size and roughness. The main goal of this work is to study the influence of the electronic and structural properties of CeO_{2-x} in the reactivity of Cu-CeO_{2-x} nanoparticles towards the CO oxidation reaction and to elucidate the atomic mechanisms involved in the reaction.

The chapter 2 of this thesis is a literature review about the health, environmental and catalytic issues related to the CO emission, followed by an explanation about the atomic mechanisms occurring in the CO oxidation reaction. In chapter 3, the physical principles, instrumentation and information obtained by the analysis techniques used in this study are described. The chapter 4 presents the experimental procedures and the data analysis used in this study. In chapter 5, all results and the corresponding discussion are presented. Finally, the chapter 6 shows the conclusions and perspectives of this study.

2. LITERATURE REVIEW

This chapter discusses the consequences of the CO emission in the atmosphere, followed by a revision about the catalysts currently used in the CO oxidation reaction.

2.1 Carbon monoxide (CO)

Carbon monoxide (CO) is a colorless, odorless, tasteless, and non-irritating gas formed by the incomplete combustion of fossil fuels and vegetation, as wood, gasoline, coal, natural gas and kerosene. CO is a highly toxic gas that binds with hemoglobin forming carboxyhemoglobin. This bonding is 200-250 times stronger than the hemoglobin bond to O_2 and around 80% - 90% of the inhaled CO binds to the hemoglobin, affecting the blood O_2 transport in a short-term. Thereby, it causes O_2 deficiency to cells even at low exposition of CO (~ 5% of carboxyhemoglobin) [1]. Common symptoms of direct CO poisoning include headache, dizziness, fatigue, nausea, vomiting and chest pain [2]. The formation of carboxyhemoglobin is a reversible process, but due to the strong bound of CO with hemoglobin, the half-life of the CO in the body varies from 2 h to 6 h [1]. Long-term exposition to CO may cause chronic toxicity, that is more evident in organs that demand high O_2 supply, such as brain and heart, and may cause heart and respiratory diseases [1, 3]. For example, CO causes injuries of arterial walls leading to atherosclerosis (condition that causes the hardening and tightening of the arteries). The work on tunnels, where the mean CO concentration due to vehicles' traffic is around 50 ppm, made the workers to present a 35% excess risk of death from arteriosclerotic heart diseases when compared to the rest of the population [3].

Table 2.1 presents the maximal indoor CO exposure recommended by the World Health Organization (WHO). This guideline was formulated aiming to avoid healthy problems related to the CO exposure.

Table 2.1: WHO guidelines for CO exposure, adapted from [4].

Averaging time (h)	Concentration (mg/m^3)	Typical Situation	Comments
0.25	100	Unvented stove	Excursions to this level should not occur more than once per day
1	35	Faulty appliances, as fueled heaters	Excursions to this level should not occur more than once per day
8	10	Occupational exposures	Arithmetic mean concentration
24	7	Averaging of the day	Arithmetic mean concentration

Besides its toxicity, the CO molecule at the atmosphere reacts mainly with •OH [5, 6, 7], indirectly increasing the CH_4 concentration at the troposphere which is typically eliminated by the reaction with •OH. The CH_4 contributes more to the global warming than CO_2 since 1 ton of CH_4 warms Earth between 28-36 times more than 1 ton of CO_2 in a period of 100 years [8] . The reaction of CO with •OH is relatively fast, thereby it concentrates mainly near the urban areas where its emission is higher [5]. Also, its half-life changes with the location and season where it is emitted, varying from 10 days in the summer in the continent to 1 year near the poles due to the temperature and •OH concentration in the atmosphere [7].

Considering these issues, many countries regulated the maximum CO emission [9, 10] and concentration [11, 12] in the atmosphere. For example, the European Union has determined that the maximum emission of CO by incinerators is 100 mg/m^3 under normal temperature and pressure (NTP) conditions per hour [10] and the average for 8 h should not exceed a concentration of 10 mg/m^3 [12]. In Brazil, the maximum CO emission by motor vehicles is 2.0 g/km, meaning that cars can emit a maximum of 2 g of CO for each kilometer traveled since 1997 [9] and the maximum concentration in the air should not exceed 9 mg/m^3 [11].

The most common source of CO is the motor vehicles with gasoline engines [1]. The *Companhia Ambiental do Estado de São Paulo* (Cetesb) reported that, in São Paulo's state, the CO emitted by motor vehicles decreased from 658 tons/year in 2006 to 328 tons/year in 2017, although the number of vehicles used in 2017 increased by 5

million when compared to 2006. Also, it was observed that the CO molecule was mainly emitted by motor vehicles that used gasoline and ethanol as fuels source. This decrease is attributed to the decrease in the new cars emissions. The cars manufactured in 1983 emitted around 33 g/km of CO, while the new cars emit around 0.2 g/km [13]. This decrease in the CO emission is related to the use of catalyst in the car exhaust and an increase in the car engine efficiency [2].

In addition to the health and environmental issues presented, the CO molecule is detrimental to fuel cells, where it poisons the expensive noble-metal based catalysts typically used for this purpose. Therefore, the use of a catalyst in the CO oxidation reaction is essential to avoid poisoning of fuels cells and health and environmental issues. The CO oxidation reaction is driven by catalysts according to:

$$CO + \frac{1}{2}O_2 \rightarrow CO_2 \qquad (2.1)$$

Catalysts that increase the CO oxidation reaction are very important for industrial process and for the control of the vehicle exhaust, as well as indoor air purifiers [14].

2.2 Catalysts

Catalysts are substances that increase the rate of a chemical reaction. It occurs because the catalysts offer an alternative reactional path of smaller activation energy. Figure 2.1 presents an example of the energy diagram for the CO oxidation reaction with and without a Pt catalyst. It can be observed that the activation energy required for the reaction occurrence with catalyst is much smaller than without catalyst. Therefore, during the same period of time, more molecules will react in the system with the catalyst. It means that the use of catalysts makes the reaction faster, increasing the rate of product formation. Despite changing the reaction rate, the catalysts do not change the equilibrium state, that is, catalysts do not change the maximum concentration of products that will be formed and do not prevent the reverse reaction to occur. Catalysts are not consumed during the reaction. Therefore, the catalytic active sites can interact

with more than one reagent molecule. Hence, a small amount of catalyst compared to the amount of reagents is enough for applications [15].

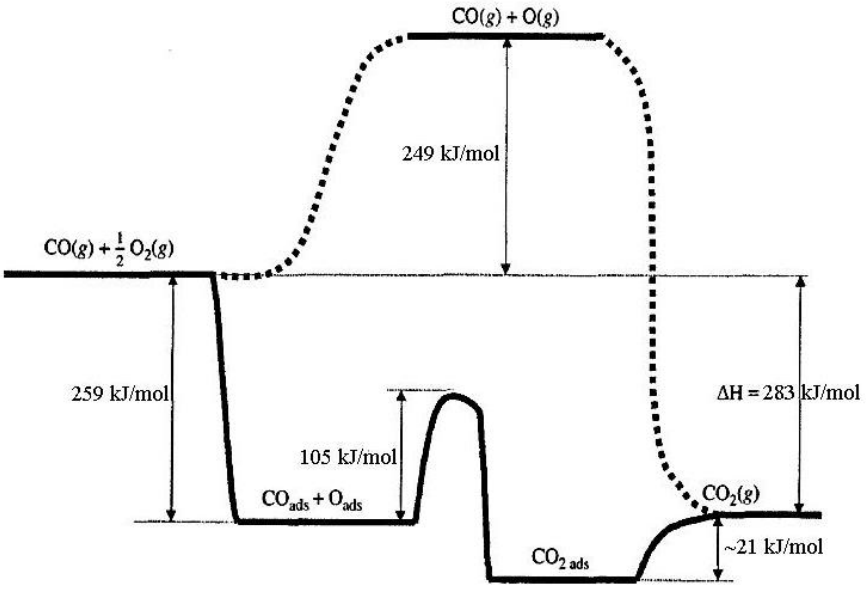

Figure 2.1: Schematic representation of the energy diagram indicating the activation energy for the CO oxidation reaction. The dotted region represents the reaction without catalyst and the solid line represents the reaction with a Pt catalyst. Adapted from [16].

Catalysts can be used in any physical state (solid, liquid or gas). Liquid and gaseous catalysts are usually employed in homogeneous catalysis, where reagents and catalysts are in the same physical state. In heterogeneous catalysis, where the catalyst and reagents are in different physical states, it is typically used a solid catalyst. Some advantages of heterogeneous catalysis are the easy separation and removal of the catalyst from the reactional medium and the possibility of using high temperatures and pressures of the reagents, which increases the reaction efficiency. Since solid catalysts are easily removed from the reactor, they can be used several times.

In solid catalysts, the reaction mechanism is strongly related to the available adsorption sites at the surface. Therefore, it is essential to study the structural, electronic and surface properties of the catalysts. The reaction in a solid catalyst can occur by two distinct mechanisms. In one case, both reagents are adsorbed onto the catalyst surface and react with the product being desorbed as a gas molecule. Other possibility is that only one reagent is adsorbed on the catalyst surface where it reacts with the other reagent present in the atmosphere.

The efficiency of heterogeneous catalysts is directly related to the presence of catalytically active sites, such as O vacancies and steps, which are specific to a given catalytic reaction [15]. Figure 2.2 shows different atomic sites existing in a catalyst in a (a) schematic representation and (b) High Resolution Transmission Electron Microscopy (HRTEM) image. Since the catalytic reaction occurs at the catalyst surface, a high surface area is desired as it usually implies in a greater number of catalytic active sites. The surface area can be increased by decreasing the particles size, since it is inversely proportional to the percentage of atoms at the particle surface, which means that the smaller the particle size, the greater the surface area to volume ratio. Other way to increase the surface area is through the presence of pores at the particle surface. Thus the use of catalysts containing nanoparticles (diameter typically between 1 and 100 nm), can improve the catalytic performance when compared to bulk catalysts. However, it is important to note that, for each catalytic reaction, there is an optimal nanoparticle size meaning that decreasing the nanoparticle size will not necessarily improve the catalytic activity.

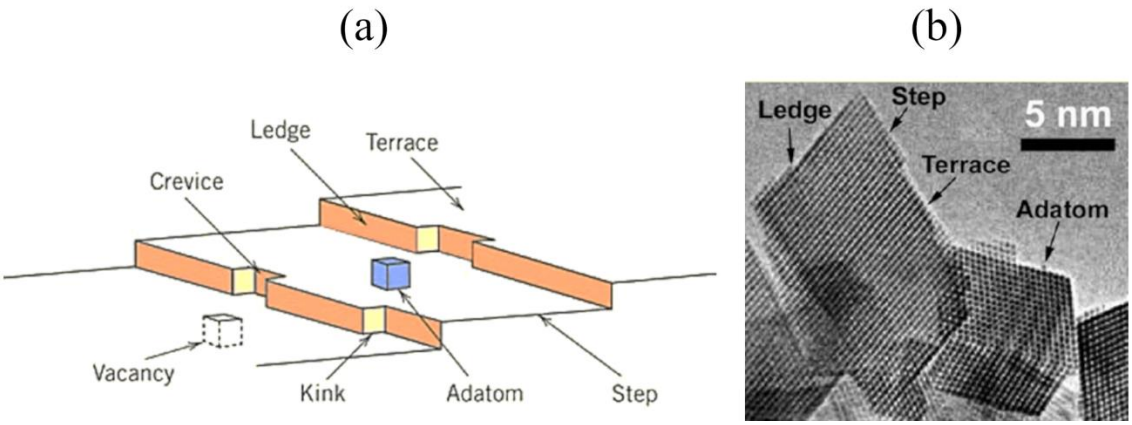

Figure 2.2: (a) Schematic representation of the possible active sites of a catalyst where the atoms are represented by cubes. (b) HRTEM image from $Ce_{0.5}Zr_{0.5}O_2$ crystals, presenting defect regions and possible active sites [17].

In heterogeneous catalysis, it is typically used nanoparticles supported on porous metal oxides, as they decrease or prevent the agglomeration of nanoparticles when exposed to high temperatures. The support may be inert or actively participate in the catalytic reaction. The systems with active supports usually present an increase in catalyst efficiency. The catalyst composed of metal nanoparticles supported on metal oxide is applied in several catalytic reactions, including the CO oxidation reaction.

2.3 Catalysts used in the CO oxidation reaction

The catalysts applied to the CO oxidation reaction are used in motor vehicles exhaust fans and in the exhaust fans from industries due to the implementation of laws that regulated the CO emissions. The efficiency of these catalysts is continuously being improved as the regulation of the maximum allowed CO emissions becomes more restrictive. The catalysts currently used in car exhaust fan need a high thermal stability, once the exhaust fans can achieve temperatures higher than 1000 ºC, and should present a high catalytic activity. Currently, it must convert more than 90% of the NO_x, hydrocarbons and CO into harmless gases [18, 19]. The most commonly used catalyst in the car exhaust fan is the Three Way Catalyst (TWC), where the catalyst is used for the oxidation reactions of CO and C_yH_n and the reduction reaction of NO_x, as presented in (2.2) to (2.7) [20]:

Oxidation reactions:

$$C_yH_n + \left(1 + \frac{n}{4}\right) O_2 \rightarrow yCO_2 + \frac{n}{2} H_2O \quad (2.2)$$

$$CO + \frac{1}{2} O_2 \rightarrow CO_2 \quad (2.3)$$

$$CO + H_2O \rightarrow CO_2 + H_2 \quad (2.4)$$

Reduction reactions:

$$NO + CO \rightarrow \frac{1}{2} N_2 + CO_2 \quad (2.5)$$

$$NO + H_2 \rightarrow \frac{1}{2} N_2 + H_2O \quad (2.6)$$

$$\left(2 + \frac{n}{2}\right) NO + C_yH_n \rightarrow \left(1 + \frac{n}{4}\right) N_2 + yCO_2 + \frac{n}{2} H_2O \quad (2.7)$$

It is important to notice that only the desirable reactions are represented above, but many other reactions can occur. Thus, a high selectivity of the catalyst to the presented reactions is also an important property of the catalyst [18].

The catalysts currently used contain noble metals, such as Rh, Pd and Pt [18]. In these catalysts the reaction occurs in the active sites of the noble metals. The Rh is used

to promote the NO reduction, while the Pt and Pd nanoparticles are used to promote the oxidation of the hydrocarbons and CO. Figure 2.3 presents a schematic representation of the Three Way Catalyst. This catalyst is basically a stainless steel container which incorporates a honeycomb monolith made of ceramic or metal. This monolith has many parallel channels with a high surface area covered by aluminum oxide, where the noble metals particles are supported. The Three Way Catalyst can be divided in three stages. In the first stage occurs the reduction of the NO, at the Rh surface. The second stage is responsible for the C_yH_n and CO oxidation reactions occurrence at the Pt and Pd nanoparticle's surface. The third stage controls the fuel to air flux, controlling the catalyst inlet flux of the car exhaust and external air, related to the O concentration in the monolith. Also, in this stage the outlet flux is controlled in order to improve the catalytic conversion of harmful gases from the car exhaust fan.

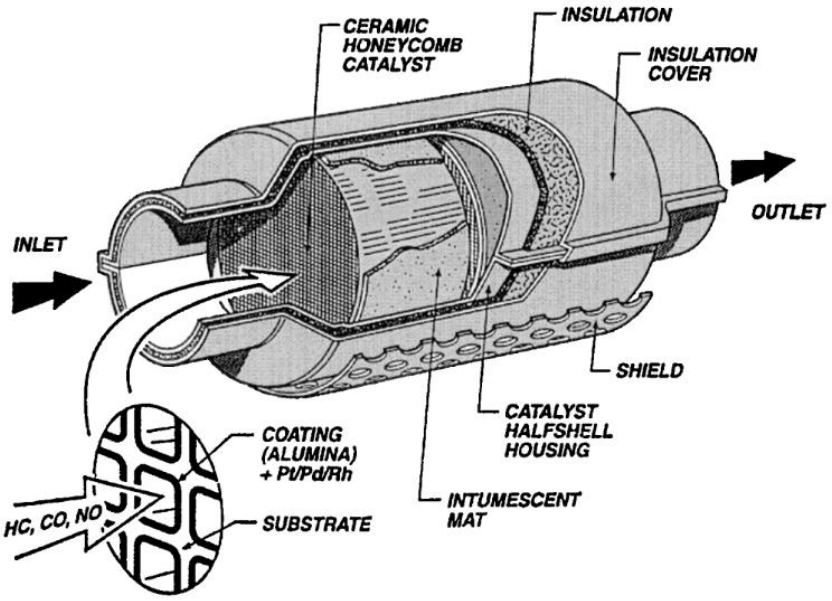

Figure 2.3: Schematic representation of a Three Way Catalyst used in car exhaust, adapted from [21].

The oxidation reaction in noble metals nanoparticles, such as Pt, Pd, Au and Rh, occurs by the adsorption of CO molecules in the catalytic active sites of these nanoparticles. Figure 2.4 shows the CO oxidation mechanism over metals from the Pt group, which occurs in four steps. In the first step, the CO and O_2 molecules present in the atmosphere are adsorbed in the metal surface. After, the O_2 molecule dissociates and reacts with the adsorbed CO molecule. Finally, the product, i.e. the CO_2 molecule, is desorbed from the surface [22].

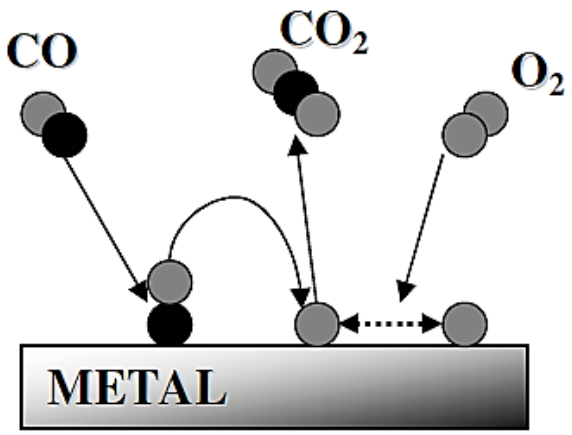

Figure 2.4: Schematic representation of the CO oxidation mechanism over metals from the platinum group [22].

All reactions presented above (Equation (2.2)-(2.7)), require energy (from heat) to occur at the noble metal's surface. In the Three Way Catalyst, the temperature is increased due to the high temperature of the inlet gases since the exhaust gases are formed by the fuel burning. However, when the automobile first starts the engine and the catalysts are cold, the catalytic reaction of converting the harmful gases from the automobile exhaust into harmless gases occurs in a very low rate [20]. In order to increase the efficiency of the Three Way Catalysts at low temperatures, a higher loading of noble metals could be employed. However, a higher noble metals concentration favors the sintering at high temperatures, which would lead to the deactivation of the catalyst. Moreover, it increases a lot the cost of the catalyst since noble metals are very expensive [18]. Therefore, alternative approaches to increase the efficiency, especially for the CO oxidation reaction, at low temperatures (near room temperature) are being developed. For example, when Au nanoparticles supported on CeO_2 or TiO_2 are used in the Three Way Catalyst, they enable the CO oxidation reaction occurrence with good catalytic activity for temperatures around 100 ºC [23]. However the Au nanoparticles are easily deactivated under conditions where the Three Way Catalyst works [18].

Besides low reactivity at low temperatures, noble metals are easily poisoned by the CO molecules that contribute to the deactivation after a certain time [18, 20]. In addition to CO poisoning, two other factors decrease the efficiency of these catalysts. The first one is the adsorption of water on the nanoparticle's surface and the second one is the oxidation of these metals [24], which occurs due to exposure to the gaseous atmosphere at very high temperatures during the catalytic process. An alternative

approach to overcome these issues is the use of new support and nanoparticles. The use of cheaper metals with increased catalyst efficiency at low temperatures would play a part in arousing greater interest in industry.

Considering Equations ((2.2) – (2.7)), the basic reaction for the CO and C_yH_n molecules is the oxidation, while for the NO_x molecule it is the reduction reaction. Therefore, a material with a high oxygen storage capacity (OSC), which is the maximum amount of O that the material is able to provide/accept to/by the gas stream [25], should increase the catalytic activity of the system. It is because the high OSC materials may easily donate or absorb O from the gas exhaust fan and the external air in a reversible way. Cerium oxide (CeO_{2-x} ($0 < x < 0.5$) or ceria when $x = 0$) was found to be the best promoter to be used in Three Way Catalyst since it has a high OSC [26].

Nowadays, in order to achieve a high thermal stability, the main support used for Three Way Catalyst is a CeO_2-ZrO_2 mixed oxide. The use of this material promotes, besides the thermal stability of the Al_2O_3, a better noble metal dispersion, which is responsible for favoring the catalytic reaction at the interface between metal and support, and the storage or release of O in rich or poor O_2 atmospheres, respectively. There are also alternative routes which may enhance the thermal stability of the CeO_2-based catalysts, such as the design of microstructure/textural properties during the synthesis, doping and dispersing the CeO_2 on a carrier, such as Al_2O_3 [18].

Summarizing, the current most common components used for the CO oxidation reaction are [18]:

- noble metals, such as Rh, Pt and Pd, used as the active site for the reaction;
- CeO_2-ZrO_2 mixed oxides, used due to the high OSC and good thermal stability;
- Alumina, used as support because of the high surface area.

2.4 CO oxidation reaction on CeO_{2-x} nanoparticles

Cerium oxide is a pale yellow/white powder, that has been widely used in recent

years in different scientific areas such as fuel cells [27], optics [28] and catalysis [29], being highly important in the construction of the Three Way Catalyst [25]. The main feature that makes it so attractive is its facility in donating or absorbing O from the atmosphere. Cerium oxide can change the oxidation state continuously between Ce(IV) and Ce(III), which corresponds to the fully oxidized (CeO_2) and fully reduced (Ce_2O_3) components, respectively. Also, a non-stoichiometric oxide CeO_{2-x} ($0 \leq x \leq 0.5$) may occur by the creation of O vacancies in the crystal structure of CeO_2. Therefore, the main role of CeO_{2-x} in catalysts (such as the Three Way Catalyst) is to be an O supply, where reduced ceria (CeO_{2-x}) can store O by promoting the reduction of the NO_x, while the CeO_2 can provide O for the CO and C_yH_n oxidation reactions. However, the catalytic activity of CeO_{2-x}-based catalysts is much better than that observed for similar systems composed of other metal oxides with comparable OSC because CeO_{2-x} can also participate in the reaction mechanism besides being an O supply [25]. Also, it is observed that metallic nanoparticles supported on CeO_2 nanoparticles show increased catalytic activity in comparison to the case in which metallic nanoparticles are supported on CeO_2 bulk [30]. It is also known that the size, shape and roughness of CeO_2 nanoparticles affect the catalytic activity [31]. Thus, the control of these properties is pivotal to maximize the catalytic activity [29].

It is well known from the literature that the CO oxidation reaction using CeO_{2-x} occurs by the adsorption of the CO molecule on the lattice O ions [32]. After, the CO molecule reacts with the O atoms, leaving a charged O vacancy ($\square^{2-}$) in the CeO_{2-x} when desorbed. This CO oxidation reaction on CeO_{2-x} is described by

$$CO + * \rightarrow CO_{ads} \tag{2.8}$$

$$CO_{ads} + O^{2-} \rightarrow \square^{2-} + CO_2 \tag{2.9}$$

where * represents the O ions and $\square^{2-}$ a charged O vacancy. The CeO_{2-x} can be re-oxidized when exposed to an O_2 rich atmosphere, following the equation

$$O_{2(g)} + 2\square^{2-} \rightarrow 2O^{2-} \tag{2.10}$$

where $O_{2(g)}$ represents the oxidant atmosphere [32]. Consequently, a higher O vacancy population at the surface of the CeO_{2-x} during the reduction treatment leads to a higher

lattice O ions population after exposure to an oxidizing atmosphere. This is related to a higher probability of the CO oxidation reaction occurrence on the CeO_{2-x} surface. Sayle et al. [33] used non-equilibrium molecular dynamics to study how the size, morphology and Ce(III) fraction of the CeO_{2-x} nanoparticles influence on the reactivity towards CO oxidation reaction. The authors observed that the energy needed to extract an O atom of the CeO_{2-x} lattice increases with the increase in the Ce(III) fraction, decreasing the reactivity of the nanoparticles for the CO oxidation reaction. Also, the energy needed to extract an O atom is minimal for a Ce(III) fraction of 8% for the range of nanoparticle's morphology and sizes studied and maximal for a Ce(III) fraction of 40 %, except for small nanoparticles (3.5 nm). For Ce(III) fractions higher than 40 %, the energy needed to further extract an O atom starts to decrease with the reduction of the nanoparticles. Thus, controlling the surface O vacancy population of CeO_{2-x} is essential to control the catalytic activity in the CO oxidation reaction.

In a previous work of the research group, Della Mea et al. [34] synthesized CeO_{2-x} nanoparticles by the precipitation method. Several parameters were varied like the solvent type, concentration, and temperature of synthesis. The as-prepared samples were characterized by Transmission Electron Microscopy (TEM), X-Ray Diffraction (XRD), Brunauer-Emmett-Teller (BET) and Scanning Electron Microscopy (SEM) techniques. After, the synthesized nanoparticles were exposed to a CO reducing atmosphere during heating to 500 °C. During the reduction process, the samples were analyzed *in situ* by NAP-XPS (Near Ambient Pressure X-Ray Photoelectron Spectroscopy) and time-resolved XANES (X-ray Absorption Near Edge Structure) at the Ce L_3 edge. It was observed that the change in the synthesis parameters allowed controlling many properties of the CeO_{2-x} nanoparticles, such as the mean diameter, surface area, pore volume, reduction temperature and surface O vacancy population. Moreover, the synthesized nanoparticles are highly reducible reaching high Ce(III) fraction values at very small temperatures when compared to the literature and to a commercial CeO_{2-x} standard. The standard sample did not reduce during the heating process to 500 °C. The Ce(III) fraction at the end of the reduction process and the reduction temperature of the synthesized nanoparticles can reach 0.92 and 108 °C, respectively. Structural and electronic parameters such as diameter, specific surface area, pore volume, initial O vacancy population (before reaction with CO) and hydrophobicity play a fundamental role in the reduction kinetics of CeO_{2-x} by CO.

2.5 CO oxidation reaction on metallic nanoparticles supported on CeO_{2-x}

Cargnello et al. [35] studied the influence of the nature of the interface between metal and CeO_2 on the reactivity of the catalyst towards the CO oxidation reaction. The authors characterized the samples by using TEM and CO chemisorption measurements in nanoparticles containing Ni, Pt and Pd of different sizes and supported on CeO_2. The authors observed that the reactivity increases with the decrease of the nanoparticles size. These results allowed the authors to conclude that in catalysts containing Ni, Pt or Pd nanoparticles supported on CeO_2, the CO oxidation reaction occurs at the interface between the metallic nanoparticles and the CeO_2 support. The CO molecule is adsorbed at the surface of the metallic nanoparticle, while the O atom is provided by the CeO_2 support. After occurrence of the CO oxidation reaction, the CeO_2 is re-oxidized following Equation (2.10). Therefore, catalysts composed of active supports, such as CeO_2, present a higher catalytic activity than inactive supports such as Al_2O_3.

A similar mechanism was observed by Jia et al. [36] for catalysts composed of CuO nanoparticles. The authors used XRD, HRTEM and N_2O chemisorption techniques to characterize the CuO/CeO_2 catalyst and the CeO_2/CuO inverse catalyst. The authors observed that both systems presented the same catalytic activity in the CO oxidation reaction, indicating that the reaction occurs at the interface of the CuO and CeO_2 oxides. The literature shows that pure CuO and pure CeO_2 are both active for the CO oxidation reaction. However, a higher catalytic activity is observed when CuO and CeO_2 are combined [37].

It is interesting to note that the CO oxidation reaction of the specific case of Cu/CeO_{2-x} catalysts is not yet fully understood. In the literature, there are two main atomic mechanisms proposed for this reaction. Some authors [38, 39, 40, 41] affirm that the CO oxidation reaction occurs by the adsorption of the CO molecule on the Cu(II) species, while the O atom is adsorbed in the O vacancies of the CeO_{2-x} support. In this mechanism, which will be designate as *Mechanism I,* the O atom for the CO transformation into CO_2 is given by the Cu(II) species. The CO oxidation reaction is described in the following Equations ((2.11) - (2.12)):

$$CO + Cu(II) \leftrightarrow CO - Cu(II) \quad (2.11)$$

$$CO - Cu(II) \rightarrow Cu(I) + CO_2 \quad (2.12)$$

After the CO_2 desorption, the Cu(I) specie is re-oxidized following equation:

$$Cu(I) + Ce\ (IV) \leftrightarrow Cu(II) + Ce(III) \quad (2.13)$$

where the O involved in the reaction are the O ions adsorbed at the O vacancies of the CeO_{2-x} support. Thus, the CO oxidation reaction occurs at the interface between Cu and CeO_{2-x}. After, the O vacancies of CeO_{2-x} are filled by the O present in the atmosphere following Equation (2.10).

On the other hand, some authors [36, 37, 42, 43] propose the CO oxidation reaction by Cu/CeO_{2-x} nanoparticles as schematically represented in Figure 2.5. This mechanism, which will be identified as *Mechanism II*, is known as *Mars-van Krevelen* mechanism. The CO oxidation reaction occurs by the chemisorption of the CO molecule on the Cu(I) species, which are the active sites for the CO oxidation reaction. The O_2 molecule is adsorbed in the O vacancies of the CeO_{2-x} support, forming active O_2^- or lattice O^{2-} species. Thus, the reaction occurs at the interface between the Cu and CeO_{2-x} with the chemisorbed CO molecule migrating to the interface and reacting with the O ion from an active site of the CeO_{2-x}. After reaction, the active sites of the Cu nanoparticles are regenerated and the O vacancies of the CeO_{2-x} support are filled by the O_2 present in the atmosphere, leaving the catalyst active for the next reaction cycle.

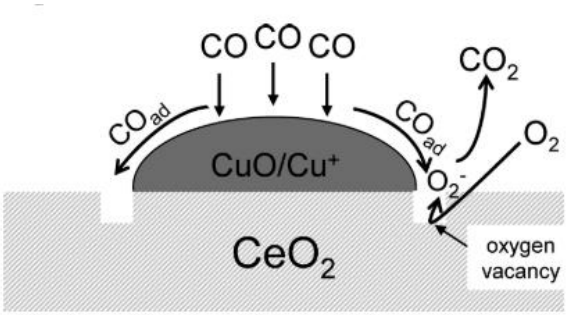

Figure 2.5 Schematic representation of the *Mars-van Krevelen* mechanism for the CO oxidation reaction on systems composed by Cu-CeO_2 nanoparticles [36].

Lykaki et al. [42] analyzed the influence of the CeO_2 shape (nanorods, nanocubes and nanopolyhedra) on the catalytic activity for the CO oxidation reaction

for Cu/CeO_2 catalysts. The samples were characterized by XRD, XRF (X-Ray Fluorescence), H_2 Temperature Programmed Reduction (H_2 – TPR), TEM, XPS and *in situ* Raman Spectroscopy. It was observed that the reactivity towards CO oxidation is mainly influenced by the increase of defects in the crystalline lattice, Cu(I) concentration, and concentration of O atoms adsorbed in the CeO_2 vacancies instead of the nanoparticle size. Thus, the efficiency of the Cu/CeO_2 catalyst is directly associated to the electronic and structural properties of the CeO_2 support [44]. These properties influence on the metal-support interaction, which may be related to easier exchange interplay between the reduced and oxidized state, improving the catalytic activity [45, 46].

Zhang et al. [47] analyzed the effect of the preparation method in the reactivity of CuO/CeO_2 nanoparticles for the CO oxidation reaction. CuO/CeO_2 nanoparticles were synthesized with different methods and characterized using XRD, BET, TEM, H_2-TPR (measured from room temperature to 850 °C) and XPS. It was observed that the increase of the catalytic activity can be attributed to the Cu species that can reduce at lower temperatures, higher concentration of Cu(I) species, and higher O surface population.

Lu et al. [48] studied the influence of the CeO_2 support (synthesized using different methods as well as commercial sample) on the catalytic activity of Cu/CeO_2 nanoparticles for the CO oxidation reaction using SEM, BET and XRD techniques. The authors observed that a higher catalytic activity is related to a better dispersion of the Cu nanoparticles. Then the systems that presented smaller and well dispersed Cu nanoparticles showed a higher catalytic activity for the CO oxidation reaction. A similar behavior was observed by Martinez-Arias et al. [49] that examined CuO/CeO_2 and $CuO/ZrCeO_4$ nanoparticles using TEM, XRD, DRIFTS (Diffuse Reflectance Infrared Fourier Transform Spectroscopy), CO-TPD (CO Temperature Programmed Desorption) and EPR (Electron Paramagnetic Resonance) techniques. The authors observed that both metal nanoparticles and oxide support reduce and oxidize when exposed to CO and O_2 atmospheres, respectively. Also, the limiting step for the catalytic activity is the re-oxidation of the catalysts. The authors observed that the CuO/CeO_2 nanoparticles presented the highest activity for the CO oxidation reaction. It was attributed to the presence of well dispersed small CuO clusters, which have active sites for the CO chemisorption. Additionally, the redox properties of the Cu nanoparticles are enhanced

by the interaction with the CeO_2 support.

Harrison et al. [41] prepared CeO_2 and CuO/CeO_2 nanoparticles following the impregnation or co-precipitation methods, which were exposed to different calcination temperatures, between 100 °C and 1000 °C. These samples were analyzed by BET, XRF, XRD, EXAFS (Extended X-Ray Absorption Fine Structure) and EPR techniques. The authors observed that the reactivity towards CO oxidation is mainly influenced by the calcination temperature instead of the preparation method. In the catalyst calcined at 1000 °C, the CuO phase sinterizes, then decreasing the reactivity of the samples irreversibly. Also, they noticed that the samples calcined at the same temperature presented the same Cu species. The authors observed that amorphous and larger Cu(II) aggregates are reduced easier than Cu(II) dimers, being more reactive for the CO oxidation reaction. Thus, it was concluded that the Cu(II) concentration and the easy exchange between the reduced and oxidized states are directly related to the reactivity of the sample.

In another work, Martinez-Arias et al. [43] studied the reduction properties of CeO_2 nanoparticles in catalysts composed of Cu/CeO_2 and CeO_2 nanoparticles using *in situ* XRD, *in situ* Raman Spectroscopy and O_2 Electron Probe Magnetic Resonance techniques. The reduction and oxidation treatments were performed with CO and O_2 atmosphere, respectively, and at temperature of 500 °C. The authors observed that the support of the Cu/CeO_2 nanoparticles presented improved redox properties if compared to the CeO_2 nanoparticles without Cu nanoparticles. It shows that the interaction between Cu and CeO_2 presents a synergy effect, with electron transfer between the metallic nanoparticle and the support. A similar mechanism was observed in a previous work of the group, where Thill et al. [50] studied the influence of transition metal nanoparticles in the reduction properties of CeO_2 nanoparticles using systems composed of Pd/CeO_2, Au/CeO_2, $Au_{.0.9}Pd_{0.1}/CeO_2$, $Au_{.0.8}Pd_{0.2}/CeO_2$ and commercial CeO_2. The samples were studied using *in situ* XAS during reduction with a H_2 atmosphere at 500 °C and XPS measurements. At the end of the reduction treatment, it was observed that the commercial CeO_2 (without metallic nanoparticles) presented the lowest Ce(III) fraction among the samples studied. The Ce(III) fraction depends on the composition of the metallic nanoparticles. Moreover, the charge transfer from the metallic nanoparticle to the CeO_2 support was measured empirically by *in situ* XANES measurements and confirmed by XPS measurements.

Other effect that may change the catalytic activity of nanoparticles containing Cu/CeO_2 is the Strong Metal Support Interaction (SMSI) effect. It is characterized by the almost complete inhibition of the CO and H_2 chemisorption capacity [51]. The SMSI effect is related to a geometric and/or electronic factor [52]. The geometric factor is characterized by the migration of functional groups from the support to the metallic nanoparticles surface during the activation of the catalyst under a reduction atmosphere. This effect may create new catalytic active sites or block those existing, causing an increase or decrease in catalyst efficiency for the reaction used, depending on the case. In a previous work of the group [53], Cu and Ni nanoparticles, non-supported and supported on CeO_2 nanoparticles, were analyzed by HRTEM, XPS and *in situ* XAS, during heating to 500 °C under a H_2 atmosphere. It was observed a decrease in the reduction temperature of the Ni/CeO_2 nanoparticles when compared to the non-supported Ni nanoparticles. The same effect was not observed for the Cu/CeO_2 nanoparticles. This decrease in the reduction temperature was attributed to the electronic factor of the SMSI effect, responsible in this case for the charge transfer from the support to the Ni nanoparticle. The SMSI effect in the Ni/CeO_2 nanoparticles was confirmed by XPS and HRTEM measurements, where the capping layer of the support over the Ni nanoparticles was observed. The same effect was observed in another work from the group, where Figueiredo et al. [54] studied the geometrical and electronic factor of the SMSI effect for systems containing Cu and Ni nanoparticles, with different concentrations, supported on commercial CeO_2. It was used *in situ* XAS and NAP-XPS techniques to characterize the samples at 500 °C under a H_2 and CO_2 atmosphere. It was observed the SMSI effect for the samples with higher Cu concentrations. Also, the capping layer of the support disappeared when the sample was exposed to an oxidizing atmosphere, which is expected for the SMSI effect. It was noticed that the nanoparticles that presented the SMSI effect also presented a lower reduction temperature for the metallic nanoparticle and an oxidation of the CeO_2 nanoparticles during H_2 reduction treatment, showing the electron transfer from the support to the metallic nanoparticle. The NAP-XPS analysis allowed to conclude that the SMSI effect is related to a charge transfer to specific electronic levels of the CeO_2 support. This capping layer from the SMSI effect has strong influence on the reactivity towards CO_2 dissociation reaction [55].

Martinez-Arias et al. [56] studied the reduction and oxidation mechanism of

CuO/CeO_2 nanoparticles during exposure to a CO and O_2 atmosphere, respectively. The sample was characterized using XRD, Raman, XAS, XPS and EPR techniques. The results allowed establishing a model for the reduction and oxidation processes for this system. In this model, the reduction starts at the interface between Cu and CeO_2. However, the oxidation of the highly reduced states starts in the Ce atoms far away from the Cu nanoparticles and progress in the direction of the metal-support interface. The oxidation of the Cu atoms occurs later and is damped by the stabilization of the Cu(I) state during the redox cycle. Also, it was observed that a high O vacancy population in CeO_{2-x} induces the formation of Cu(I) species following the process given by Equation (2.13) [57]. The Cu(I), Cu(II), Ce(III) and Ce(IV) species may be involved in the CO oxidation reaction mechanism. Thus, the easy interplay between Cu(I) and Cu(II) is related to a superior catalytic activity for the CO oxidation reaction [41, 44].

Despite all the work existing in the literature, the influence of the CeO_{2-x} nanoparticles in the catalytic activity and the atomic mechanism of the CO oxidation reaction on Cu-CeO_{2-x} nanoparticles are not fully understood yet. Thus, the main goal of this work was to study the influence of the electronic and structural properties of CeO_{2-x} in the reactivity of Cu-CeO_{2-x} nanoparticles towards the CO oxidation reaction and to elucidate the atomic mechanisms involved in the reaction. Thereby, optimizing the properties of Cu-CeO_{2-x} nanoparticles for the CO oxidation reaction to allow the production of a highly efficient catalyst that is cheaper than those currently used.

3. ANALYSIS TECHNIQUES

In this chapter, the physical principles of the analysis techniques used to characterize the Cu-CeO_{2-x} nanoparticles, as well the information that can be obtained with each technique, are briefly explained.

3.1 Transmission Electron Microscopy (TEM)

The TEM is a powerful tool for materials science that uses the interaction of electrons with the sample to obtain structural and morphological information about the material. The transmission electron microscope works similarly to the optical microscope, as can be seen in Figure 3.1. However, it uses electrons instead of light as an illuminating source. This allows higher resolution for the analysis of the material since electrons may have a much smaller wavelength than the visible light, depending on the accelerating voltage used [58].

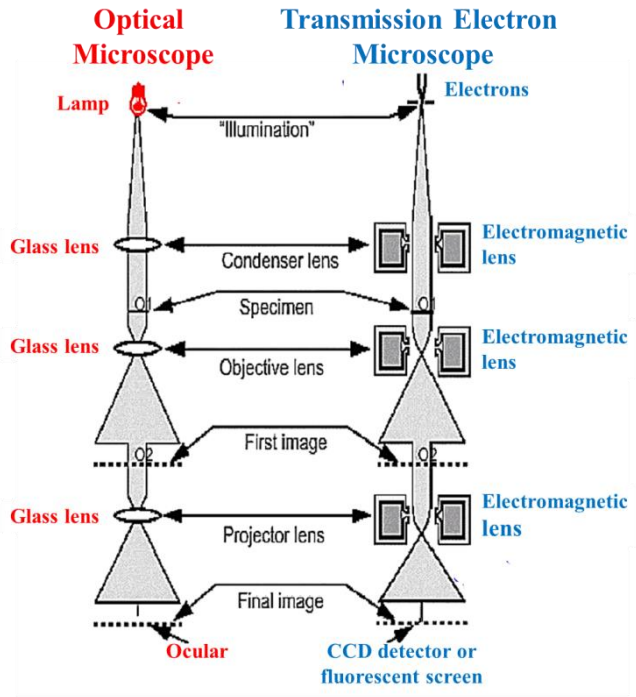

Figure 3.1: Comparison between the schematic representation of the optical microscope (on the left) and electronic microscope (on the right) [59].

The electrons source can operate by two main physical principles: thermionic or field emission effects. Thermionic sources use a W filament or a LaB_6 crystal that emit

electrons when heated. Electron sources that operate by field emission works by a process known as quantic tunneling, in which the electrostatic potential of the cathode (source), typically made of a single crystal of W, is increased to allow the electrons to leave the material's surface. This electron source is typically used for images with higher magnifications since it has an emission area smaller than the thermionic source. Around the electron source is fixed the Wehnelt cylinder, which is an electrode that is used to focus the electron beam. The beam is focused by applying a negative potential in the cylinder in comparison to the source. To minimize the scattering of electrons by the air molecules, the transmission electron microscope column is kept in high vacuum ($\sim 10^{-6} - 10^{-7}$ mbar). After emission, the electron beam is accelerated by an electric potential difference and focalized on a region of the sample by electromagnetic and electrostatic lenses. The final energy of the electron beam depends on the potential difference applied. The electromagnetic lenses are built from coils, where the intensity of the magnetic field depends on the applied current, which makes it possible to change the focus of the lenses. The asymmetry in the generated magnetic field can produce secondary and undesired effects such as aberrations and astigmatism. When the electron beam illuminates the sample, elastic and inelastic collisions occur resulting in scattered and transmitted electrons through the sample. The transmitted electrons are collimated and create the final image when arriving in the detector, that can be a fluorescent screen or a CCD (charge-coupled device) [60].

The contrast observed in the TEM image depends on the operational mode used. The most used mode is the bright field (BF) one, where the contrast is given mostly by the amplitude of the transmitted wave and depends on the electronic density and thickness of the sample. It means that if the sample is electronically dense or thick, few electrons are transmitted, creating a dark region on the image. On the other hand, thin regions or regions with low electronic density give bright spots in the image. This mode is usually used to obtain the size and morphology of nanoparticles because it shows the projection of the structures present in the sample. Figure 3.2 shows an example of a bright field TEM image of Au-Co bimetallic nanoparticles with an inner region (core) made of Au and an outer region (shell) made of Co atoms. The image presents the core region darker than the shell region because the Au atoms are electronically denser than the Co atoms, besides the core region being thicker than the shell region [58].

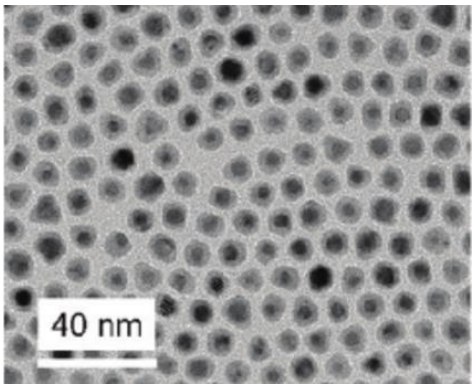

Figure 3.2: Example of a TEM image in the bright field mode of Au-Co nanoparticles, where the core region contains Au atoms while the shell, Co atoms [61].

Another TEM image mode is the dark field, where the contrast is given by the electrons diffraction. This image is obtained by selecting only those electrons that undergo Bragg scattering (which will be explained in Section 3.2). In a crystalline sample, it is possible to select a specific Bragg reflection, related to a specific crystalline plan, by placing an aperture in the transmitted beam, hence only the particles which satisfy the Bragg's law for the selected crystalline plane appear bright [60]. The electron diffraction patter is formed in the focal plane of the objective lens and can be observed by changing the position of the objective's focal plane.

Another contrast used in TEM images is the phase-contrast, which is responsible for the contrast in High Resolution TEM (HRTEM) images. The phase of the electron wave changes with the thickness of the sample and the electron energy, then changing the interference pattern observed. The HRTEM image allows the analysis of the crystal structure of the material because the image formed is the inverse Fourier Transform of the diffraction pattern formed at the focal plane of the objective lens. However, the final image obtained in HRTEM depends not only on the sample that is being measured, but also on the lenses, electron gun and apertures used, i.e., the image is a convolution of the signal from the sample and the system used [62].

When the electron beam interacts with the sample it generates a wide range of secondary signals. These signals can be detected and analyzed using spectroscopic techniques that work together with the electron microscopes, improving the information obtained from the measurements. A generally used technique in TEM is the Energy Dispersive Spectroscopy (EDS), which provides chemical information of the sample. When the high energy electron beam interacts with the TEM sample, some electrons in

the beam are inelastically scattered by the inner shell electrons, causing a transition of the inner shell to an empty upper electronic level or the ejection of these electrons from the atoms leaving them in an excited state with a vacant electronic level. The relaxation of these atoms can occur by the downward transition of an electron from an upper electronic level to the vacant level. In this de-excitation process, energy can be released by the Auger effect [58] or fluorescent emission, which happens with the emission of an Auger electron or an X-ray photon, respectively. The probability of emitting a photon, the characteristic X-ray, is higher for atoms with higher atomic number. When a photon is emitted, its energy is given by the difference in energy between the two electronic levels involved in the transition. The EDS technique detects the energy of the characteristic X-ray emitted by the sample using a detector, usually a semiconductor diode, made of a single crystal of Si or Ge. When entering the detector, the X-ray photon can transfer its energy to the valence electrons of the diode, exciting them to the conduction band, then creating electron-hole pairs. A reverse-bias voltage is applied to the diode in order to detect the charge. The detected charge is proportional to the number of electron-hole pairs generated. The natural line broadening of the characteristic X-rays is only few eV (typically 1-5 eV), but due to the experimental uncertainty the measured line width is higher than 100 eV. For this reason, the EDS technique is more useful when the spectrum is transformed into a quantitative compositional profile or a compositional image (map) than presented as a simple spectrum of intensity as a function of the X-ray photon energy [58, 60] .

3.2 X-Ray Diffraction (XRD)

The XRD technique gives the angular interference profile caused by the scattering of a monochromatic X-ray beam incident on a sample. The angular interference profile, known as diffractogram, is characteristic for each crystalline structure. The analysis of the diffractogram allows identify the phases present in the sample and the concentration and structural properties, like crystallite mean size and lattice parameter, of each phase.

The intensity detected at a given angle from the incident direction corresponds to a superposition of waves scattered by the sample in that direction. Whenever the sample

has long-range crystalline order, the superposition of the scattered waves produces constructive interference in specific directions and this can be seen as a maximum of intensity in the diffractogram. The condition to be fulfilled in order to obtain the diffraction maxima is summarized in a single relation, known as Bragg's law. It associates the wavelength of the incident X-rays with the interplanar spacing of the crystalline phase:

$$2dsen\theta = n\lambda \tag{3.1}$$

where d is the interplanar distance, θ is the angle between the incident or diffracted beam and the sample surface and λ is the wavelength of the incident X-ray beam. Figure 3.3 shows schematically the X-ray diffraction phenomenon for a given family of crystalline planes. The optical path length difference for waves scattered by an atom and its neighbor depends on the distance between them (in the case of crystalline structures this distance is equal to the interplanar distance) and the angle of incidence and scattering of the beam. A maximum of diffraction, also known as Bragg's reflection, occurs when the optical path length difference is equal to an integer number of wavelengths.

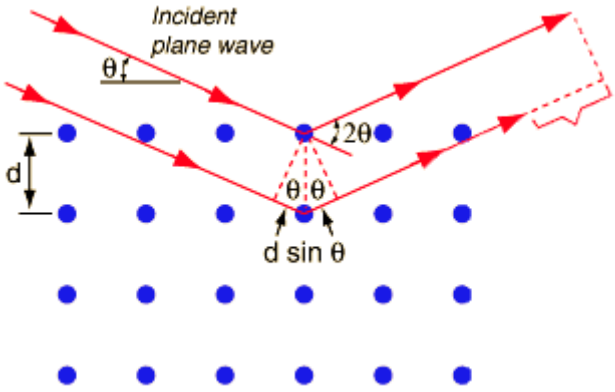

Figure 3.3: Schematic representation of X-ray diffraction phenomenon in a crystalline material [63].

Amorphous materials do not satisfy the conditions described in Bragg's law since the random positioning of the atoms in the material causes partially destructive interference in all directions. Therefore, the diffractogram of amorphous materials does not present Bragg's reflections. Figure 3.4 shows a comparison between the diffractogram from a crystalline and an amorphous material. It is possible to notice that

the diffractogram from the crystalline material presents Bragg's reflections related to the crystalline planes in specific angles, whereas the diffractogram of the amorphous material does not present these Bragg's reflections.

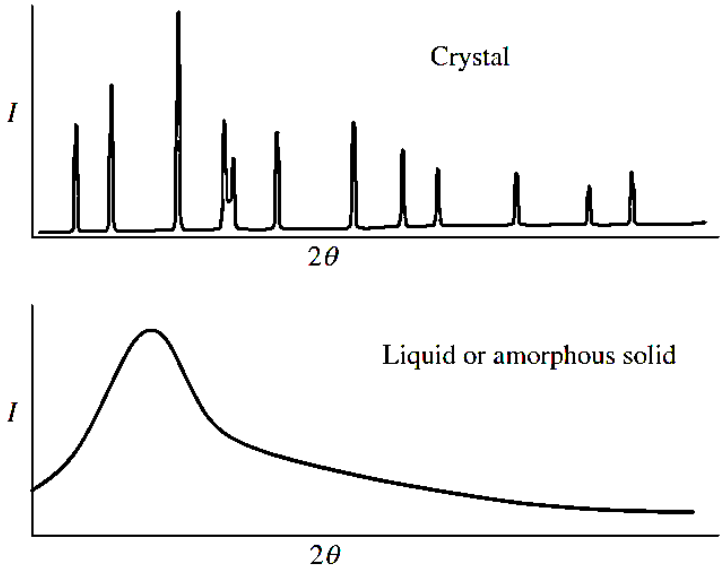

Figure 3.4: Schematic representation of diffractograms from a crystalline and an amorphous material [64].

The diffractograms are typically shown as intensity versus 2θ that represents the sum of the incidence and detection angles in relation to the sample surface. The intensity of each peak is proportional to the square module of the structure factor that can be calculated by:

$$F_{hkl} = \sum_{j=1}^{N} f_j e^{i\vec{K}\cdot\vec{R_j}} \tag{3.2}$$

where j represents the lattice atoms, $\vec{K}$ is the difference between the incident and diffracted wave vectors, $\vec{R}_j$ is the position vector of the jth atom and f_j is the atomic scattering factor, which depends on the electronic density of the jth atom and the scattering angle θ. The atomic scattering factor refers to the interference of the wave scattered by the electrons of the atoms and is defined as the ratio between the amplitude of the X-ray scattered by an atom (composed by Z electrons) and the amplitude of X-ray scattered by a single electron in the same conditions. The intensity (I) of the beam scattered by one electron for an unpolarized incident beam (I_o) in a given point (P) can be calculated using the Equation (3.3):

$$I = I_0 \frac{e^4}{r^2 m_e^2 c^4} \cdot \frac{1 + \cos^2 2\theta}{2} \quad (3.3)$$

where e and m_e are the charge and mass of the electron, respectively, c is the velocity of light and r is the distance from the electron to the point P. It is possible to notice that the intensity of the scattered beam is dependent on the angle 2θ by the factor $\frac{1+\cos^2 2\theta}{2}$, which is the polarization factor. The intensity of the beam scattered by a single atom is basically the superposition of the waves scattered by each of its electrons. The intensity of the beam is maximum at the same direction of the incident beam while in other directions it decreases due to the phase difference between waves scattered by different electrons.

The intensity of a Bragg's reflection is dependent of four other factors: *multiplicity factor, Lorentz factor, absorption factor* and *Debye-Waller factor.* The *multiplicity factor* (p) determines the number of equivalent planes giving a reflection at the same angle (2θ), i.e., the number of planes in a family of crystalline planes. A higher number of equivalent planes in the crystal increases the intensity of the Bragg's reflection since it increases the probability of satisfying the Bragg's law. The *Lorentz factor* (LF) is a geometric factor that takes into account the divergence and the partial monochromatization of the incident beam. It depends on the Bragg's angle and can be calculated by:

$$LF = \frac{1}{4\ sin^2\theta\ cos\theta} \quad (3.4)$$

The *absorption factor* (AF) is related to the absorption of X-ray in the sample, and can be calculated by:

$$\mathrm{AF} = \frac{1}{2\mu}\left(1 - e^{-2\frac{\mu t}{sin\theta}}\right) \quad (3.5)$$

where μ is the absorption coefficient and t is the sample thickness. The *Debye-Waller factor,* also known as temperature factor, is related to the thermal vibrations of the atoms around an equilibrium position. The amplitude of these vibrations increases with the increase of the temperature. The vibration causes a broadening of the Bragg's

reflections and a decrease in their maxima intensity. The decrease in the intensity due to the Debye-Waller factor is more evident for higher angles since it implies in smaller d values. Considering all these factors, the intensity of the diffracted beam can be obtained by:

$$I = |F|^2 \cdot p \cdot \left(\frac{1 + \cos^2 2\theta}{\sin^2 \theta \cos \theta}\right) \cdot \frac{1}{2\mu} \cdot e^{-2M_T} \quad (3.6)$$

where e^{-2M_T} is the temperature factor, which depends on the model used to describe the thermal atomic oscillations.

Since the intensity changes with the structure factor, the diffractogram is dependent on the crystalline structure. Thus, the XRD technique is ideal for identifying the crystalline phases present in the sample.

The Bragg's reflections have a full width at half maximum (FWHM) inversely proportional to the crystallite size. When the crystallite size is smaller than 100 nm, it is possible to estimate its size using the Scherrer's Equation (3.7):

$$\tau = \frac{K\lambda}{\beta cos(\theta_B)} \quad (3.7)$$

where τ is the crystallite size, λ the wavelength of the incident beam, K is the form factor (0.9 for spherical particles), θ_B is the Bragg's angle and β is the full width at half maximum (FWHM) of the Bragg's reflection.

The constructive interference between the scattered waves occurs whenever Equation (3.1) is satisfied. Hence the diffractogram can be acquired by changing either the angle of incidence or the wavelength of the incident X-ray beam. A widely used method for XRD measurements is the Powder Method. In this method, the analyzed sample should be a fine powder to avoid a great roughness at the surface and to ensure the crystals are randomly positioned (each grain is a single crystal), then increasing the possibility that some crystal is oriented in order to satisfy the Bragg's law for a fixed wavelength λ and a given incident angle θ of the X-ray beam. A monochromatic X-ray beam is focused on the sample and the measurement is conducted with the change of the incidence and detection angle θ in a given interval [65]. The measurement is performed

using a diffractometer, as that shown schematically in Figure 3.5. The X-ray diffractometer is constituted by an X-ray source, a high voltage power supply, a cooling system, a sample holder, a monochromator and a detector.

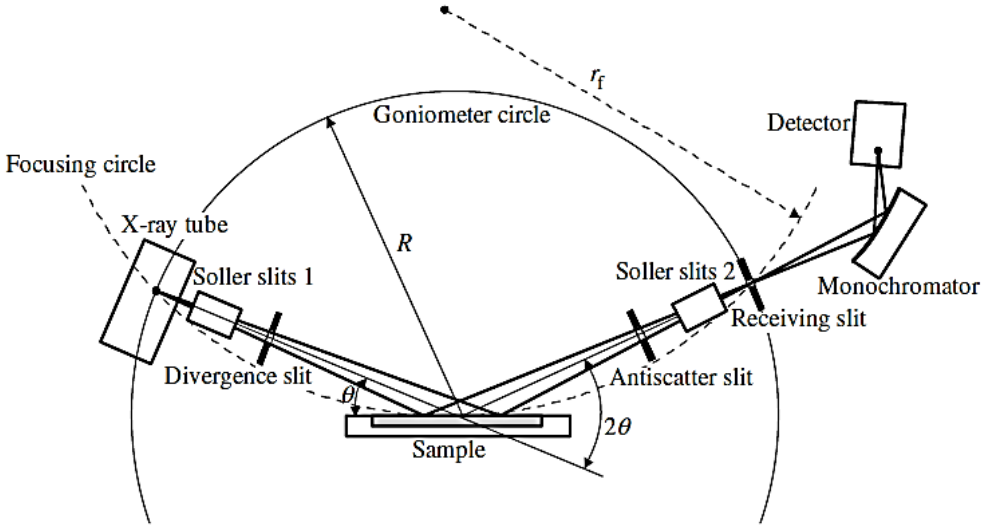

Figure 3.5: Schematic representation of a conventional X-ray diffractometer [64].

The X-ray source is constituted by five main components: a high voltage power supply, an electron source, an electrode, a metallic target and a cooling system for the target, as shown in Figure 3.6. The electron source typically consists of a tungsten filament that emits electrons by thermionic effect. These electrons are accelerated from the cathode (located behind the electron source) to the anode (target of the X-ray tube). The energy acquired by the electrons depends on the potential difference applied. Since the anode is usually grounded, the voltage is applied only at the cathode. The target consists of a metallic plate, usually made of copper. The X-rays are emitted by Bremsstrahlung and characteristic X-ray emissions. However, the X-ray emission has a very low efficiency, typically less than 1%. This happens because the electrons may interact with the material in many other different ways like elastic or inelastic collisions emitting an Auger electron. The energy transfer from the electrons to the target heats the X-ray tube which makes the cooling system essential for the system. Since the target is grounded, water is used to cool it.

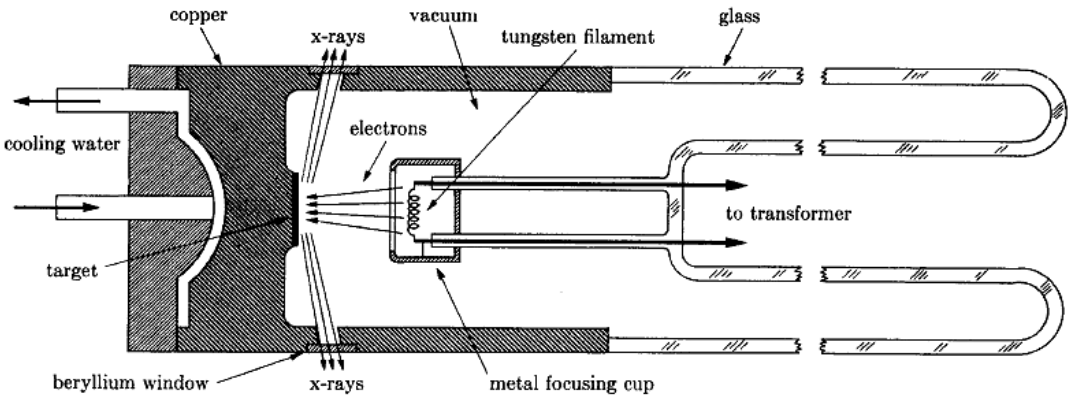

Figure 3.6: Schematic representation of an X-ray source where the electrons are emitted by a tungsten filament and accelerated towards the metallic target, where they collide with the material, emitting X-rays [65].

Figure 3.7 shows the X-ray spectra emitted by an X-ray source with a Mo target as a function of the voltage applied. It is possible to observe that for operational voltages lower than 20 kV it presents only the Bremsstrahlung contribution. For operational voltages higher than 20 kV, the X-ray spectrum corresponds to both contributions, the Bremsstrahlung and the characteristic X-ray emission. The Bremsstrahlung is produced by the deceleration of a charged particle and appears in the Figure 3.7 as a continuous spectrum. The minimum X-ray wavelength obtained by the Bremsstrahlung effect corresponds to the maximal energy of the electron beam. The characteristic X-ray is emitted when an incoming electron transfers energy to an inner-shell atomic electron in the physical process already explained for the EDS technique (see Section 3.1). This only happens when the electron beam has enough energy to transfer to the atom. Therefore, the Mo characteristic X-ray only appears in the spectrum for a voltage higher than 20 kV. Figure 3.7 presents two peaks from the Mo Kα e Kβ emissions. The Kα and Kβ radiation are due to the filling of the K-shell by an L-shell and M-shell electron, respectively.

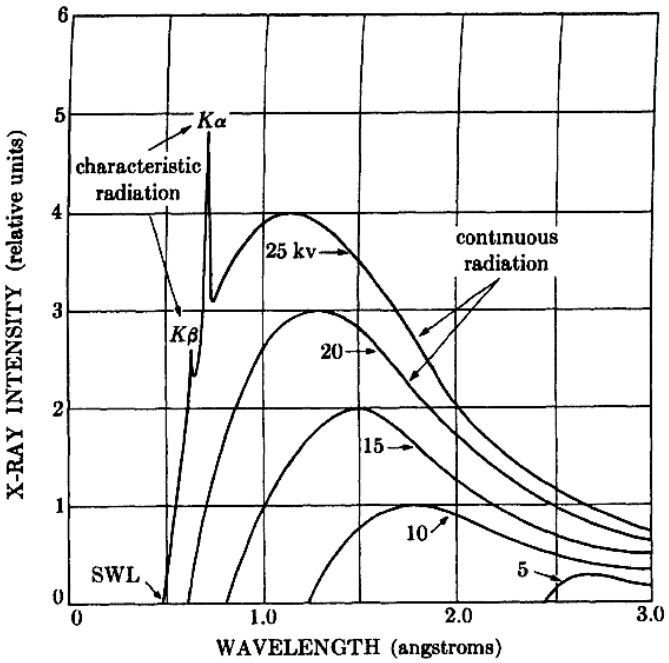

Figure 3.7: X-ray spectra coming from a Mo X-ray source as a function of the operational voltage of the X-ray tube [65].

The polychromatic beam illuminates the sample where it diffracts as seen before. A monochromator is localized between the diffracted beam and the detector. This monochromator is a single crystal with almost no defect and a well-known lattice parameter. The crystal is adjusted, according to the Bragg's Law (Equation (3.1)), so that only those photons with the desired energy arrive at the detector. Usually it is chosen the wavelength corresponding to the characteristic X-ray of the metallic plate of the X-ray tube [65] that presents a high intensity and small FWHM. The XRD technique is widely used in materials science to identify the crystalline structure of the sample, obtaining the size of the crystallite and the lattice parameter of each phase present in the sample.

3.3 X-Ray Photoelectron Spectroscopy (XPS)

The XPS technique uses the photoelectron effect to obtain information about the chemical components, the oxidation state and the density of occupied states. This technique is sensitive to the surface of the analyzed material, which makes it interesting for the characterization of catalysts once the composition of the materials surface influences on the catalytic activity of the sample.

Figure 3.8 presents schematically the steps involved in the XPS measurement. The first step is the absorption of the photon by the electron in the atom, after the electron is emitted from the sample and lastly it enters into the analyzer, then being detected. Thus, the XPS measurement consists of illuminate the sample with an X-ray beam of energy hν and measure the kinetic energy of the ejected photoelectrons. This kinetic energy (E_k) can be calculated by:

$$E_k = h\nu - E_b - \varphi_{an} \tag{3.8}$$

where E_b is the binding energy of the ejected electron in the atom and φ_{an} is the analyzer's work function. For the measurements, the sample and the analyzer are connected to the ground, aligning their Fermi levels, thus the measured kinetic energy of the photoelectron depends on the analyzer's work function.

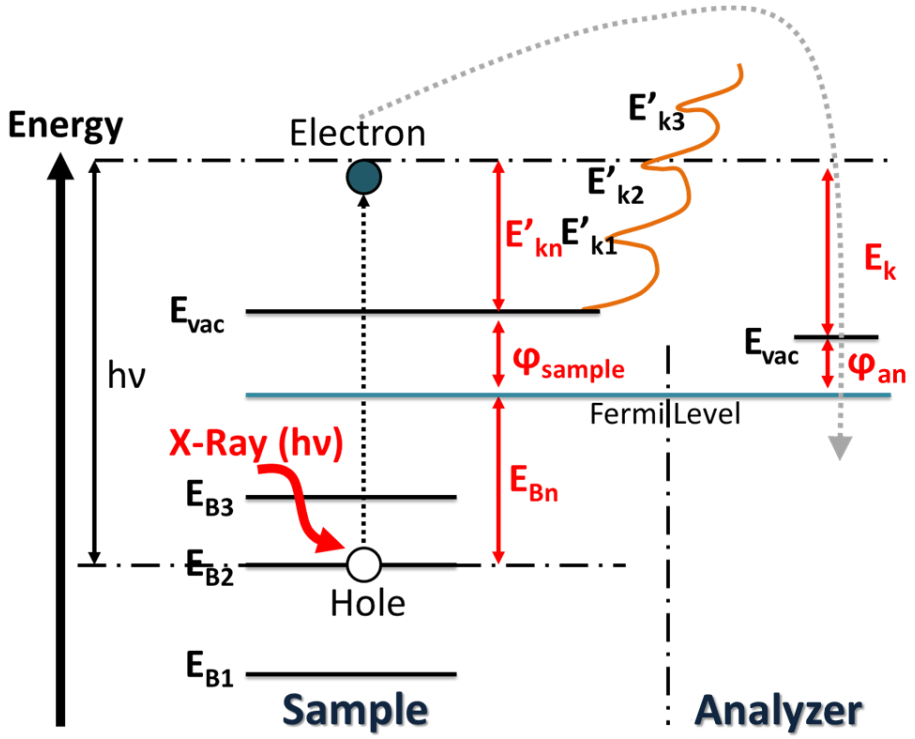

Figure 3.8: Schematic representation of the photoelectron effect where an incoming photon transfers its energy to an inner electron with a binding energy (E_{B2}). The electron is then emitted from the atom with a given kinetic energy (E_{k2}) and enters into the analyzer with a kinetic energy (E_k^a) which depends on the X-ray energy (hν), the binding energy of the electron and the work function (φ_{an}) of the analyzer, adapted from [66].

The kinetic energy of the photoelectron is dependent on the incident beam

energy, then not being an intrinsic property of the material. On the other hand, the binding energy depends only on the electronic structure and can be used to identify the chemical components existing in the sample. Considering this, the XPS spectra are commonly presented as a number of photoelectrons per second (intensity) as a function of their binding energy. Figure 3.9 shows an example of a XPS spectrum (long scan) of Cu-CeO_2 nanoparticles, where it is possible to identify the elements present in the sample. In this case, it is possible to identify the presence of Cu, Ce, O, Na and Cl because each chemical element appears as a specific set of peaks in the spectrum.

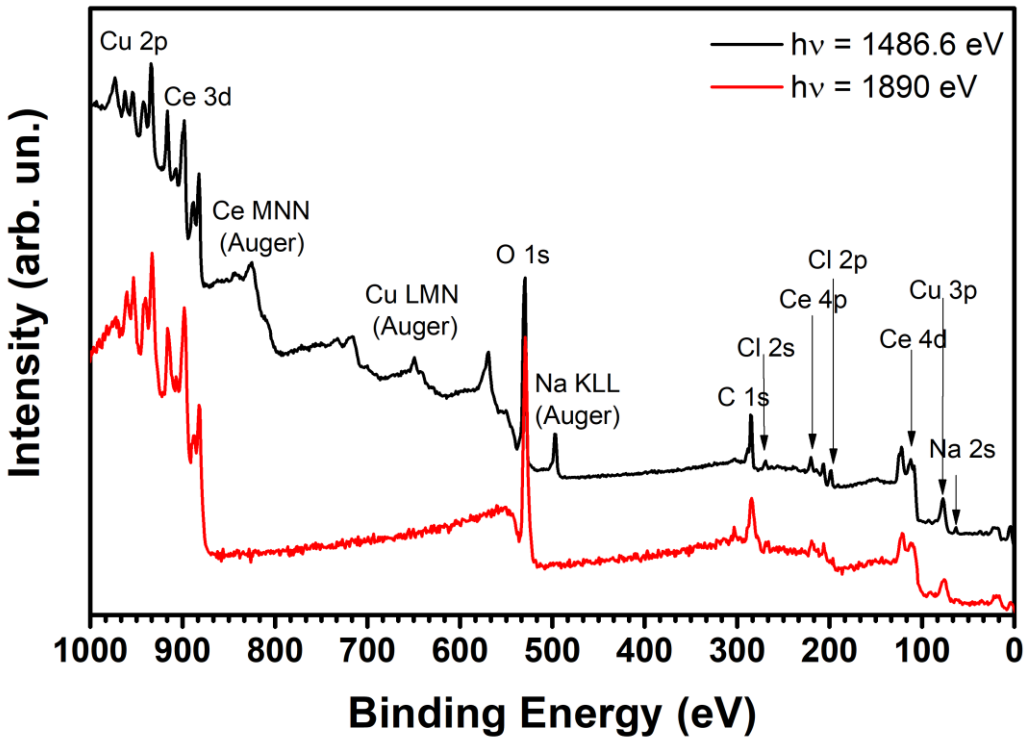

Figure 3.9: Comparison of the long scan spectra of Cu-CeO_2 nanoparticles using two different X-ray sources.

Figure 3.9 shows the characteristic peaks of the elements present in the sample. These peaks are labeled according to the quantum number of the electronic level that the photoelectrons were originated. The photoelectron peaks appear in the spectrum as doublets, except for the s level peaks, due to the spin-orbit splitting. The characteristic photoelectron peaks are formed by those photoelectrons that were excited and suffered only elastic scattering in the sample. The photoelectrons that undergo inelastic scattering before leaving the sample's surface contribute to the background of the

spectrum. After atomic ionization, the atomic relaxation occurs by emitting a characteristic X-ray or an Auger electron. These Auger electrons have a constant kinetic energy, which is related to the energy difference of the electronic levels involved in the relaxation process and that is independent of the incident X-ray beam energy. Then the Auger contribution can be identified by changing the incident X-ray energy. The characteristic photoelectron peaks appear at the same binding energy for both X-ray sources energies, while the Auger contribution shifts in the binding energy scale accordingly. In the Figure 3.9, the Auger peaks shifted to a higher binding energy value when the X-ray energy was changed from 1486.6 eV to 1890 eV, where the shift is equal to the energy difference of the X-ray sources used. This factor is commonly used to avoid Auger peaks near the characteristic peaks of the sample.

Figure 3.10 presents XPS spectra at the Cu 2p region for Cu(0) and CuO standards. It is possible to observe that the measured binding energy of the Cu $2p_{3/2}$ electronic level is clearly different for each compound. It occurs because the energy level of core electrons depends on the atomic chemical state. In the major part of cases, the binding energy is proportional to the oxidation state and the electronegativity of the ligands. Thus, with a high resolution XPS spectrum is possible to obtain the oxidation state of the sample.

The binding energy of a photoelectron peak can be explained considering that the kinetic energy of the photoelectron is not influenced by the relaxation effects of the ionized atom, which is known as sudden approximation. It means the photoelectron leaves the atom and does not interact strongly with the ionized atom. However, in some cases the photoelectron emission process is slow and the emitted photoelectron interacts with the ionized atom. In this case, the photoelectron loses energy promoting another atomic electron to a higher energy level or to the continuous, which is known as shake-up and shake-off processes, respectively. It gives an additional peak with higher binding energy (due to the smaller kinetic energy) in the XPS spectrum, as shown in Figure 3.10 (b).

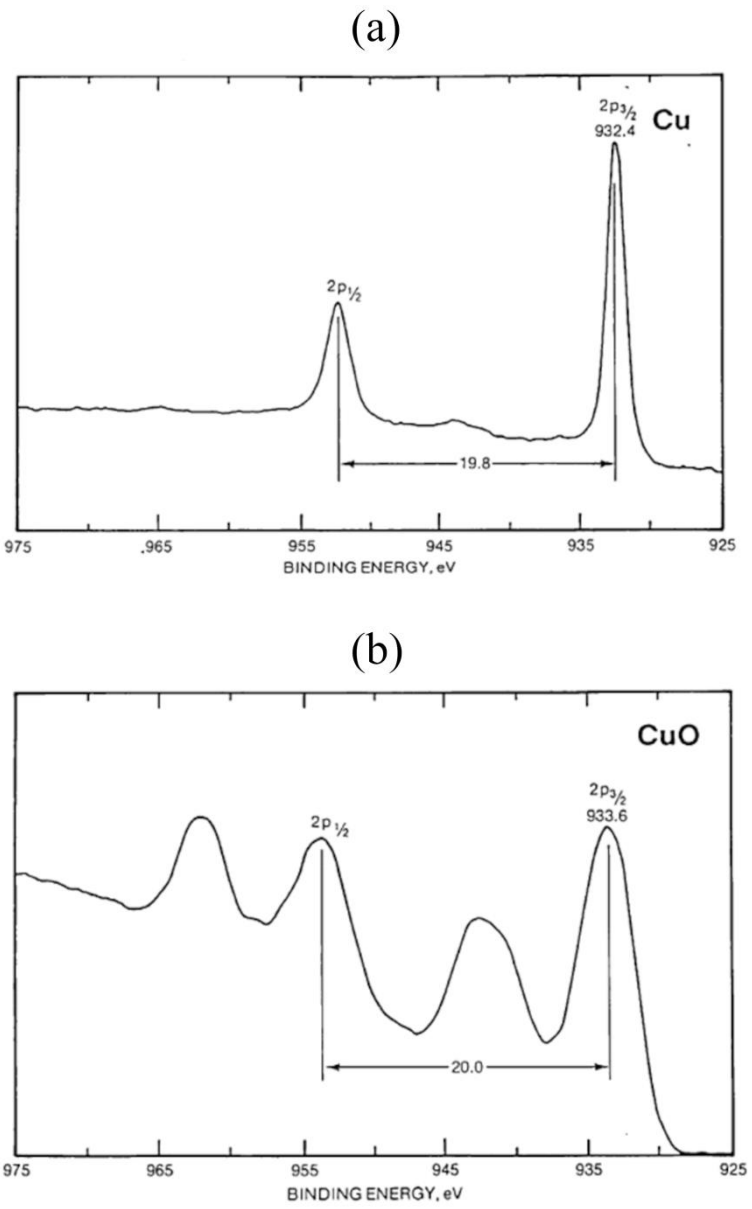

Figure 3.10: XPS spectra at the Cu 2p region of (a) Cu(0) and (b) CuO standards [67].

The intensity of the characteristic photoelectric peak can be calculated by

$$I = F_x \cdot S(E_k) \cdot \frac{d\sigma_{nl}(E_k)}{d\Omega} \cdot \int_0^{\infty} n(z) \cdot e^{-z/\lambda_{IMFP}(E_k)cos\phi} dz \qquad (3.9)$$

where I is the intensity of the XPS peak (area), F_x is the X-ray flux on the sample, $S(E_k)$ is the analyzer efficiency for detecting the electron at kinetic energy E_k, $\frac{d\sigma_{nl}(E_k)}{d\Omega}$ is the photoionization differential cross-section for the atomic level nl, n(z) is the concentration of the element in the sample (number of atoms per unit volume), z is the depth below the surface where the photoelectron is emitted, $\lambda_{IMFP}(E_k, z)$ is the inelastic

mean free path of the photoelectron at kinetic energy E_k and ϕ is the take-off angle, that is, the angle between the direction in which the photoelectron is emitted and the surface normal.

The inelastic mean free path is the average distance travelled by a photoelectron in the sample before suffering an inelastic collision. The probing depth of XPS depends on the kinetic energy of the photoelectron and is usually taken as $3\lambda_{IMFP}$. Figure 3.11 presents a graph of the inelastic mean free path of the photoelectrons (λ_{IMFP}) as a function of the kinetic energy for some specific elements. It shows that the inelastic mean free path does not depend on the elements present in the solid, but on the energy of the emitted photoelectron. It means that different depths can be probed by changing the kinetic energy of the photoelectron, which, in accordance to Equation (3.8), can be achieved by changing the incident photon energy or the electronic level probed (change on E_b value).

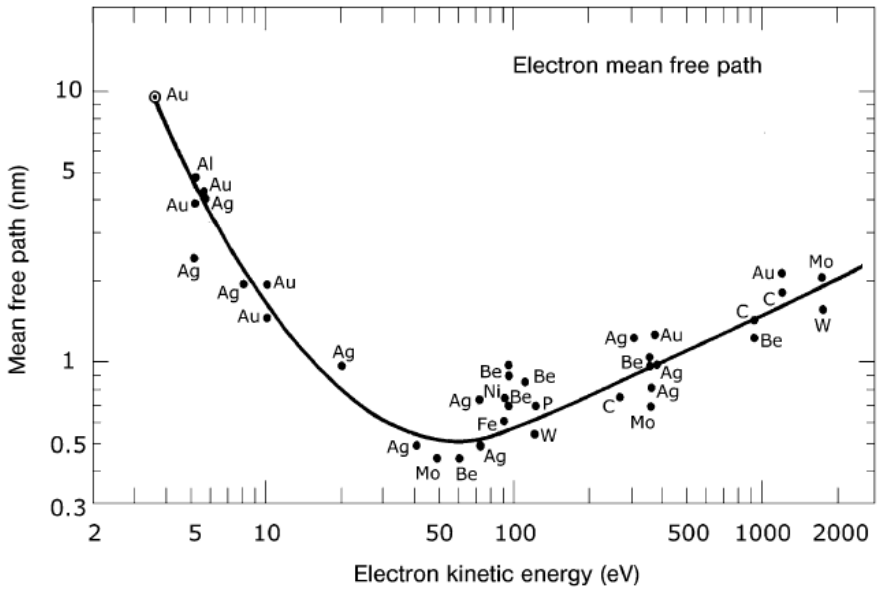

Figure 3.11: Inelastic mean free path of the photoelectrons in a solid as a function of the kinetic energy of the emitted photoelectron [68].

The photoionization cross-section (σ_{nl}) is related to the probability of ionizing an atom by the incident X-ray beam. This probability is related to the element and electronic level considered and the incident photon energy. The differential cross-section is related to the probability of ionizing an atom by the incident X-ray beam emitting a photoelectron in a specific angle. For an unpolarized X-ray beam, the differential cross-section is given by

$$\frac{d\sigma_{nl}(E_k)}{d\Omega} = \frac{\sigma_{nl}(E_k)}{4\pi}\left[1 + \frac{1}{2}\beta_{nl}(E_k)\left(\frac{3}{2}\sin^2\alpha - 1\right)\right] \quad (3.10)$$

where β_{nl} is the angular asymmetry factor and α is the angle between the direction of incident beam and the emission of the photoelectron [69]. The asymmetry factor takes into account the non-isotropic nature of the photoemission. For a polarized X-ray beam, the differential cross-section can be obtained from

$$\frac{d\sigma_{nl}(E_k)}{d\Omega} = \frac{\sigma_{nl}(E_k)}{4\pi}\left[1 + \beta_{nl}(E_k)\left(\frac{3}{2}\cos^2\gamma - \frac{1}{2}\right)\right] \quad (3.11)$$

where γ is the angle between the polarization of the incident beam and the photoemission direction [69].

After being ejected from the sample the photoelectron may enter into the electron analyzer, which can be of different geometries like the cylindrical mirror analyzer (CMA) or the hemispherical sector analyzer (HSA). The most commonly used is the HSA, which has higher energy resolution but lower sensitivity than the CMA. In both analyzers, the electrons are dispersed along a radial or axial coordinate due to its kinetic energy [70, 69]. Figure 3.12 shows a schematic representation of the HSA which consists of two concentric hemispherical electrodes (inner and outer hemispheres). A potential difference is applied on the electrodes, then selecting only those photoelectrons with a specific kinetic energy to arrive at the detector. This kinetic energy (known as pass energy) can be calculated by Equation (3.12):

$$E_k = e\Delta V\left(\frac{a \cdot b}{b^2 - a^2}\right) \quad (3.12)$$

where e is the electron charge, ΔV is the potential difference applied in the electrodes and a and b are the radii of the inner and the outer hemispheres, respectively, as shown in Figure 3.12. The HSA may operate in two distinct modes, the constant analyzer energy (CAE) and constant retard ratio (CRR) mode. In the CAE mode, the voltage difference between the hemispheres is kept in a constant value, which means that the pass energy is constant and set by the user. The electrons are retarded before entering in the hemispheres region. Then the voltage used to retard the photoelectrons is changed in order to select photoelectrons with different kinetic energies to be detected. This is the

most used mode because the pass energy is related to the energy resolution and transmission rate of the electrons. A high pass energy provides a higher transmission rate but poorer resolution, while a low pass energy provides an improved resolution but worst transmission rate.

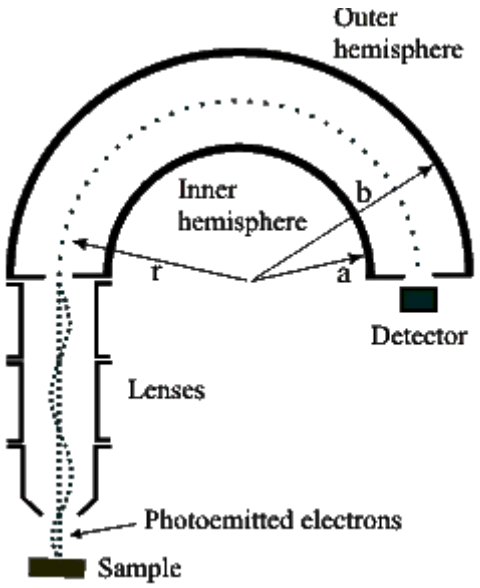

Figure 3.12: Schematic representation of a HSA analyzer where only electrons with a specific kinetic energy arrive at the detector [71].

3.4 Mass Spectrometry

The Mass Spectrometry is a technique that can be used to identify the products of a catalytic reaction. This technique is based on the use of a magnetic field that sorts the ions according to the mass to charge ratio (m_i/q). Firstly, the molecule is ionized and then a force F_m is applied to the charged particle by the magnetic field, usually perpendicularly to the charged particle trajectory. This force can be calculated by:

$$\vec{F}_m = q\left(\vec{v} \times \vec{B}\right) = qvB\hat{e}_r \tag{3.13}$$

where q is the charge of the particle, $\vec{v}$ is the velocity, $\vec{B}$ is the applied magnetic field vector and $\hat{e}_r$ is the unity vector in the radial direction $\vec{r}$. The Equation (3.13) shows that the force $\vec{F}_m$ is perpendicular to the plane given by the velocity and magnetic field vectors. In other words, the charged particle travels in a circular path in the region where the magnetic field is applied. The radius (R) of this trajectory can be obtained by:

$$R = \frac{m_i v}{|q|B} \tag{3.14}$$

Figure 3.13 presents the mass spectrum of pure CO_2. It is presented the relative intensity as a function of the mass to charge value. It can be notice that the peak related to the mass of CO_2 (44) is the most intense one. The following peaks, with a (m_i/q) of 45 and 46 are related to the CO_2 with the isotopes of the carbon (C^{13}) and oxygen (O^{18}), respectively. The intensity of these peaks is related to the fraction of each isotope in the nature. It is possible to observe in Figure 3.13 a peak with a (m_i/q) ratio of 22, which refers to a CO_2 molecule that had lose two electrons instead of one. The others peaks with a (m_i/q) ratio lower than 44 are related to breaking the CO_2 molecule into CO, C and O after entering the mass spectrometer.

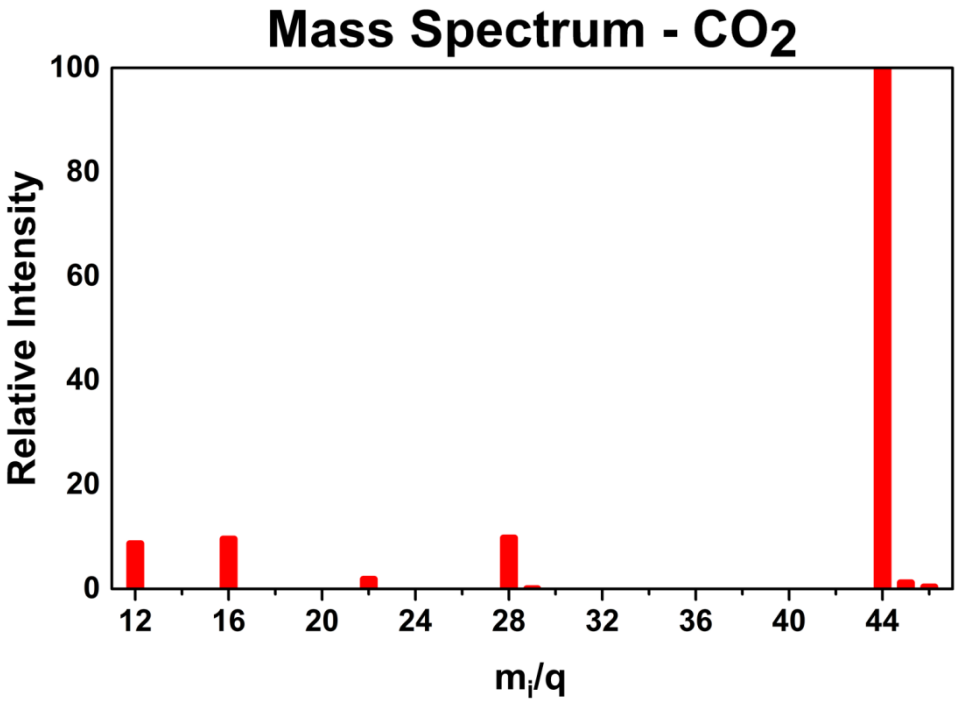

Figure 3.13: Mass spectrum of the CO_2 molecule [72].

The mass spectrometer can be divided in three main parts, the ionization source, the mass analyzer and the detector. Figure 3.14 shows the schematic representation of a mass spectrometer, where the analyzed gas is ionized by the collision with electrons. The ionized molecules are accelerated by a potential difference to a specific velocity v, which depends on the applied potential. In the analyzer, the ions are sorted according to the (m_i/q) ratio. There are many different ways of separating the masses, but all of them

include the application of an electric or a magnetic field that change the trajectory or the velocity of the ion. In Figure 3.14, when a uniform magnetic field is applied the trajectory of the ion changes, following Equation (3.14). It is possible to notice that the radius of the trajectory is different for the different mass to charge ratio of the ions, as can be seen in Figure 3.14. The ion mass can be identified by its position when it arrives at the detector [73]. The Mass Spectrometry allows the identification of the compounds present in the analyzed gas. The measurement can be carried out along a catalytic reaction, monitoring the evolution of the products formed as a function of reaction time.

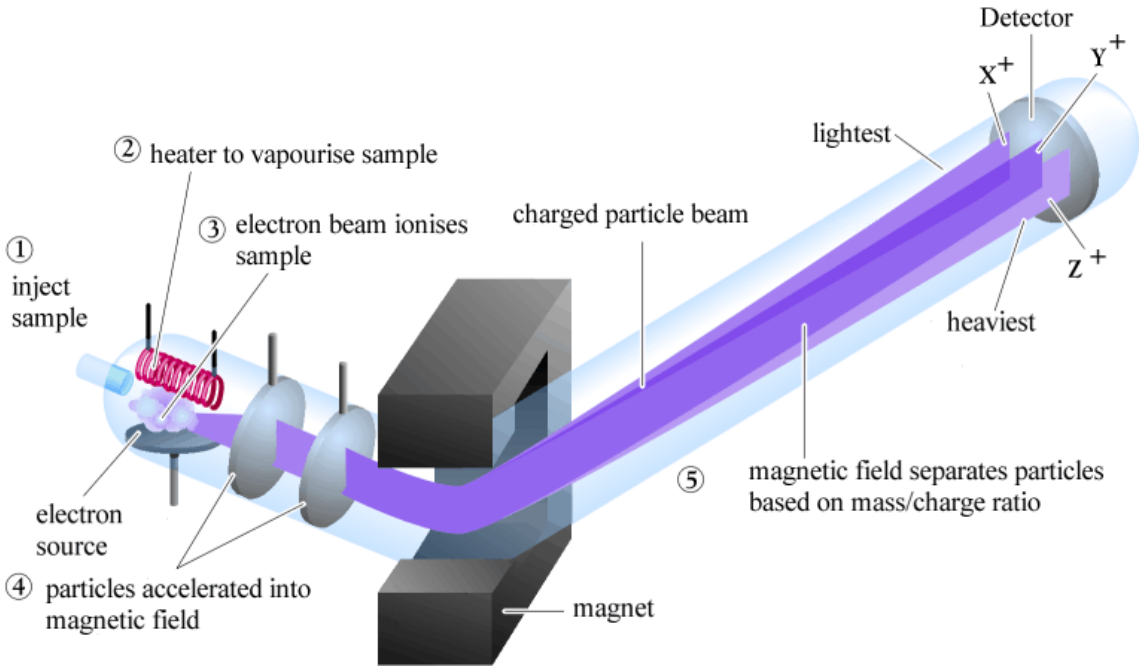

Figure 3.14: Schematic representation of a mass spectrometer equipment [74].

3.5 Synchrotron Radiation

The synchrotron light is a polychromatic radiation emitted by relativistic charged particles when deflected by a magnetic field in a circular trajectory. In a synchrotron light lab, the electrons are initially emitted by an electron gun (usually generated by thermionic emission from a hot filament) and accelerated in a linear accelerator (linac) to around 100 MeV. The electrons are later inserted in the booster ring where they are accelerated to the final energy of a few GeV. After achieving this energy, they are injected in the storage ring. The electrons must be periodically injected in the storage ring because the electron current decreases due to collision with residual

gas molecules inside the main ring. The electrons are kept in a closed path inside the storage ring by a set of magnets. As seen previously, a charged particle moving through an uniform magnetic field applied perpendicularly to its trajectory follows a curved path. In this way, the electron is deflected when crossing the magnetic field region due to a magnetic dipole, named bending magnet, then emitting electromagnetic radiation. The radiation emitted from a bending magnet covers the electromagnetic spectrum from infrared to hard X-rays. There are also quadrupole magnets (used to focus the electron beam) and sextupole magnets (used to correct chromatic aberrations from the use of quadrupoles). Figure 3.15 shows that in the storage ring there are auxiliary components, beside the magnets, such as the radio frequency supply and insertion devices (*undulators* and *wigglers*). The radio frequency supply is responsible for providing to the electron the energy lost due to the emission of the synchrotron radiation or collision with molecules. While the bending magnet is used to bend the electron trajectory, the insertion devices are used in the straight sections of the storage ring to produce synchrotron light of higher brightness. To achieve this, the insertion devices are composed of many alternated magnets and, because of the alternating magnetic field produced, the electrons follow an undulating trajectory, emitting radiation at each bend and generating a much more brilliant radiation beam than that generated by a single magnet. Depending on the period of the alternating magnets and other characteristics, the light produced in these devices may have a better time or energy resolution, which differentiates between both insertion devices.

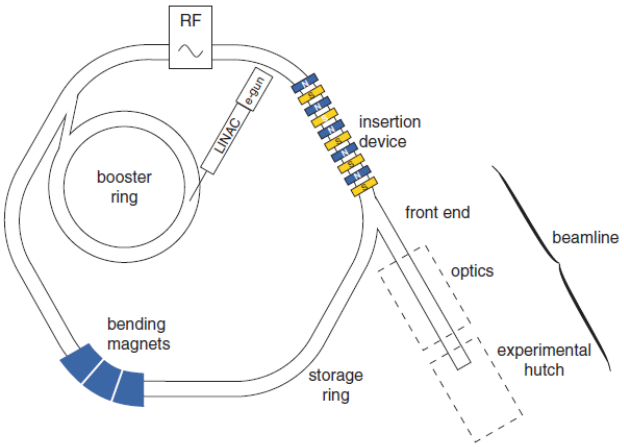

Figure 3.15: Schematic representation of the main components of a synchrotron light source [75].

After being emitted, the synchrotron light is focused to the beamline, positioned

tangentially to the storage ring. Each beamline has a different configuration depending on the requirements of the experiment that are performed there, although many components are common to most beamlines. For example, after being emitted the radiation is usually focused by X-ray mirrors on the monochromator which, similarly to that used in the XRD technique, is typically composed by a monocrystal where the energy of the X-ray is selected according to Bragg's Law. Later, the monochromatic X-ray beam is focused on the sample by mirrors or refractive Fresnel lenses. The sample is fixed in a custom sample holder that is exposed to the experimental conditions (temperature, reactant gases, pressure…). Lastly, there are the detectors (CCD, ionization chambers…) that are used to measure the data of the performed experiment [76].

The main characteristics of the synchrotron light are: (i) high brilliance, many order of magnitude higher than the conventional X-ray tube brilliance; (ii) low emittance, meaning that the beam is highly collimated; (iii) extremely short pulses (< 10^{-12} s); (iv) variable polarization and (v) wide frequency range available. Thereby, state-of-the-art experiments with nice time and spatial resolution can be performed [75]. All these characteristics make the synchrotron light very interesting for many analysis techniques, such as XRD, XPS and X-Ray Absorption Spectroscopy (XAS).

3.6 X-Ray Absorption Spectroscopy (XAS)

The XAS technique consists of measuring the X-ray absorption coefficient as a function of the incident X-ray beam energy. A monochromatic X-ray beam is focused on the sample and the intensity of the transmitted beam is measured to obtain the absorption coefficient by using the Beer-Lambert's law. It relates the intensity of the transmitted beam with the thickness and the absorption coefficient of the sample. According to the Beer-Lambert's law, the intensity of the transmitted beam decreases exponentially with the increase of the sample thickness and the absorption coefficient [75] as shown in Equation (3.15):

$$I = I_o \, e^{-\mu(E)t} \tag{3.15}$$

where I is the intensity of the transmitted beam, I_o is the intensity of the incident beam,

μ(E) is the absorption coefficient that depends on the energy of the incident beam and t is the sample thickness. The photon absorption occurs with the electron transition from the initial electronic level to an unoccupied electronic level or to the continuum, depending on the photon energy. In the second case, the photoelectrons have a kinetic energy given by:

$$E_k = h\nu - E_b \tag{3.16}$$

where E_k is the kinetic energy of the photoelectron, hν is the photon energy and E_b is the binding energy of the electron in the atom.

Figure 3.16 presents the XAS spectrum at the Cu K edge of a Cu(0) standard sample. The X-ray absorption coefficient is zero for incident beam energies smaller than the binding energy of the electrons at the 1s electronic level of Cu (8979 eV). When the beam reaches the energy required to excite the electrons from the 1s to the 4p electronic level of Cu, the absorption coefficient increases significantly. The region of this abrupt increase on the absorption coefficient is named absorption edge. For higher incident energies, whether the Cu atoms absorb the X-ray photon the photoelectrons are ejected with non-zero kinetic energy and some oscillations on the absorption coefficient are observed in this energy region. The XAS spectrum is divided in two energy regions: the XANES (X-Ray Absorption Near Edge Structure), which comprises the region before the absorption edge until, typically, 50 eV to 100 eV after absorption edge, and the EXAFS (Extended X-Ray Absorption Fine Structure), that is the region from the end of XANES until the end of the XAS spectrum.

During the XAS measurements, the monochromatic beam is focused on the sample and its intensity is detected before and after being transmitted by the sample by using ionization chambers. The absorption spectrum is obtained by changing the incident photon energy in a specific range. The absorption edge energy is related to a specific atom and transition, allowed by the dipole transition rule.

The XAS technique is widely used in catalysis since it allows *in situ* measurements, i.e., XAS measurements with the sample exposed to high temperatures and pressures of the reacting gases. Therefore, this technique can be used to study changes in the electronic and structural properties of the sample with the increase of the

pressure of reacting gases and with the increase of the sample's temperature.

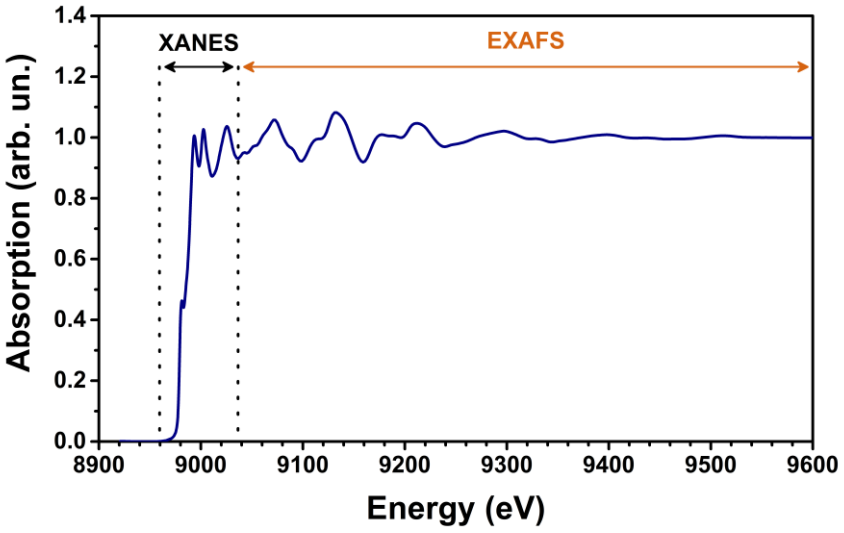

Figure 3.16: XAS spectrum at the Cu K edge of a Cu(0) standard sample.

The XAS measurements, besides being performed *in situ*, can be conducted with time resolution. This makes the technique ideal for the study of the catalytic reaction kinetics since it allows the observation of the electronic changes in the sample in real time during a catalytic reaction. In order to measure *in situ* time-resolved XAS, a fast measurement mode is required. One of the possibilities is to use a monochromator made of a curved crystal. Figure 3.17 shows a schematic representation of the system used at the DXAS beamline of LNLS, which is dedicated to performing *in situ* time-resolved XAS measurements. The polychromatic beam is focused on the curved Si monochromator, which is curved to allow the variation of the incidence angle. Thus, from Bragg's law (Equation (3.1)), it is possible to notice that a polychromatic beam is produced which will illuminate the sample, positioned at the focus of the beamline. The transmitted beam is detected by a CCD camera, where the beam energy is determined by the position it reaches the detector.

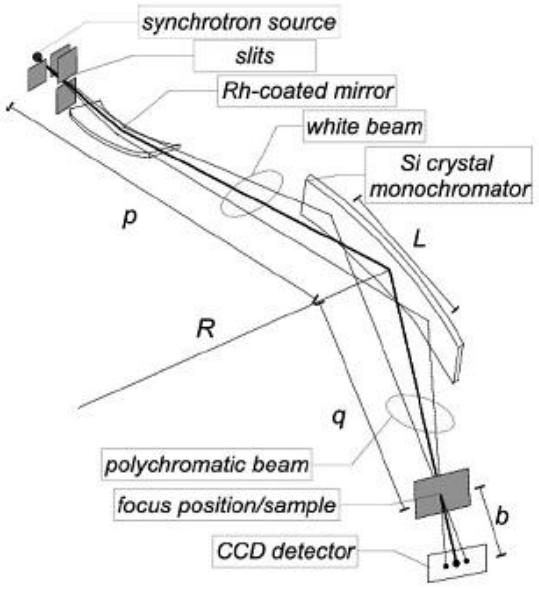

Figure 3.17: Schematic representation of the DXAS-LNLS beamline showing the optical system, a curved Si monochromator and a CCD detector [77].

3.6.1 X-Ray Absorption Near Edge Structure (XANES)

In the absorption edge region of the XAS spectrum, the first maximum in the absorption coefficient occurs due to the excitation of the electrons from the electronic core level to an upper unoccupied electronic level of higher energy. The intensity of this maximum is related to the density of unoccupied electronic states in the upper energy level. In this way, the comparison between different samples allows determining the variation of the density of unoccupied states due to the oxidation state of the absorbing atom. The shape of the following XANES oscillations depends on the neighbors of the absorbing atoms, including their identity and coordination number. Figure 3.18 shows a comparison between different XANES spectra of Cu compounds, which have different oxidation states. The measurement at the Cu K edge corresponds to an electronic transition from the 1s to the 4p electronic level of Cu. It is possible to observe, for example, that the Cu(0) presents the maximum after the absorption edge with the lowest intensity. This happens because the metallic Cu presents the lowest number of unoccupied states in the 4p electronic level since the oxidation number is zero. Besides this, the energy position of the absorption edge also depends on the oxidation state of the absorbing atom and the energy typically increases with the oxidation number.

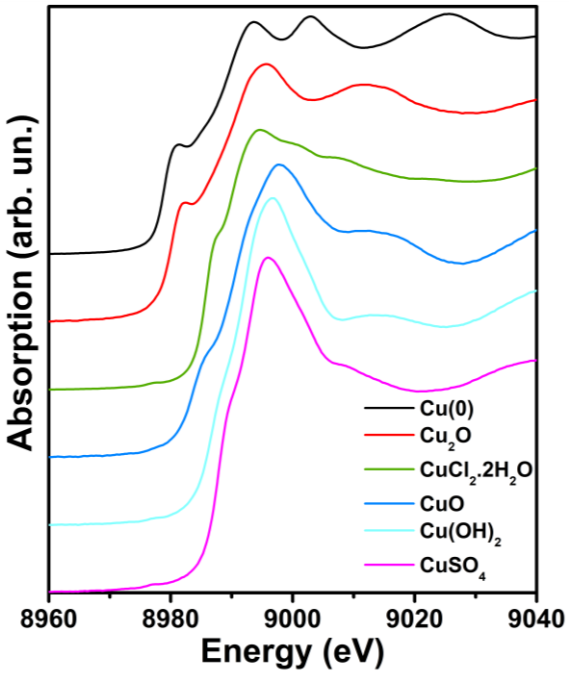

Figure 3.18: Comparison between XANES spectra measured at the Cu K edge for different Cu compounds.

The absorption coefficient is directly related to the probability of the electronic transition by absorption of the photon from the initial core level to the upper unoccupied state with a higher energy level. The transition follows the electric dipole selection rule. In this approximation, the absorption coefficient can be described by the Fermi's golden rule, which, for a single atom a, can be described as:

$$\mu_{\mathrm{a}}(E) \propto \sum_{f} |\langle f|\hat{\mathrm{e}}\cdot\boldsymbol{r}|i\rangle|^{2}\,\delta(E-E_f) \qquad (3.17)$$

where $\hat{\mathrm{e}}\cdot\mathbf{r}$ is the dipole operator, a represents the absorbing atom and $|i\rangle$ and $|f\rangle$ represent the initial and final state of the atom, respectively.

A secondary edge located in energies smaller than that of the absorption edge may appear and is known as pre-edge. This edge cannot be explained only by the dipole selection rule and it occurs due to hybridization effects and the occurrence of other electronic transitions like the quadrupole transition, which has a lower probability to occur than the dipole transition, giving a peak of lower intensity.

The XANES spectrum is commonly fitted using Linear Combination Analysis

(LCA), which uses a linear combination of the reference's spectra to fit the XANES region measured. Figure 3.18 presents some Cu K edge reference's spectra and it is possible to notice that the curve shape is characteristic for each compound, as discussed above. Hence, with the XANES measurement, it is possible to obtain the percentage of each compound present in the sample. More sophisticated methods can be employed, including ab initio calculation aiming to reproduce the XANES features from a proposed model.

3.6.2 Extended X-Ray Absorption Fine Structure (EXAFS)

The EXAFS oscillations appear in the XAS spectrum and allow probing the local atomic order around an absorbing atom. It gives the mean distance between the absorbing atom and its neighbors, the coordination number and information about thermal and structural disorder of the sample [78].

Figure 3.19 shows a schematic representation of the origin of the EXAFS oscillations. After ejected from the absorbing atom, the photoelectron travels through the sample and can be seen as a wave. The photoelectron wave can be backscattered by the neighboring atoms, returning to the absorbing atom. The backscattered photoelectron wave interacts with the original photoelectron wave interfering constructively or destructively depending on the distance between the atoms, phase and the photoelectron wavelength. The constructive interference increases the X-ray absorption coefficient since the electron density at the absorbing atom increases, while in a destructive interference it decreases, then explaining the EXAFS oscillations after the absorption edge. The de Broglie wavelength (λ_e) associated to the photoelectron can be calculated by:

$$k = \frac{2\pi}{\lambda_e} = \sqrt{\frac{2m_e \cdot (h\nu - E_b)}{\hbar^2}} \tag{3.18}$$

where k is the photoelectron's wave vector, m_e is the electron mass, hν is the photon energy, E_b is the binding energy of the electron in the atom and $\hbar$ is the reduced Planck constant.

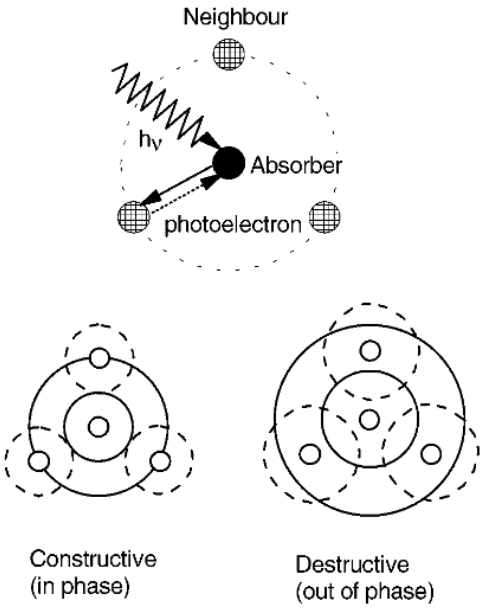

Figure 3.19: Schematic representation of the photoelectron backscattering process by the neighboring atoms [79].

Figure 3.20 shows the XAS spectra of a Kr sample in different temperatures and phases. The gas and liquid phases' measurements are very close to the single atom measurement since they present almost no oscillatory behavior. It is in accordance to the explanation for the existence of the EXAFS oscillations after the absorption edge.

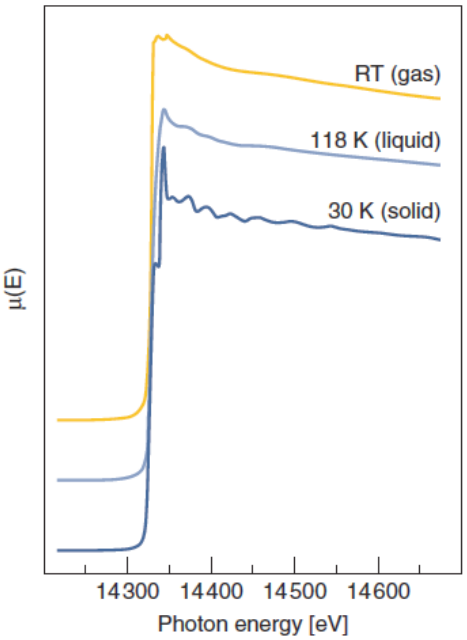

Figure 3.20: XAS measurements at the Kr K edge for a Kr sample in the gas, liquid and solid phase [75].

Figure 3.21 (a) presents the XAS spectrum at the Cu K edge for a Cu(0) standard

and the theoretical single atom contribution ($\mu_0(E)$). It can be noticed that the amplitude of the EXAFS oscillations is only few percent of the overall X-ray absorption coefficient. The oscillations in the EXAFS region (χ) may be isolated from the measured data ($\mu(k)$) by

$$\chi(k) = \frac{\mu(k) - \mu_0(k)}{\mu_0(k)} \tag{3.19}$$

where $\mu_0(k)$ is the single atom XAS spectrum, which is approximated by an smooth absorption background. The EXAFS oscillations, Figure 3.21 (b), are typically presented in function of k, which is the photoelectron wavenumber as presented in Equation (3.18).

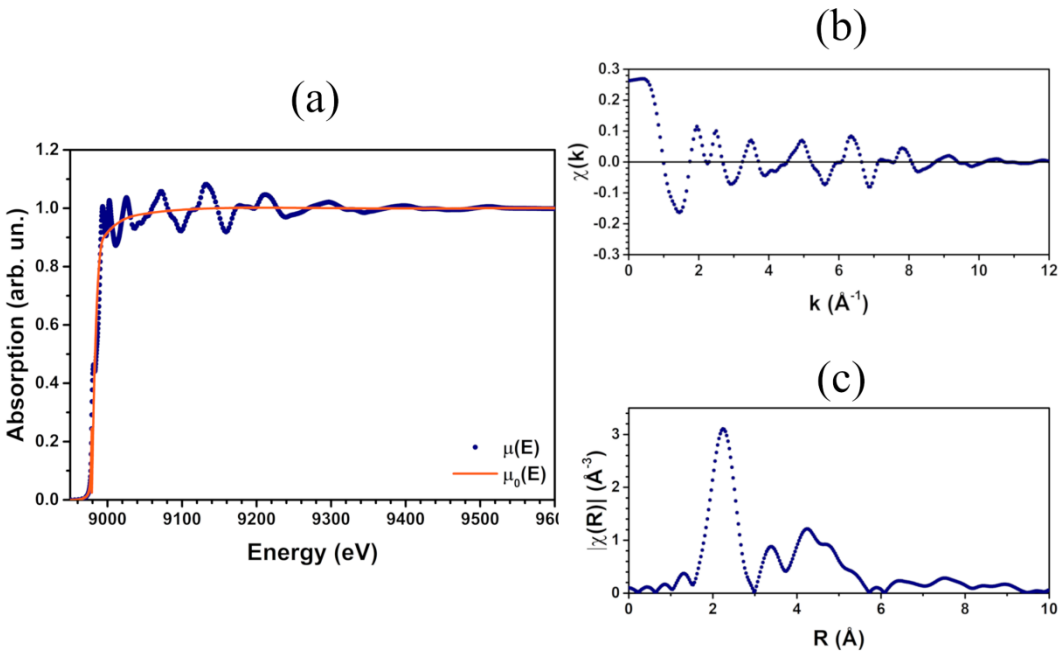

Figure 3.21: (a) XAS measurement at the Cu K edge for a Cu(0) standard ($\mu(E)$) and the calculated single atom contribution ($\mu_0(E)$), (b) the respective EXAFS oscillations and (c) Fourier Transform.

The $\chi(k)$ function contains important information about the atomic structure around the absorbing atom, and is given by a sum over contributions from different atomic shells around the absorbing atom:

$$\chi(k) = \sum_j S_0^2 \cdot N_j \cdot e^{-2\cdot k^2 \cdot \sigma_j^2} \cdot e^{-2\frac{R_j}{\lambda(k)}} \cdot \frac{f_j(k,\theta)}{k \cdot R_j^2} \cdot \sin\left(2 \cdot k_j \cdot R_j + \delta_j\right) \tag{3.20}$$

where $f_j(k, \theta)$ is the scattering amplitude of the photoelectron with a wave vector k in an angle θ by the neighboring atoms and δ_j is the phase shift of the scattering process. The coordination number (N_j) is the number of atoms with the same identity localized at approximately the same distance from the absorbing atom. The term $\exp(-2R_j/\lambda(k))$ is the attenuation of the wave function amplitude when the photoelectron travels in a solid. The EXAFS oscillations depend on the interatomic distance (R_j) between the absorbing atom and the scatterers. This dependence is included also as a sinusoidal behavior ($\sin(2k_j \cdot R_j)$). The $\lambda(k)$ term depends on the inelastic mean free path (λ_{IMFP}) of the photoelectron and the lifetime of a hole in a deep electronic level. It is usually in the order of a few angstroms in the EXAFS measurements, which means that only the atoms near the absorbing atom can be analyzed. The amplitude reduction factor (S_0^2) is related to intrinsic processes of energy loss. It is a many-body effect that is related to the absorbing atom relaxation process and affects the wave amplitude of the photoelectron. The Debye-Waller factor is taken into account by the factor $\exp(-2\sigma_j^2 k^2)$. This factor is a convolution of the thermal and structural disorder. The thermal disorder is mostly given by the oscillation of the atoms around their equilibrium position due to the thermal energy. The Debye-Waller factor increases with the increase of the temperature, as the atoms oscillate with higher amplitude, increasing the thermal disorder. This factor influences on the amplitude of the EXAFS oscillations.

The amplitude of the EXAFS oscillations $\chi(k)$ generally deceases with the increase of k, as can be observed in Figure 3.21 (b), therefore the $\chi(k)$ is usually weighted by k, k^2 or k^3. The different k-power options are used to enhance the signal from elements with higher or lower atomic number (Z) around the absorbing atom.

It is convenient to Fourier transform the $\chi(k)$ oscillations in order to analyze the data in the real space [80]. It is obtained by:

$$\tilde{\chi}(R) = \frac{1}{\sqrt{2\pi}} \int_{k_{min}}^{k_{max}} k^{\omega} \chi(k) e^{i2kR} dk \qquad (3.21)$$

Figure 3.21 (c) presents the k^2-weighted Fourier Transform of the EXAFS oscillations $\chi(k)$ (Figure 3.21 (b)). The Fourier Transform is interpreted with the presence of the absorbing atom at R = 0 and every peak represents an atomic shell

around the absorbing atom.

The analysis of the EXAFS oscillations and the corresponding Fourier Transform is performed by firstly proposing an atomic cluster and then calculating the $f_j(k,\theta)$ and δ_j factors. After, the data are fitted varying parameters that are obtained from the EXAFS analysis, such as the coordination number, Debye-Waller factor and distance between the absorbing and neighbor atom. For the theoretical calculation of the $f_j(k,\theta)$ and δ_j factors it is commonly used the *muffin tin* potential, represented in Figure 3.22. This potential is characterized by spherically symmetric scattering potentials centered in the atoms position and a constant potential between the atoms.

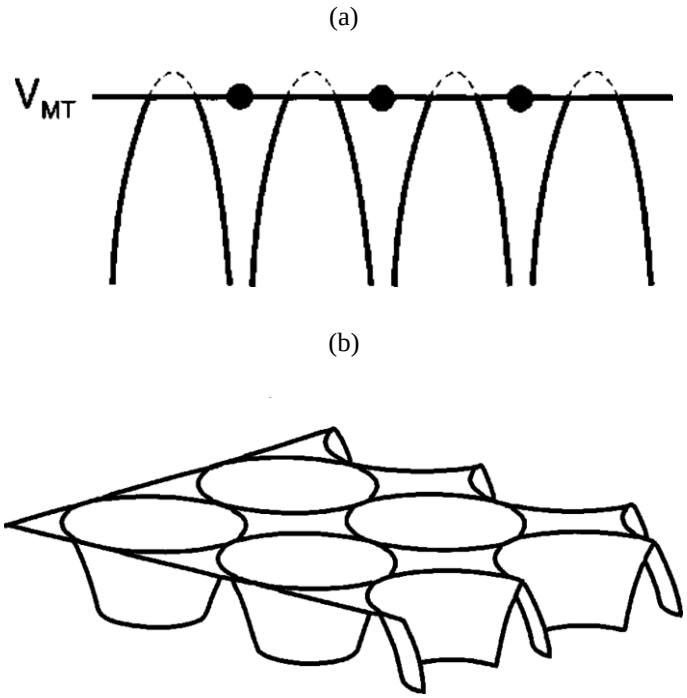

Figure 3.22: Schematic representation of (a) one-dimensional and (b) two-dimensional muffin-tin potential. The atoms are represented by a symmetrically spherical potential, with a constant potential in the region between the atoms [78].

The EXAFS oscillations are the result of the interference between many photoelectron wave functions from many different possible paths of the photoelectron ejected by the absorbing atom. The photoelectron can take a single- or a multiple-scattering path, depending on the number of backscattering events it suffered. The single path occurs with a single backscattering event in a neighbor atom while the multiple one occurs with two or more backscattering events in the neighbor atoms. Some of these possible paths are represented in Figure 3.23. Therefore, a multiple-

scattering theory should be used in combination with the muffin tin potential, besides the use of curved waves to calculate the scattering amplitude and phase shift of the scattering.

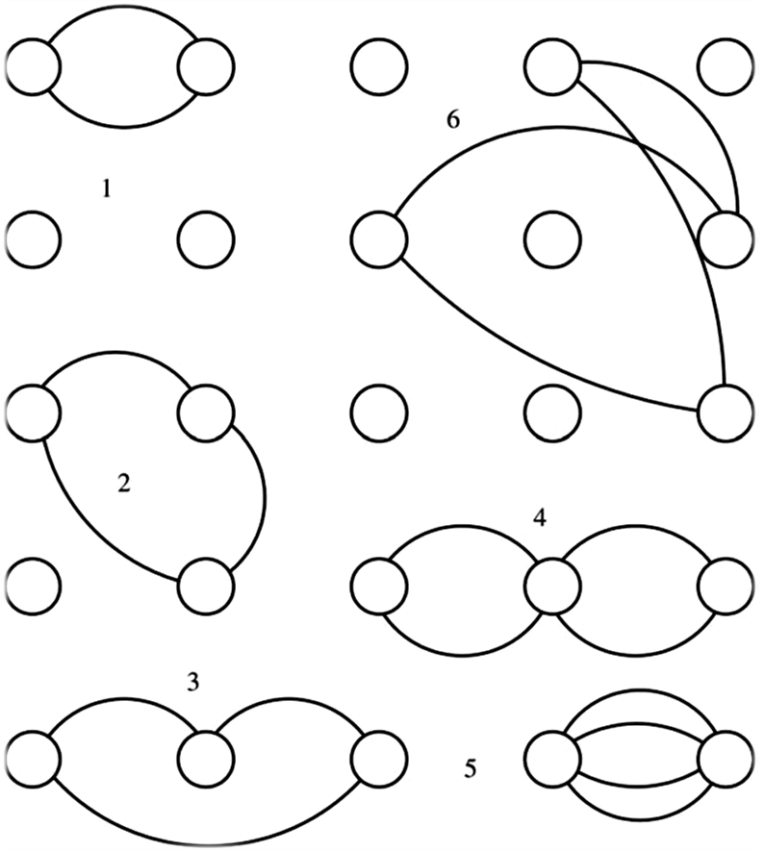

Figure 3.23: Example of the different scattering paths the photoelectron can take including single- and multiple-scattering paths.

In the multiple-scattering theory [78, 81], the Fermi's Golden rule is re-written using a one-particle Green function (*G*), which describes all possible scattering paths that the photoelectron can take. The system's Green function can be written as:

$$G(E) = \frac{1}{E - \mathcal{H} + \mathrm{i}\zeta} \tag{3.22}$$

where $\mathcal{H}$ is the Hamiltonian of the system given by:

$$\mathcal{H} = \mathcal{H}_0 + V_{int} + \delta V \tag{3.23}$$

where V_{int} is the constant interstitial potential between the atoms (in accordance to the muffin-tin approximation) and δV is the scattering potential of the ions. Equation (3.17)

can now be written using Equation (3.22) as

$$\mu_a(E) \propto -\frac{1}{\pi}\, Im\, \langle i|\hat{e}^* \cdot \boldsymbol{r} G(E) \hat{\mathrm{e}} \cdot \boldsymbol{r}|i\rangle \Theta(E - E_F) \tag{3.24}$$

where $\Theta(E\text{-}E_F)$ is the Heaviside step function.

The Green function G(E) is the full propagator in the presence of the scattering potential and can be expressed in series by the Dyson equation

$$G = G^0 + G^0 T G^0 \tag{3.25}$$

where G^0 is the free-electron propagator given by

$$G^0 = \frac{1}{E - \mathcal{H}_0 + i\zeta} \tag{3.26}$$

and T is the full atomic scattering matrix represented by

$$T = V + VGT = t + tG^0 t + tG^0 tG^0 t + \cdots \tag{3.27}$$

where *t* is the single site scattering matrix. Replacing T (Equation (3.27)) in the Equation (3.25),

$$\begin{aligned} G &= G^0 + G^0 t G^0 + G^0 t G^0 t G^0 + \cdots \\ &= (1 - G^0 t)^{-1} G^0 \end{aligned} \tag{3.28}$$

The G can be identified as a Taylor expansion. Applying Equation (3.28) in Equation (3.24), it is possible to obtain

$$\mu_a(\varepsilon) = \mu_0(\varepsilon)[1 + \chi_l(\varepsilon)] \tag{3.29}$$

where $\chi_l(\varepsilon)$ is the appropriate trace of the G matrix, l is the final state angular momentum and $\varepsilon = E - E_b$.

4. EXPERIMENTAL DESCRIPTION

This chapter presents the synthesis method and experimental procedures used in the measurements and data analysis of the samples. The samples were analyzed by EDS, TEM, HRTEM, XRD, XPS, time-resolved Mass Spectrometry, *in situ* time-resolved XANES and *in situ* EXAFS techniques.

4.1 Synthesis of the nanoparticles

Cu-CeO_{2-x} nanoparticles were synthesized to obtain improved results for the CO oxidation reaction and to elucidate the atomic phenomena influencing on the reactivity towards CO oxidation reaction. Firstly, the CeO_{2-x} nanoparticles were synthesized in accordance to the procedure described in [34]. Ceric ammonium nitrate ($(NH_4)_2Ce(NO_3)_6$) (2 g) was dissolved in ultra-pure water "type 1" (6 mL). This solution was dropped to a saturated aqueous solution (14 mL) of ammonium carbonate ($(NH_4)_2CO_3$) under magnetic stirring. The pH value of the mixture was maintained at 9 by adding more ammonium carbonate, if needed. After 30 min, the orange yellowish resulting solution was filtered and aliquots (2 mL) were withdrawn and mixed with water or ethanol at different temperatures for 16 h. The CeO_{2-x} nanoparticles (named CeO_{2-x} low TR) were synthesized using 2 mL of water as solvent and a temperature of 30 °C, while the CeO_{2-x} nanoparticles (named CeO_{2-x} high TR) used 2 mL of ethanol and a temperature of 70 °C. Nanoparticles that precipitated after this time period were washed 3 times with water, centrifuged and left in a drying oven at 90 °C for 48 h. A CeO_2 commercial standard (std) (Sigma-Aldrich) was also used for comparison purposes.

The main structural characteristics of the nanoparticles synthesized in this study were already investigated in the previous work [34] by XRD, N_2 adsorption-desorption isotherms, TEM and SEM measurements, which are summarized in Table 4.1. The CeO_{2-x} (high TR) nanoparticles present the highest specific surface area, while the standard presents the lowest one. Also, CeO_{2-x} (high TR) is the smallest nanoparticle while the standard sample is the biggest one. The CeO_{2-x} (low TR) nanoparticles are the only case without a monomodal distribution, presenting three size distributions. Besides

this, the pore size distributions were obtained for the CeO_{2-x} nanoparticles synthesized and the commercial standard (Figure 4.1). It is possible to observe that only the CeO_{2-x} (high TR) nanoparticles present mesoporous with a mean diameter around 3.7 nm. The pore volume obtained from this analysis is shown in Table 4.1.

In the previous work [34], the nanoparticles were exposed to a CO reduction atmosphere and heated to 500 °C. NAP-XPS measurements and *in situ* time-resolved XANES measurements at the Ce L_3 edge were performed during the reduction treatment. These nanoparticles are highly reducible, reaching extremely high Ce(III) fraction values at very low temperatures when compared to the literature results. Table 4.1 also presents the reduction temperature (TR) and the final Ce(III) fraction obtained previously [34] for the nanoparticles synthesized in this work. The reduction temperature was used to label the samples, where the sample CeO_{2-x} (high TR) presents the highest reduction temperature and the CeO_{2-x} (low TR) presents the lowest reduction temperature among the nanoparticles synthesized in the previous work [34]. It is important to notice that the CeO_{2-x} (std) was not reduced in this temperature range, thus it does not presents a reduction temperature value. Another important parameter is the Ce(III) fraction, which is directly related to the O vacancy population. The nanoparticles with the highest initial Ce(III) fraction corresponds to the CeO_{2-x} (low TR), while at 400 °C and 500 °C CeO_{2-x} (high TR) presents the highest values.

Table 4.1: Main electronic and structural characteristics of the synthesized CeO_{2-x} nanoparticles. The uncertainty associated to the specific surface area and pore volume values are 5 m^2g^{-1} and 0.002 cm^3g^{-1}, respectively. The typical uncertainty associated to the Ce(III) fraction values is around 10% of the Ce(III) fraction value. Adapted from [34].

Sample	**Specific Surface Area (m^2/g)**	**Pore Volume (cm^3/g)**	**Mean Diameter (nm)**	**Initial Ce(III) Fraction**	**TR (ºC)**	**Ce(III) Fraction in 500ºC**	**Ce(III) Fraction in 400ºC**
CeO_{2-x} (low TR)	138	0.052	13 ± 3 44 ± 21 90 ± 18	0.26	108	0.75	0.70
CeO_{2-x} (high TR)	201	0.129	3 ± 2	0.13	188	0.90	0.85
CeO_{2-x} (std)	38	0.104	26 ± 24	0.00	--	0	0

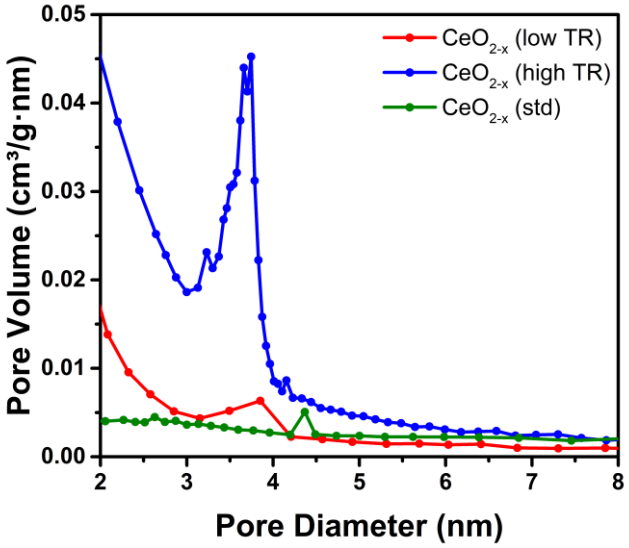

Figure 4.1: Pore size distribution of the CeO_{2-x} (low TR), CeO_{2-x} (high TR) and CeO_{2-x} (std) nanoparticles, obtained from N_2 adsorption-desorption isotherms measurements (adapted from [34]).

The Cu nanoparticles were synthesized in collaboration with Prof. Jairton Dupont (IQ-UFRGS) following the method described in [53]. $CuCl_2 \cdot 2H_2O$ (134 mg, 0.79 mmol) was dissolved in BMI·BF4 ionic liquid (3 mL) and stirred at room temperature for 15 min. After this time, a solution of $NaBH_4$ (296 mg, 7.9 mmol) dissolved in methanol (3 mL) was added to the mixture. The mixture turned black due to the formation of Cu nanoparticles, which were washed 3 times with methanol and 3 times with dichloromethane. The nanoparticles were isolated by centrifugation (3500 rpm) and dried under reduced pressure. These Cu nanoparticles were mixed with the synthesized CeO_{2-x} samples and the CeO_{2-x} commercial standard (50 wt. % of Cu) using an ultrasonic bath, as shown schematically in Figure 4.2.

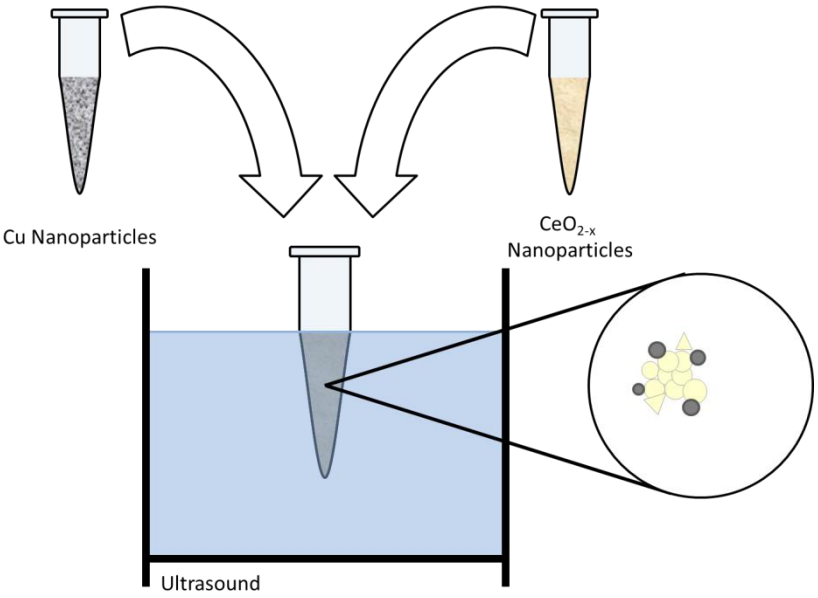

Figure 4.2: Schematic representation of method used for the mixture of the Cu and CeO_{2-x} nanoparticles using an ultrasonic bath.

4.2 EDS Compositional Maps

The EDS compositional maps were performed at Laboratório de Conformação Nanométrica (LCN) at IF-UFRGS using a JEOL JIB4500 Multi-Beam equipment composed of a Focused Ion Beam (FIB) and a Scanning Electron Microscope (SEM) using an operational voltage of 20 kV. For the measurements, the nanoparticle powder - as-prepared and after exposition to the CO oxidation reaction (described below) - was spread out over a carbon tape fixed in an aluminum stub. After this, the stubs were exposed to a carbon deposition in order to avoid charging effects during the measurements. The SEM images were obtained with the backscattered electrons and the EDS compositional maps were obtained with the biggest aperture (3) and a fixed spot size of 50 μm.

4.3 TEM measurements

The TEM images were obtained at the Centro de Microscopia e Microanálise (CMM) at UFRGS using a JEOL JEM 1200 Exll microscope operated with 80 kV. The mixture procedure of the Cu nanoparticles with the CeO_{2-x} nanoparticles should not

modify the Cu size distribution or shape. In order to verify this, the Cu nanoparticles size distribution was obtained for the as-prepared non-supported Cu nanoparticles and as-prepared Cu-CeO_{2-x} (low TR) nanoparticles. For the measurements, the powder was dispersed in deionized water and left in the ultrasound for 15-20 min. Then a drop of this solution was dropped on a TEM Cu grid covered with carbon film. The same procedure was performed for all nanoparticles exposed to the reduction treatment (see description at Section 4.6).

The size distribution histogram of the Cu nanoparticles was obtained analyzing the TEM images by using the ImageJ (Version 6.0) software. The diameter of each nanoparticle was obtained from the mean value between the minimum and maximum Ferret diameter. It was analyzed more than 2000 Cu nanoparticles and the mean diameter was obtained from the average value obtained in the analysis of the non-supported Cu and Cu-CeO_{2-x} (low TR) nanoparticles.

The HRTEM images were obtained at Laboratório Nacional de Nanotecnologia (LNNano) at Centro Nacional de Pesquisa em Energia e Materiais (CNPEM) using a JEOL JEM 2100F microscope operated with 200kV. The samples were prepared as described above, but now using a Ni grid. EDS Line Scan measurements were also conducted and, in this case, it was used the Scanning TEM (STEM) mode with the sample tilted by 15º in order to increase the signal to noise ratio in the EDS Si detector. The EDS measurements were performed using a fixed spot size of 1 nm. The images were analyzed using the Gatan Digital Micrograph software (Version 3.22.1461.0).

4.4 XRD measurements

The XRD measurements were performed at IF-UFRGS in a Siemens D500 conventional diffractometer using a Cu Kα (1.5406 Å) radiation, working at 40 kV and 17.5 mA. For the XRD measurements, the as-prepared Cu-CeO_{2-x} nanoparticles were fixed in a glass blade. The data were collected for a 2θ range between 20° and 80°, using a scanning step of 0.05° during 1 s/point.

The pattern indexing was performed using reference standards obtained from the ICSD database [82]. The Rietveld refinement was employed using the FullProf [83]

software (version July-2017). The instrumental resolution function (IRF) was obtained from a LaB_6 standard. Rietveld refinements were carried out using the pseudo-Voigt profile function of Thompson, Cox and Hastings [84] and a linear background. During the refinement, the Debye-Waller overall factor and the atom occupancy were fixed from the cif file obtained in the literature.

4.5 XPS measurements

The XPS data were obtained at LNNano-CNPEM with a Thermo Scientific K-Alpha X-ray photoelectron spectrometer using an Al Kα (1486.6 eV) radiation and a voltage in the X-ray tube of 12 kV. For the XPS measurements, the powder of the nanoparticles was spread out in a carbon tape fixed in a steel sample holder. Then, the samples were inserted in the high vacuum chamber ($p \sim 1x10^{-8}$ mbar). The angle between the incoming beam direction and the analyzer was set at 45°. The photoelectrons were collected by a 180° double focusing hemispherical analyzer (HSA), operating in the CAE mode and detected by a 128-channels detector. During the measurements, the charging of the samples was compensated by the use of a flood gun, which provides a low-energy electron flow in the sample. The measurements were performed in the Survey, Cu 2p, Ce 3d, Cu 3p, Ce 4d, C 1s and O 1s regions. The pass energy used was 200 eV and 50 eV for the Survey and high resolution measurements, respectively. An energy step size of 1 eV and 0.1 eV was used for the Survey and high resolution measurements, respectively.

The XPS data were analyzed using the XPSPeak (Version 4.1) software. For the high resolution spectra, a Shirley-type background was used. The measurements were calibrated due to charging effects using the Ce 3d peak position at 882.3 eV. An asymmetric Gaussian-Lorentzian function with 55% Lorentzian contribution was used to fit the chemical components at the Cu $2p_{3/2}$ region, as determined from the analysis of an Au standard sample [55]. The FWHM values were fixed for a given chemical component obtained in different samples.

The Ce 3d XPS region is complex and a different analysis was used to fit this region. The fitting procedure was performed based in the method described in the literature [85]. Initially, the CeO_2 standard sample was adjusted using 10 components.

Following notation given by Burroughs et al. [86], the v_o, u_o, *v'* and *u'* components correspond to the $3d_{5/2}$ and $3d_{3/2}$ doubles of the Ce(III) component, hence the area constraint was used in these components. An asymmetric Gaussian-Lorentzian function with 37% Lorentzian contribution was used to fit the Ce 3d region as obtained by fitting the *u'''* single peak. The energy differences and FWHM values of the components for each sample were constrained to the values obtained from the CeO_2 standard analysis. The surface Ce(III) fraction was obtained from the intensity of each component by:

$$Ce(III)_{surf} = \frac{v_0 + v' + u_0 + u'}{v_0 + v + v' + v'' + v''' + u_0 + u + u' + u'' + u'''} \qquad (4.1)$$

4.6 Time-resolved Mass Spectrometry measurements

The time-resolved Mass Spectrometry measurements were carry out at the Brazilian Synchrotron Light Laboratory (LNLS) at CNPEM during the time-resolved *in situ* XANES measurements at the Cu K edge at the DXAS beamline. For the measurements, pellets of 15 mg of nanoparticles (Cu-CeO_{2-x}) and 35 mg of BN were used. The samples were fixed in the sample holder and inserted in a tubular furnace. The mass spectrometer was fixed after the pellet, then ensuring that all gas molecules arriving in the mass spectrometer diffused throw the pellet. Figure 4.3 shows schematically the thermal treatment applied to the samples, that were initially exposed to 100 ml/min 5% CO + 95% He at room temperature. Then, the samples were heated to 400 °C with a heating rate of 10 °C/min, then remaining for 30 min at this temperature. This thermal treatment was performed in order to reduce the nanoparticles, then increasing the O vacancy population in the CeO_{2-x} nanoparticles [34]. The samples remained for 30 min at 400 °C aiming to reach the oxidation state of equilibrium at this temperature, which is essential for the in situ measurements. After this, the samples were cooled to 250 °C exposed to the same atmosphere. At 250 °C, 50 ml/min 5% O_2 + 95% He was inserted, then starting the CO oxidation reaction. The samples remained for 30 min at 250 °C under the CO + ½ O_2 atmosphere. After this time period, the O_2 flux was removed and the samples were heated again to 400 °C with a heating rate of 10 °C/min under 100 ml/min 5% CO + 95% He. After 30 min at 400 °C, the samples were

cooled to 150 °C and exposed to the CO oxidation reaction again (insertion of 50 ml/min 5% O_2 + 95% He), then remaining exposed to these conditions for 30 minutes. At the end, the samples were cooled to room temperature with 100 ml/min N_2.

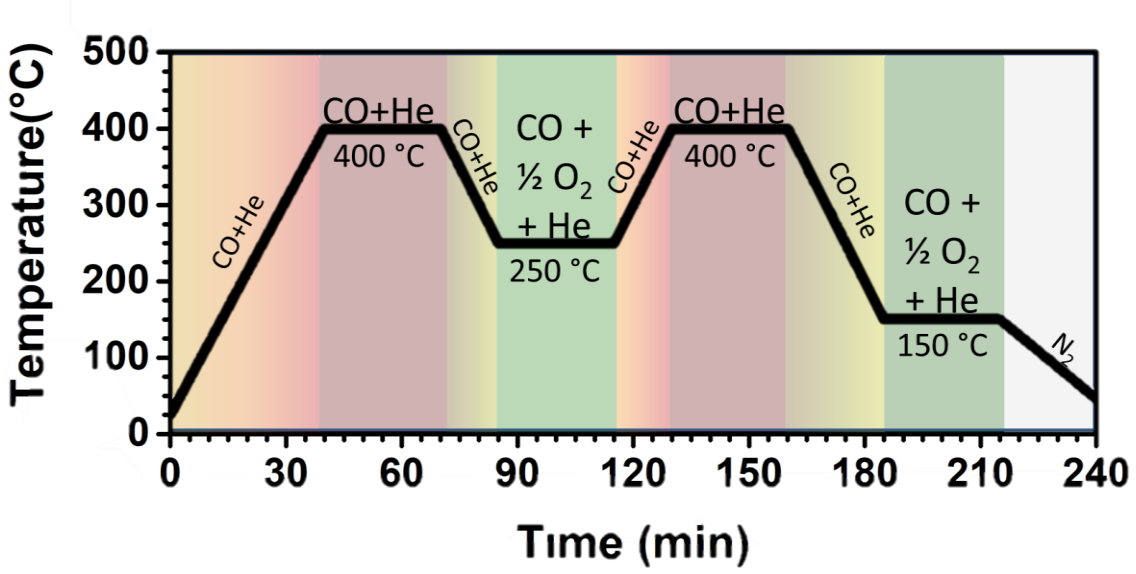

Figure 4.3: Schematic representation of the sequential thermal treatment applied to the Cu-CeO_{2-x} nanoparticles.

The Mass Spectrometry measurements were performed during the full sequential treatment applied using a Pfeiffer Vaccum OminiStar mass spectrometer coupled to the tubular furnace where the sample was inserted.

4.7 *In situ* time-resolved XANES measurements

The *in situ* time-resolved XANES measurements were carried out at the DXAS beamline [77] at LNLS. In the DXAS beamline, the beam comes from the bending magnet and it is focused by a Rh-coated mirror onto the Si (111) curved monochromator that produces a polychromatic beam. The measurements were performed in transmission mode with the sample positioned in the focal point of the monochromator and the signal was detected using a position sensitive CCD detector.

For the measurements, pellets made of a mixture of Cu-CeO_{2-x} nanoparticles and BN were produced and inserted in the tubular furnace. The XANES spectra were acquired at the Cu K edge (8979 eV) using 15 mg of nanoparticles and 35 mg of BN.

On the other hand, for the measurements at the Ce L_3 edge (5723 eV) a mixture of 10 mg of nanoparticles and 40 mg of BN was used. For the Cu K and Ce L_3 edge, a spectrum was acquired every 1 min and 15 s, respectively. The time resolution of the measurements is 100 ms. The measurements were performed during the full thermal treatment applied, schematically represented in Figure 4.3. Besides the synthesized nanoparticles, some standard samples were measured for the XANES analysis. At the Cu K edge, the Cu(0), Cu_2O, CuO, $Cu(OH)_2$ and Cu-Cl standards were measured at room temperature. At the Ce L_3 edge, the CeO_2 and $Ce(OH)CO_3$ standards, related to the Ce(III) and Ce(IV) oxidation states respectively, were measured at room temperature.

Initially, the XANES spectra at the Ce L_3 and Cu K edges were analyzed in accordance to the standard procedure of data reduction [79] using IFEFFIT [87]. It was analyzed the *in situ* XANES spectra every 5 minutes of the thermal treatment applied. The analysis of the Ce L_3 edge XANES spectra was performed by fitting a set of Lorentzian and arctangents functions as described in the literature [88]. Firstly, the XANES spectrum of the Ce(III) standard was performed using one Lorentzian function, related to the electron transition from $2p_{3/2} \rightarrow (4f^1)5d$ electronic level and one arctangent function related to the electron transition to the continuum. The fit of the Ce(IV) standard spectrum was performed with two Lorentzian functions, related to the electron transitions $2p_{3/2} \rightarrow (4f^{\Gamma})5d$ and $2p_{3/2} \rightarrow (4f^0)5d$, where Γ denotes an electron in the O 2p orbital transferred to the Ce 4f orbital, and an arctangent function with the same parameters used in the fitting of the Ce(III) standard. In this way, it was possible to obtain the concavity (B) and energy position (C) of the arctangent function and the width (E) and energy positions (F) of the Lorentzian functions related to the Ce(III) and Ce(IV) components. These parameters were initially fixed in the fit of the time-resolved XANES spectra of the nanoparticles, which were performed using one arctangent and three Lorentzian functions, as described in Equation (4.2):

$$f(x) = \pi \cdot \frac{A}{2} + A \cdot arctg[B \cdot (x - C)] + \frac{D_{III} \cdot E_{III}^2}{(x - F_{III})^2 + E_{III}^2} + \frac{D'_{IV} \cdot E'^2_{IV}}{(x - F'_{IV})^2 + E'^2_{IV}} + \frac{D''_{IV} \cdot E''^2_{IV}}{(x - F''_{IV})^2 + E''^2_{IV}} \quad (4.2)$$

where A is the arctangent's amplitude, D is the Lorentzian functions height and the subscripts refers to the Ce oxidation state. The energy range used in the fitting was chosen in order to contain the three Lorentzian functions and maintained around 20 eV for all the spectra. The energy position of the Lorentzian function was varied 0.5 eV around the value obtained from the fit of the standards, but the value was fixed for all spectra related to the same nanoparticles.

The oxidation state of the cerium oxide nanoparticles was obtained using the area of the Lorentzian function related to the Ce(III), normalized by the total area of the Lorentzian functions used in the fit, as shown in the equation:

$$\%\, Ce(III) = \frac{D_{III} \cdot E_{III}}{D_{III} \cdot E_{III} + D'_{IV} \cdot E'_{IV} + D''_{IV} \cdot E''_{IV}} \times 100\ \% \qquad (4.3)$$

where D and E are the height and FWHM of the Lorentzian functions, respectively, related to the Ce(III) and Ce(IV) components. This analysis allowed obtaining the oxidation state of the cerium oxide nanoparticles as a function of time, temperature and atmosphere.

The analysis of the *in situ* time-resolved XANES spectra at the Cu K edge was performed using the LCA in the energy range between -20 eV and +50 eV around the absorption edge. The fit was performed using the Cu standard spectra measured. For the fitting procedure, the weight of each component was constrained to positive values and the sum of all contributions was set equal to 1.0. In this way, it was possible to obtain the components present in the Cu nanoparticles as a function of time, atmosphere and temperature used. The time-resolved EXAFS signal χ(k) was extracted and then Fourier transformed using a k^2-weighted χ(k) and a Kaiser-Bessel window, with a k range of 6.0 $Å^{-1}$.

4.8 *In situ* EXAFS measurements

The EXAFS measurements were performed at the XAFS2 [89] beamline at LNLS. In this beamline, the radiation emitted by a bending magnet is firstly collimated

vertically by a Rh-coated cylindrical mirror, then beam is monochromatized by a Si(111) double crystal monochromator and focused in the sample by a second Rh-coated mirror. The measurements were performed at the Cu K edge (8979 eV) in transmission mode using three ionization chamber filled with a mixture of He, N_2 and Ar. One ionization chamber was positioned before the sample in order to measure the intensity of the incident beam, the second one was positioned after the sample and the last one was positioned after a Cu(0) standard foil. Pellets were produced by mixing 15 mg of the Cu-CeO_{2-x} nanoparticles with 35 mg of BN. The samples were exposed to the sequential thermal treatment shown in Figure 4.3 but without the second reduction treatment at 400 °C and without the CO oxidation reaction at 150 °C. The EXAFS measurements were performed at 250 °C under CO atmosphere and CO + ½ O_2 atmosphere. The measurements were performed with a 5.0 eV, 0.3 eV and 2.0 eV energy step and 1.0 s, 2.0 s and 3.0 s/point at the pre-edge (8920 eV – 8970 eV), XANES (8970 eV – 9030 eV) and EXAFS (9030 eV – 9624 eV) regions, respectively.

The EXAFS spectra were analyzed in accordance with the standard procedure of data reduction [79] using IFEFFIT [87]. The EXAFS signal $\chi(k)$ was extracted and then Fourier transformed using a k^2-weighted $\chi(k)$ and a Kaiser-Bessel window, with a k range of 8.0 $Å^{-1}$. The phase shift and amplitudes were obtained with the FEFF8 code by using a *fcc* metallic Cu, *fcc* Cu_2O and a monoclinic CuO cluster with 6 Å radius each. For the fit of the EXAFS oscillations, the amplitude reduction factor (S_0^2) was fixed at 0.85, as obtained from the Cu(0) standard fit. The R-factor obtained from the analysis was always lower than 0.02, which demonstrates the excellent agreement between the proposed model and the experimental result.

5. RESULTS AND DISCUSSION

This chapter is dedicated to present the results obtained from the TEM, EDS, XRD, XPS, Mass Spectrometry and *in situ* XAS measurements of the synthesized nanoparticles and the corresponding interpretation of the data obtained.

5.1 Characterization of the as-prepared nanoparticles

5.1.1 TEM measurements

The TEM measurements of the CeO_{2-x} synthesized nanoparticles and the nanoparticle commercial standard were performed and analyzed in a previous study [34]; and the size distribution results are displayed in Table 4.1. The Cu nanoparticles were mixed with CeO_{2-x} nanoparticles using an ultrasonic bath. This procedure should not change the size or the morphology of the Cu nanoparticles. In order to confirm that, TEM measurements were performed for the non-supported Cu and Cu-CeO_{2-x} (low TR) nanoparticles. Figure 5.1(a) and (c) present typical TEM images of the non-supported Cu and Cu-CeO_{2-x} (low TR) nanoparticles, respectively, where it is observed that the Cu nanoparticles present a spherical shape. The size distribution histograms of the Cu nanoparticles from the non-supported Cu and Cu-CeO_{2-x} (low TR) nanoparticles are presented in Figure 5.1(b) and (d), respectively, with a mean diameter around 8 nm in both cases. Thus, it can be observed that the mixing procedure applied does not change the size or the shape of the Cu nanoparticles, as expected.

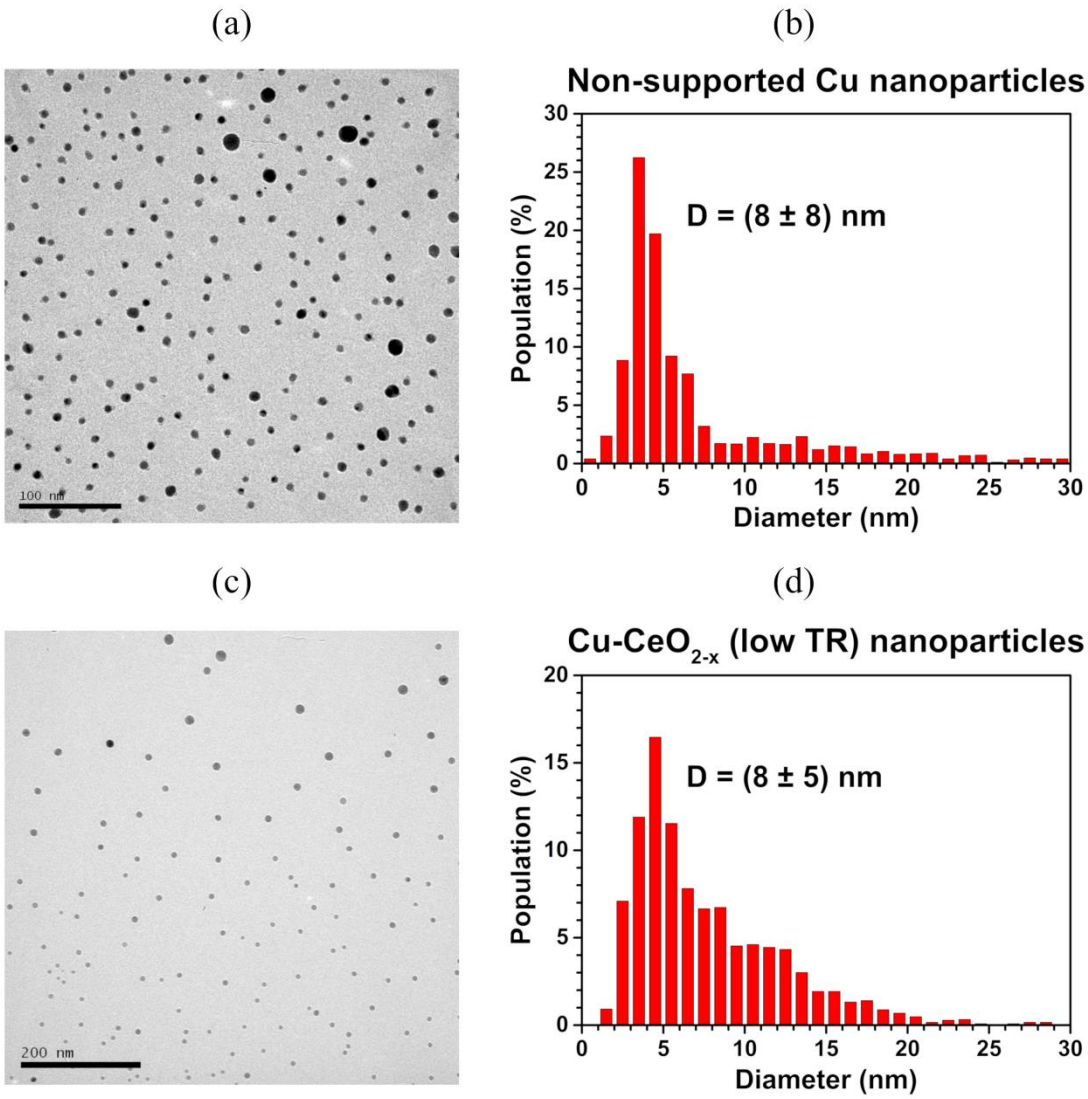

Figure 5.1 TEM image (on the left) and the corresponding size distribution histogram (on the right) of the Cu nanoparticles from the non-supported Cu ((a) and (b)) and Cu-CeO_{2-x} (low TR) ((c) and (d)) nanoparticles.

Figure 5.1(c) presents a TEM image of a sample region where the Cu nanoparticles are not mixed with CeO_{2-x} nanoparticles. These nanoparticles could have been separated from the CeO_{2-x} due to the method used to prepare the samples for the TEM measurements, in which the sample was dissolved in deionized water and placed in the ultrasonic bath for around 15 to 20 min. It was already observed in the literature for similar systems [90, 91]. However, during the TEM measurements, it was possible to observe regions where the Cu nanoparticles were supported on larger agglomerates of CeO_{2-x} nanoparticles, as presented in Figure 5.2 for the Cu-CeO_{2-x} (high TR) nanoparticles.

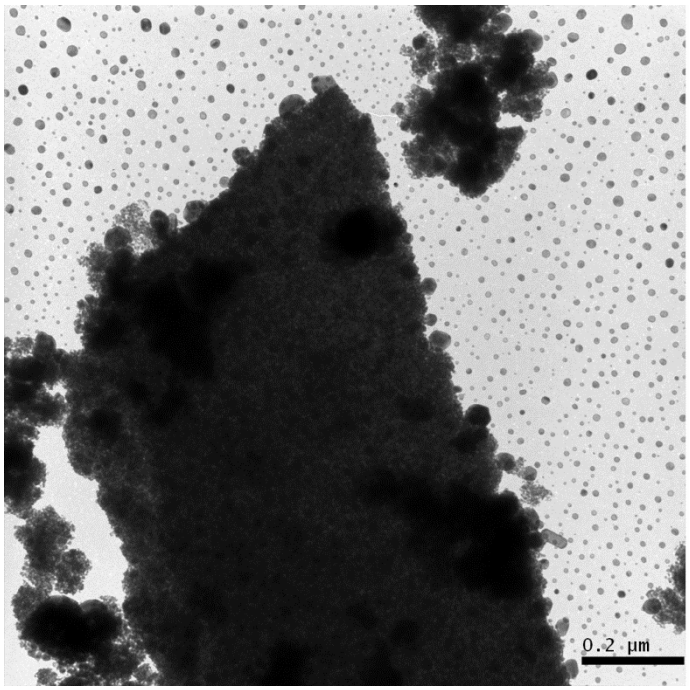

Figure 5.2: TEM image of the Cu nanoparticles supported on a CeO_{2-x} agglomerate for the Cu-CeO_{2-x} (high TR) nanoparticles.

In order to obtain the concentration of each element and to observe whether the samples were homogeneous, EDS measurements were analyzed.

5.1.2 EDS Compositional Maps

The EDS measurements allowed the analysis of the chemical elements distribution in the samples and the fraction of each element. Figure 5.3 presents the EDS compositional maps for Ce and Cu atoms, measured in the same sample region in the SEM mode, for all nanoparticles. It is possible to notice that the Cu and Ce signals occupy the same areas and are spread over the entire map obtained, indicating that the Cu and CeO_{2-x} nanoparticles are in the same region. Moreover, all samples present Na and Cl in their composition. It comes from the synthesis procedure of the Cu nanoparticles. The Al signal observed in the spectra comes from the stub where the samples were fixed.

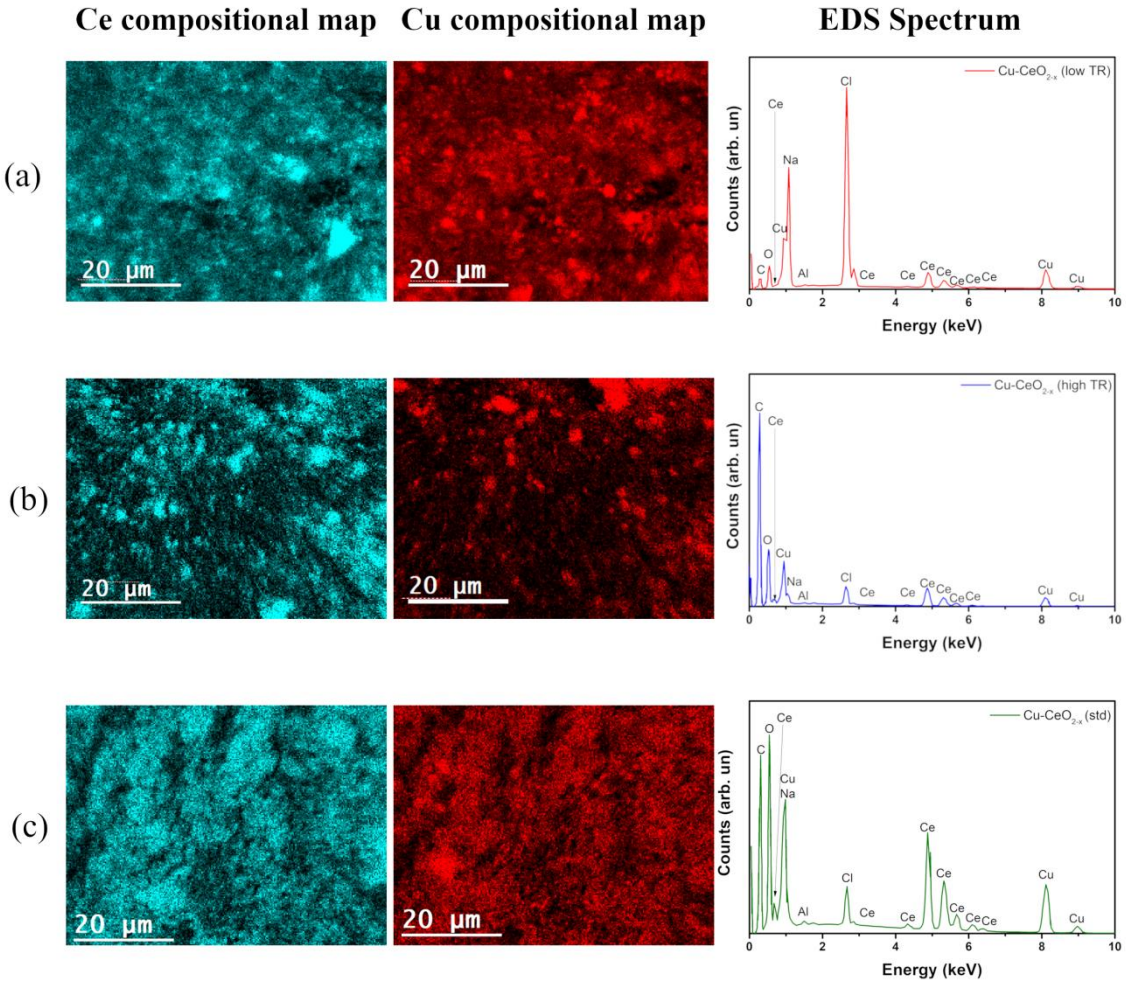

Figure 5.3: Ce (on the left) and Cu (middle) compositional maps and a typical EDS spectrum (on the right) for the (a) Cu-CeO_{2-x} (low TR); (b) Cu-CeO_{2-x} (high TR) and (c) Cu-CeO_{2-x} (std) nanoparticles.

The analysis of the EDS spectrum allowed obtaining the fraction of the chemical compounds, CuO and NaCl, which are identified in the XRD analysis described in the Section 5.1.3. The weight percent fraction of each compound was calculated considering that all the Cu atoms were related to the CuO compound, the Ce atoms were related to the CeO_2, and the Na atoms were related to the NaCl, since these were the only components found in the XRD patterns. Table 5.1 shows the weight fraction of each compound where it is possible to observe that all nanoparticles present similar wt.% values of CuO. However, the Cu-CeO_{2-x} (low TR) nanoparticles present the highest amount of NaCl, while the Cu-CeO_{2-x} (std) present the lowest one. The NaCl fraction in each sample will influence on the sample's reactivity since it is included in the mass of the sample used, meaning that the mass of Cu-CeO_{2-x} nanoparticles is lower than the measured one and it varies between the samples.

Table 5.1: Weight percent value of the CuO and NaCl compounds present in the samples. The estimated error for this analysis is 20% of the value obtained.

Sample	Fraction (wt. %)	
	$\frac{CuO}{CuO + CeO_2}$	$\frac{NaCl}{NaCl + CuO + CeO_2}$
Cu-CeO_{2-x} (low TR)	58	62
Cu-CeO_{2-x} (high TR)	37	13
Cu-CeO_{2-x} (std)	40	06

5.1.3 XRD measurements

Figure 5.4 presents the diffractograms of the as-prepared samples, the indexing with the crystalline phases and the Rietveld refinement obtained. All nanoparticles presented the CuO, NaCl and CeO_{2-x} crystalline phases.

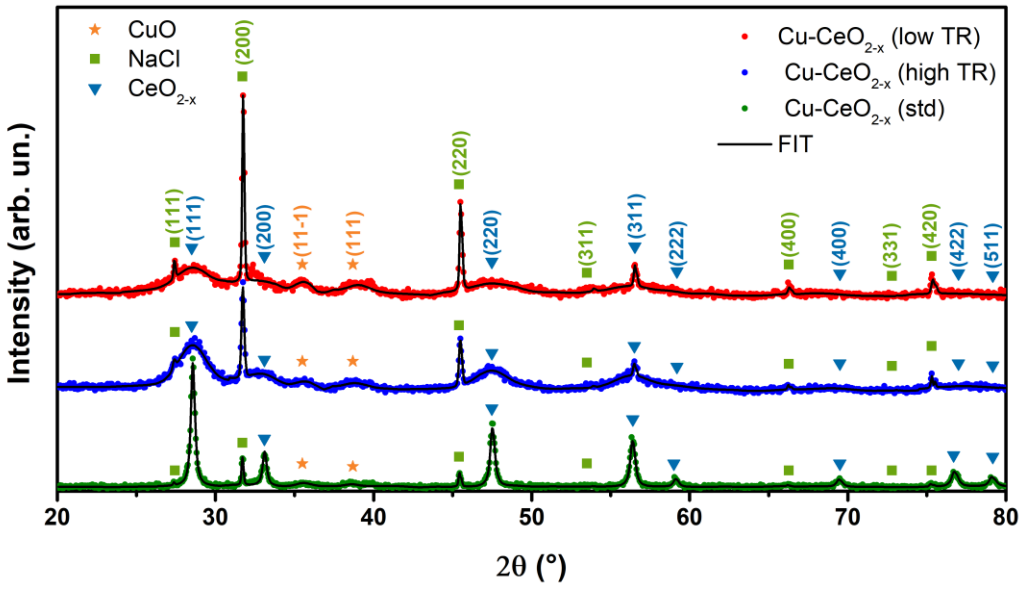

Figure 5.4: XRD diffractograms and the respective Rietveld refinement, presented as a solid black line, obtained for the Cu-CeO_{2-x} (low TR) (red), Cu-CeO_{2-x} (high TR) (blue) and Cu-CeO_{2-x} (std) (green) nanoparticles.

The CeO_{2-x} phase (ICSD 237959) presents the fluorite crystalline structure that is characterized as a cubic unit cell. The Cu nanoparticles have a CuO (ICSD 67850) crystalline phase, which have a monoclinic crystalline structure. As stated before, the NaCl, present in all samples, comes from the synthesis procedure of the Cu nanoparticles.

Figure 5.4 shows that the synthesized Cu-CeO_{2-x} nanoparticles present the CeO_{2-x} Bragg's reflections with FWHM values larger than those of the Cu-CeO_{2-x} (std) nanoparticles. It may occur due to a smaller crystallite size or the presence of defects in the crystalline lattice of the synthesized nanoparticles. Table 5.2 presents a comparison between the crystallite size obtained from the Rietveld refinement and the size of the nanoparticles obtained by TEM measurements. The Cu-CeO_{2-x} (high TR) and Cu-CeO_{2-x} (low TR) nanoparticles present a crystallite size for the CuO phase smaller than the mean size obtained from the TEM measurements. It may be related to the structural disorder of the CuO nanoparticles that widens the Bragg's reflections. The CeO_{2-x} phase in the Cu-CeO_{2-x} (low TR) nanoparticles presents a crystalline size much smaller than the size obtained by TEM, which indicates the agglomeration of CeO_{2-x} (low TR) nanoparticles in the TEM images. The Cu-CeO_{2-x} (std) presents a crystallite size for the Cu and CeO_{2-x} nanoparticles very similar to those obtained from the TEM measurements, which also happens for the CeO_{2-x} crystalline phase in the Cu-CeO_{2-x} (high TR) nanoparticles.

Table 5.2: Comparison between the mean diameter obtained by TEM and the crystallite size obtained by XRD analysis. The typical uncertainty associated to the XRD analysis is around 5% of the values obtained.

Sample	**Mean Diameter (nm)**			
	CuO		**CeO_{2-x}**	
	TEM	**XRD**	**TEM**	**XRD**
Cu-CeO_{2-x} (low TR)	8 ± 5	6.0	13 ± 3 44 ± 21 90 ± 18	4.2
Cu-CeO_{2-x} (high TR)	8 ± 5	5.4	3 ± 2	4.5
Cu-CeO_{2-x} (std)	8 ± 5	8.0	26 ± 24	26.5

Table 5.3 presents the lattice parameter and the Ce(III) fraction of the CeO_{2-x} crystalline phase. The lattice parameter (a) of the CeO_{2-x} crystalline phase was obtained from the Rietveld refinement. By comparing the lattice parameter obtained for all nanoparticles and the lattice parameter of a CeO_2 standard obtained from the literature (5.407 Å), it is possible to notice that all nanoparticles present an expansion of the unit cell that is higher for the Cu-CeO_{2-x} (low TR) and lower for the Cu-CeO_{2-x} (std)

nanoparticles. This lattice expansion in oxides is usually related to the nanoparticle's size, where smaller nanoparticles would present a higher lattice expansion [92]. However, this cannot explain the results presented in Table 5.3, once Cu-CeO_{2-x} (high TR) presents the smaller mean diameter among the CeO_{2-x} nanoparticles. Thus this expansion in the lattice parameter of the CeO_{2-x} unit cell is directly related to the Ce(III) fraction present in the sample, which means that a higher lattice parameter is related to a higher O vacancy population [93]. This Ce(III) fraction can be calculated using the Kim's equation [93]:

$$a = (0.5407 + 200x \times 2.740 \cdot 10^{-4})\ \text{nm} \qquad (5.1)$$

where 0.5407 is the lattice parameter for the CeO_2 standard obtained from the literature (in nm), 2.74×10^{-4} is the Vegard parameter and x is related to the O vacancy population according to CeO_{2-x}. The Ce(III) fractions, obtained using Equation (5.1), are reported in Table 5.3. It is possible to observe that the Cu-CeO_{2-x} (low TR) nanoparticles present the highest Ce(III) fraction, while the Cu-CeO_{2-x} (std) presents the lowest one, following the same trend obtained in the previous study [34] (see Table 4.1). Although, the synthesized Cu-CeO_{2-x} nanoparticles present a lower Ce(III) fraction, which might be due to the interaction between the Cu and CeO_{2-x} nanoparticles or due to the aging of the samples used previously since these samples were exposed to the atmosphere for a longer period before the measurements. The exposition to the atmosphere changes the oxidation state of the CeO_{2-x} nanoparticles, as demonstrated in [34], however it should not change the Ce(III) fraction of the nanoparticles during the reduction treatment under CO atmosphere or during the CO oxidation reaction.

Table 5.3: Lattice parameter (a) of the CeO_{2-x} crystalline phase obtained from the Rietveld refinement and Ce(III) fraction obtained by XRD analysis. The estimated error for the Ce(III) fraction is around 5 % of the obtained values.

Sample	a (Å)	a expansion (%)	Ce(III) fraction
Cu-CeO_{2-x} (low TR)	5.423	0.29	0.058
Cu-CeO_{2-x} (high TR)	5.416	0.18	0.035
Cu-CeO_{2-x} (std)	5.411	0.08	0.015

The as-prepared Cu-CeO_{2-x} nanoparticles were studied using the XPS technique in order to determine the oxidation state and the chemical components present at the

surface.

5.1.4 XPS measurements

In order to identify possible contaminants in the nanoparticles, the long scan XPS spectra were obtained and are displayed in Figure 5.5, where the elements are identified. It is possible to observe that all nanoparticles present the same chemical elements. These elements are in accordance to the EDS and XRD analysis. Besides Cu, Ce, O and C, the nanoparticles present Na and Cl, as observed in the XRD and EDS measurements.

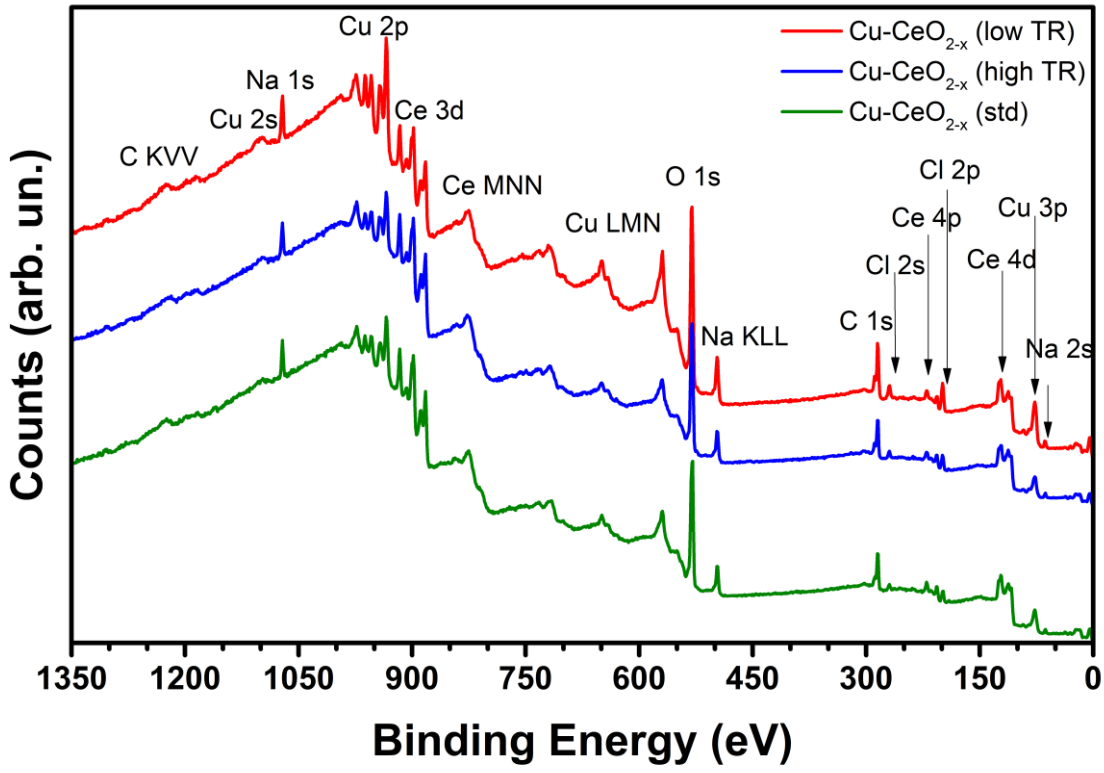

Figure 5.5: XPS long scan spectra of the as-prepared Cu-CeO_{2-x} (low TR), Cu-CeO_{2-x} (high TR) and Cu-CeO_{2-x} (std) nanoparticles, measured using Al Kα X-ray source (hν = 1486.7 eV).

Figure 5.6 presents the XPS spectra for the Ce 3d region. The peak labeling follows the Burrough's notation [86]. In this case, the inelastic mean free path of photoelectrons coming from the Ce 3d electronic level is $\lambda_{IMFP} \approx 11$Å [94], showing the surface sensitivity of the analysis performed. The relative intensity of the *u'''* peak with a binding energy of around 916 eV is directly related to the Ce(IV) fraction in the

nanoparticles. The nanoparticles present a similar relative intensity of this peak, showing a similar oxidation state of Ce atoms at the surface of the CeO_{2-x} nanoparticles. In order to quantify the Ce(III) fraction, the Ce 3d region was fitted following procedure described in Section 4.5. The peaks presented in dark and light grey are related to the Ce(IV) and Ce(III) components, respectively. The area of these peaks were used to calculate the Ce(III) fraction by Equation (4.1).

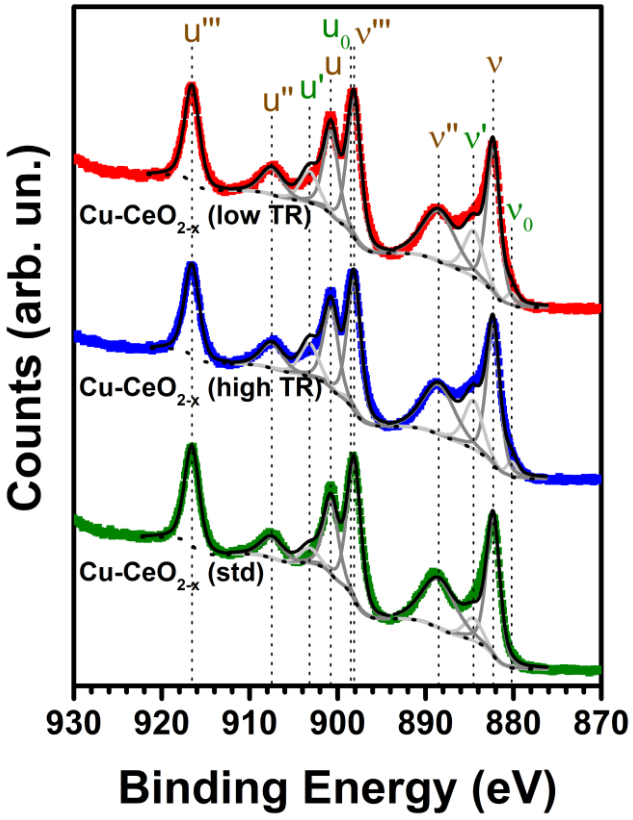

Figure 5.6: Ce 3d XPS spectra for the as-prepared Cu-CeO_{2-x} nanoparticles. The black points represent the Shirley background used, the black solid line total the fit performed using the dark gray (corresponding to Ce(IV) component) and light gray (representing the Ce(III) component) peaks.

The Ce(III) fraction, obtained from the Ce 3d XPS analysis, is presented in Table 5.4, where it is possible to notice that the sample's surfaces of all nanoparticles are highly oxidized. The Cu-CeO_{2-x} (std) presents the lowest Ce(III) fraction, as expected by the results obtained from the XRD analysis. The Cu-CeO_{2-x} (low TR) nanoparticles present the same Ce(III) fraction (considering the uncertainty) than the Cu-CeO_{2-x} (high TR) nanoparticles. In all cases, the Ce(III) fraction at the surface (Table 5.4) is higher than the values obtained for the full nanoparticle (Table 5.3), as expected

since the creation of O vacancies starts at the surface of the materials [34].

Table 5.4: Ce(III) fraction at the surface of the as-prepared nanoparticles obtained from the Ce 3d XPS spectra. The typical uncertainty associated to the analysis is around 10% of the values obtained.

Sample	% Ce(III)
Cu-CeO_{2-x} (low TR)	16
Cu-CeO_{2-x} (high TR)	18
Cu-CeO_{2-x} (std)	8

The Cu $2p_{3/2}$ XPS spectra of the as-prepared Cu-CeO_{2-x} nanoparticles are presented in Figure 5.7 with the respective fitting performed. In this case, the inelastic mean free path associated to the photoelectrons coming from the Cu $2p_{3/2}$ is $\lambda_{IMFP} \approx 12$ Å [94]. It is possible to notice that the nanoparticles present two chemical components, the Cu(I) at around 932.1 eV that is related to the Cu-Cl bonding [95], and the Cu(II) that may be related to different compounds. The literature presents the binding energy for the Cu(II) component in the Cu $2p_{3/2}$ region of 933.4 eV for the CuO [96] and 933.8 eV for the $Cu(OH)_2$ compounds [97]. Due to the wide peaks associated for these two compounds and the small difference in the binding energy, it is hard to distinguish them in this case. In principle, it would be possible to have a mixture of both compounds also. Then, the component will be labeled generically as Cu-O in this case. These chemical components are in accordance to the previous work from the group [54], where the as-prepared non-supported Cu nanoparticles were analyzed by XPS, presenting Cu-Cl and Cu-O bonding [54]. The quantitative composition of the Cu nanoparticles was obtained using the area of the peaks related to each chemical component and it is presented in Table 5.5.

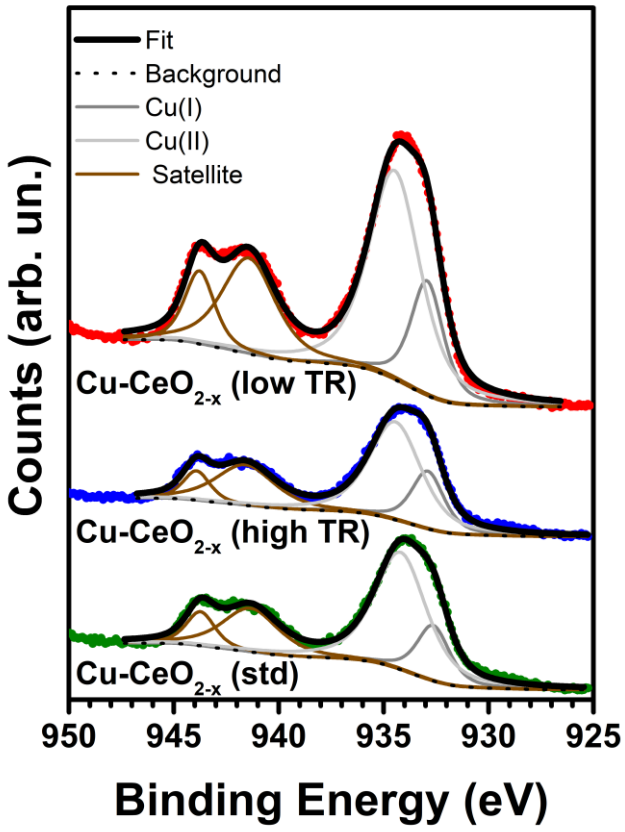

Figure 5.7: Cu $2p_{3/2}$ XPS spectra of the as-prepared Cu-CeO_{2-x} (low TR), Cu-CeO_2-x (high TR) and Cu-CeO_2-x (std) nanoparticles. The black points represent the Shirley background, the black solid line the fit obtained, the dark gray solid line the Cu(I) component, the light gray solid line the Cu(II) component and the brown solid line the Cu $2p_{3/2}$ satellites.

Table 5.5: Percentage of the chemical components used in the fitting of the Cu $2p_{3/2}$ XPS region for the as-prepared Cu-CeO_{2-x} nanoparticles.

Sample	% Cu(I)	% Cu(II)
Cu-CeO_{2-x} (low TR)	26	74
Cu-CeO_{2-x} (high TR)	27	73
Cu-CeO_{2-x} (std)	23	77

The nanoparticles present a higher fraction of the Cu(II) component at the surface, then consistent with the oxidation of the surface of the Cu nanoparticles due to the exposure to the atmosphere. Also, it is observed in Table 5.5 that all nanoparticles present a similar Cu(I) and Cu(II) fraction values. These values represent the chemical components at the surface region of the nanoparticles ($\lambda_{IMFP} \approx 12$ Å). In order to probe a deeper region of the nanoparticles (full nanoparticle) regarding the chemical components, XANES measurements at the Cu K edge were performed.

5.1.5 XANES measurements

The XANES spectra of the as-prepared nanoparticles, measured at the Cu K edge, are presented in Figure 5.8. It was measured also a CuO, $Cu(OH)_2$, Cu-Cl, Cu_2O and Cu(0) standards for comparison purposes. It is possible to notice that the XANES spectra of all nanoparticles are more similar to the CuO standard spectrum than any other Cu standard spectrum. It indicates that the CuO is the compound with the highest fraction in all cases.

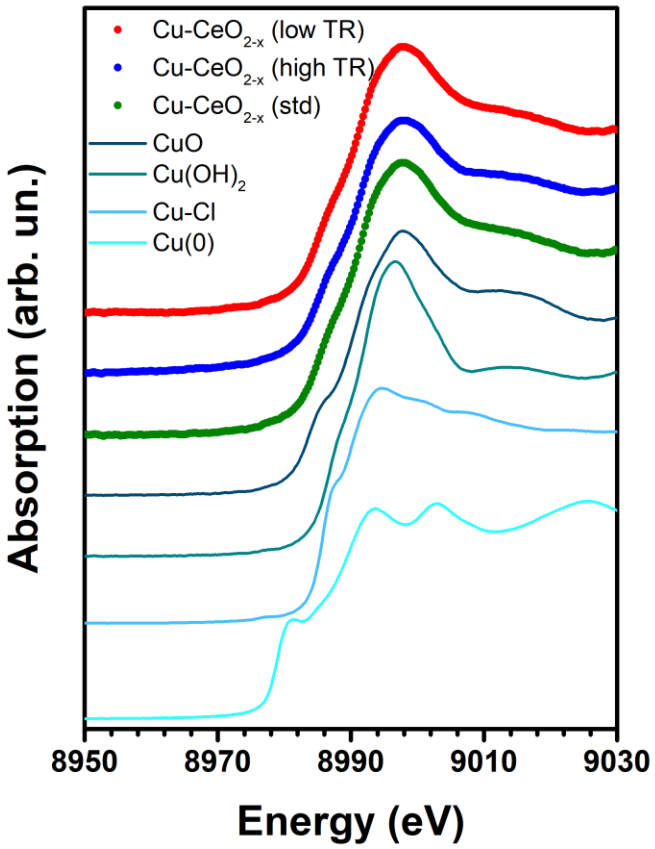

Figure 5.8: XANES spectra measured at the Cu K edge for the as-prepared nanoparticles and Cu standards (CuO, $Cu(OH)_2$, Cu-Cl and Cu(0)).

The XANES spectra of the nanoparticles were analyzed with the linear combination method using the different Cu standards measured. The result of this analysis is presented in Table 5.6.

Table 5.6: Percentage of the chemical components of the as-prepared Cu-CeO_{2-x} nanoparticles obtained from the XANES measurements at the Cu K edge. The typical uncertainty associated to the XANES results is around 10% of the value obtained.

Samples	Cu(0)	CuO	$Cu(OH)_2$	Cu-Cl
Cu-CeO_{2-x} (low TR)	1%	79%	14%	6%
Cu-CeO_{2-x} (high TR)	10%	69%	11%	10%
Cu-CeO_{2-x} (std)	0%	78%	19%	3%

It is observed that the nanoparticles present around 70% - 80% of CuO, being the compound with the highest fraction in the nanoparticles, as expected from the XRD analysis, which presented only the CuO crystalline phase. The nanoparticles also contain the $Cu(OH)_2$ compound but with fractions smaller than 20%. The $Cu(OH)_2$ and CuO compounds come from the exposition of the nanoparticles to the atmosphere. These components represent the Cu(II) chemical component observed in the XPS spectra and accounts for around 90% of the nanoparticles composition. The Cu-Cl component is a residue of the precursor used in the synthesis of the Cu nanoparticles and it is consistent with the Cu(I) chemical component found in the XPS analysis since it was associated to the Cu-Cl bonding. The $Cu(OH)_2$ and Cu-Cl components do not appear in the XRD measurements because the CuO Bragg's reflections have a small relative intensity, compared to the CeO_2 and NaCl crystalline phases, and a small amount of the $Cu(OH)_2$ and Cu-Cl compounds is found in the nanoparticles, then becoming hard to detect them in the XRD measurements. Also, the presence of these compounds may explain the differences observed in the crystalline mean sizes of the Cu nanoparticles, which were smaller than the values obtained by TEM, since only the CuO crystalline phase was taken into account for determination of the crystalline mean size. The Cu(0) component presents a negligible amount in the nanoparticles. It is again consistent with the XRD and XPS results since no Cu(0) crystalline phase is observed in the XRD pattern, neither a Cu(0) chemical component is found in the XPS measurements because the small amount of Cu(0) is expected at the core of the nanoparticles, which is not probed by the XPS analysis. Moreover, the compounds found in the nanoparticles are in accordance with a previous study of the group [54] in which the main compounds identified in the XANES measurement for the Cu/CeO_2

nanoparticle were CuO and $CuCl_2 \cdot 2H_2O$. The $Cu(OH)_2$ compound comes from the aging of the nanoparticle, and it was not present in the Cu nanoparticles of the previous work [54].

The Cu-CeO_{2-x} nanoparticles present different properties, which should influence on the catalytic activity. In order to probe how these properties affect the reactivity of the nanoparticles towards the CO oxidation reaction, time-resolved Mass Spectrometry measurements were performed.

5.2 Characterization of the nanoparticles during and after the CO oxidation reaction

5.2.1 Time-resolved Mass Spectrometry measurements

The time-resolved Mass Spectrometry measurements were performed during the full thermal treatment (see Figure 4.3). Figure 5.9 presents the CO_2 detection as a function of time during the CO oxidation reaction at 250 °C, in which the samples were exposed to 100 mL/min 5 % CO + 95 % He and 50 mL/min 5% O_2 + 95 % He. Aiming to obtain the fraction of CO molecules that were oxidized to CO_2, the CO_2 signal was normalized by the sum of the CO and CO_2 signals measured considering the correction factor for detection. The data were also normalized by the mass of the Cu-CeO_{2-x} nanoparticles. Besides using the same mass for all samples, EDS measurements showed the presence of different amounts of the NaCl compound. This implies that, for the same sample mass, a different mass of Cu-CeO_{2-x} nanoparticles was present.

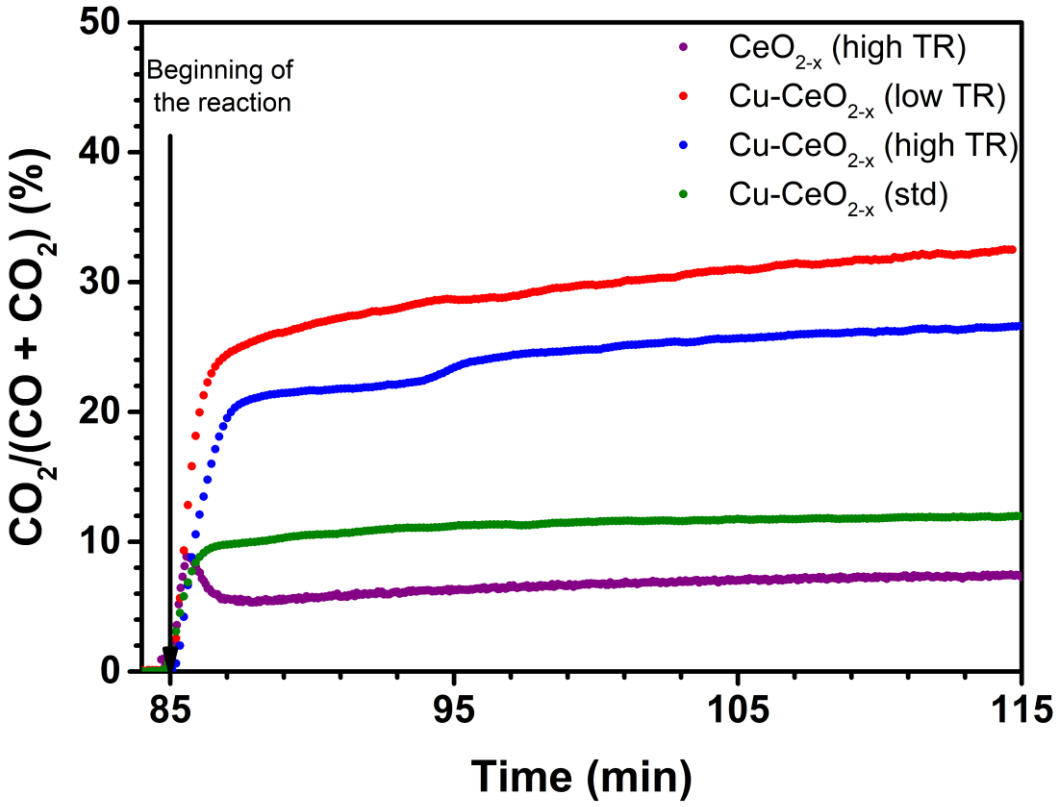

Figure 5.9: Time-resolved Mass Spectrometry measurements of the CO_2 production during the CO oxidation reaction at 250 °C for different nanoparticles. The CO_2 current signal was normalized by the sum of the CO and CO_2 signal measured at the same time and the CuO-CeO_2 mass used during the measurement. The time scale meaning is described in Figure 4.3 and corresponds to the CO oxidation reaction period.

In Figure 5.9 is noticed that in all cases the CO_2 signal started to be detected at almost the same time the O_2 gas was added to the atmosphere and the CO oxidation reaction started. The Cu-CeO_{2-x} (low TR) nanoparticles present the highest reactivity for the CO oxidation reaction during the full reaction process, oxidizing more than 30% of the inlet CO gas at the end of the reaction period. This sample shows a slight increase of the CO_2 production during the period the sample was exposed to the CO + ½ O_2 atmosphere, indicating this sample is still being activated during the first 30 min of the reaction. The Cu-CeO_{2-x} (std) nanoparticles present the lowest reactivity (around 10 % of CO oxidation), between the Cu-CeO_{2-x} nanoparticles, during the full period of the CO oxidation reaction, showing a constant CO_2 production during this period. It is important to highlight that the CO oxidation reaction was performed at temperatures much smaller than those currently used for catalysts containing noble metal nanoparticles (see Section 2.3). It is interesting to note that the Cu-CeO_{2-x} (high TR) nanoparticles show an increase, step-shaped, at around 95 min, when it becomes stable.

It occurred due to the H_2O detection from residual molecules (not shown here) in the beginning of the exposition to O_2, then decreasing the relative current of CO_2. Besides these Cu-CeO_{2-x} nanoparticles, the CeO_{2-x} (high TR) nanoparticles (without Cu) were also measured for the CO oxidation reaction and present a reactivity lower than that of the Cu-CeO_{2-x} (std) during the full reaction time, showing that the Cu nanoparticles have a key role in the CO oxidation reaction on Cu-CeO_{2-x} nanoparticles. Also, the CeO_{2-x} (high TR) nanoparticles present a peak in the beginning of the CO oxidation reaction. This is a typical behavior observed in catalysis for different catalytic reactions, and it is due to the decrease on the reactivity of the nanoparticles during the reaction. Moreover, as observed above, the Cu-CeO_{2-x} (low TR) nanoparticles present an increase in the CO_2 signal during the reaction time used and will show this decrease in the catalytic activity, after a time longer than 30 min.

The CO oxidation reaction was also performed at 150 °C and the results of the time-resolved Mass Spectrometry measurements for the CO_2 production, obtained by applying the same normalization procedure used for the reaction at 250 °C, are presented in Figure 5.10.

It can be noticed that the Cu-CeO_{2-x} (high TR) nanoparticles present the highest reactivity during the full reaction period, what is opposite to the results at 250 °C. The Cu-CeO_{2-x} (std) nanoparticles present a negligible CO_2 production at the beginning of the reaction, which decreases rapidly to zero, indicating that these nanoparticles are not active for the CO oxidation reaction in this temperature. The same happens for the CeO_{2-x} (high TR) nanoparticles, which have a CO_2 production very similar to the Cu-CeO_{2-x} (std) nanoparticles at 150 °C, decreasing rapidly to zero during the CO + ½ O_2 exposition. All samples present a CO_2 production around one order of magnitude smaller than the case at 250 °C.

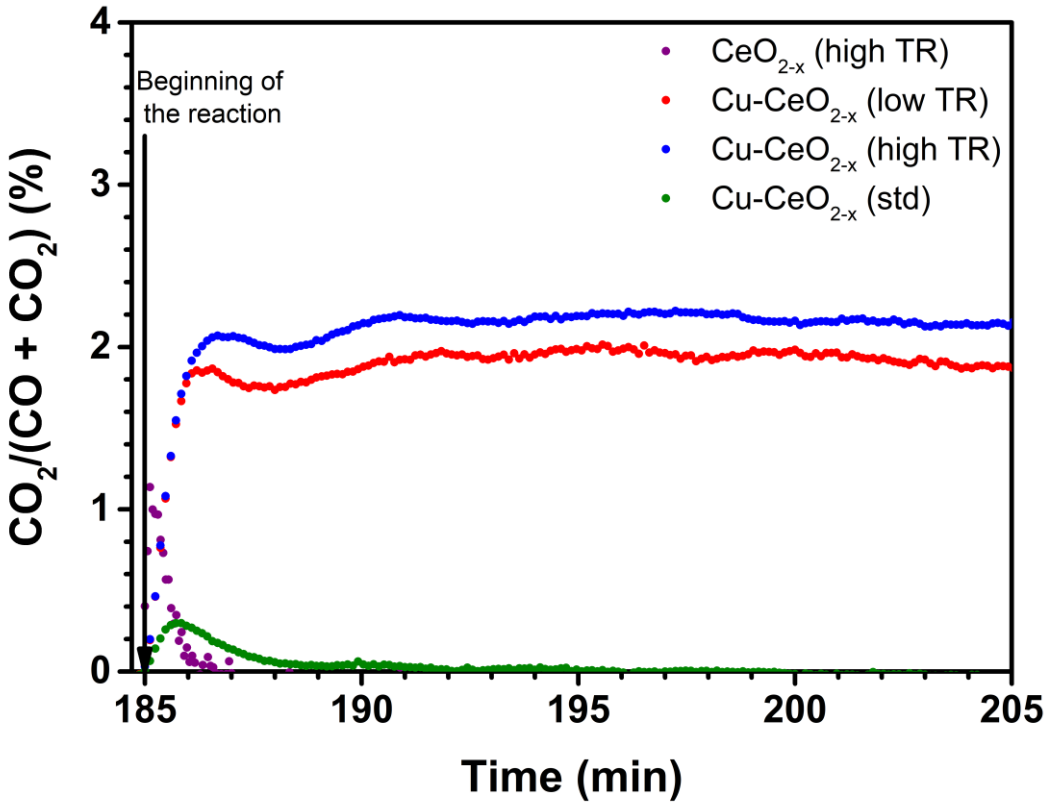

Figure 5.10: Time-resolved Mass Spectrometry measurements of the CO_2 production during the CO oxidation reaction at 150 °C for different nanoparticles. The CO_2 current signal was normalized by the sum of the CO and CO_2 signal measured at the same time and the CuO-CeO_2 mass used during the measurement. The time scale meaning is described in Figure 4.3 and corresponds to the CO oxidation reaction period.

The EDS measurements of the samples after the full thermal treatment applied (not shown here) revealed approximately the same (CuO)/(CeO_2 + CuO) weight fraction than the corresponding as-prepared sample, showing that the samples did not lose a significant amount of nanoparticles during the thermal treatment.

In order to study how the oxidation state of the nanoparticle changes during the gas treatment, which should influence on the reactivity of the samples for the CO oxidation reaction, *in situ* time-resolved XANES measurements were performed during the reduction and CO oxidation reactions.

5.2.2 *In situ* time-resolved XANES measurements

5.2.2.1 Ce L_3 edge

Figure 5.11 (a) shows typical *in situ* time-resolved XANES spectra at the Ce L_3 edge during the thermal treatment applied for the Cu-CeO_{2-x} (low TR) nanoparticles. Figure 5.11 (b) presents the CeO_2 and $CeOHCO_3$ standard spectra, related to the Ce(IV) and Ce(III) components, respectively. The Ce(IV) standard presents two peaks after the absorption edge, while the Ce(III) standard presents only one intense peak. By comparing these standard spectra to the initial Ce L_3 edge spectrum in Figure 5.11 (a), it can be noticed that this initial spectrum is similar to that of Ce(IV) standard, presenting two peaks near the absorption edge. This shows that the Ce atoms in the Cu-CeO_{2-x} (low TR) nanoparticles are highly oxidized, as expected from the XRD and XPS results of the as-prepared nanoparticles. During the heating process to 400 °C in a CO atmosphere, the XANES spectra change and it is possible to observe an increase of the first peak intensity in comparison to the second one, showing the reduction of the CeO_{2-x} nanoparticles since the *in situ* XANES spectra becomes more similar to the Ce(III) standard spectrum.

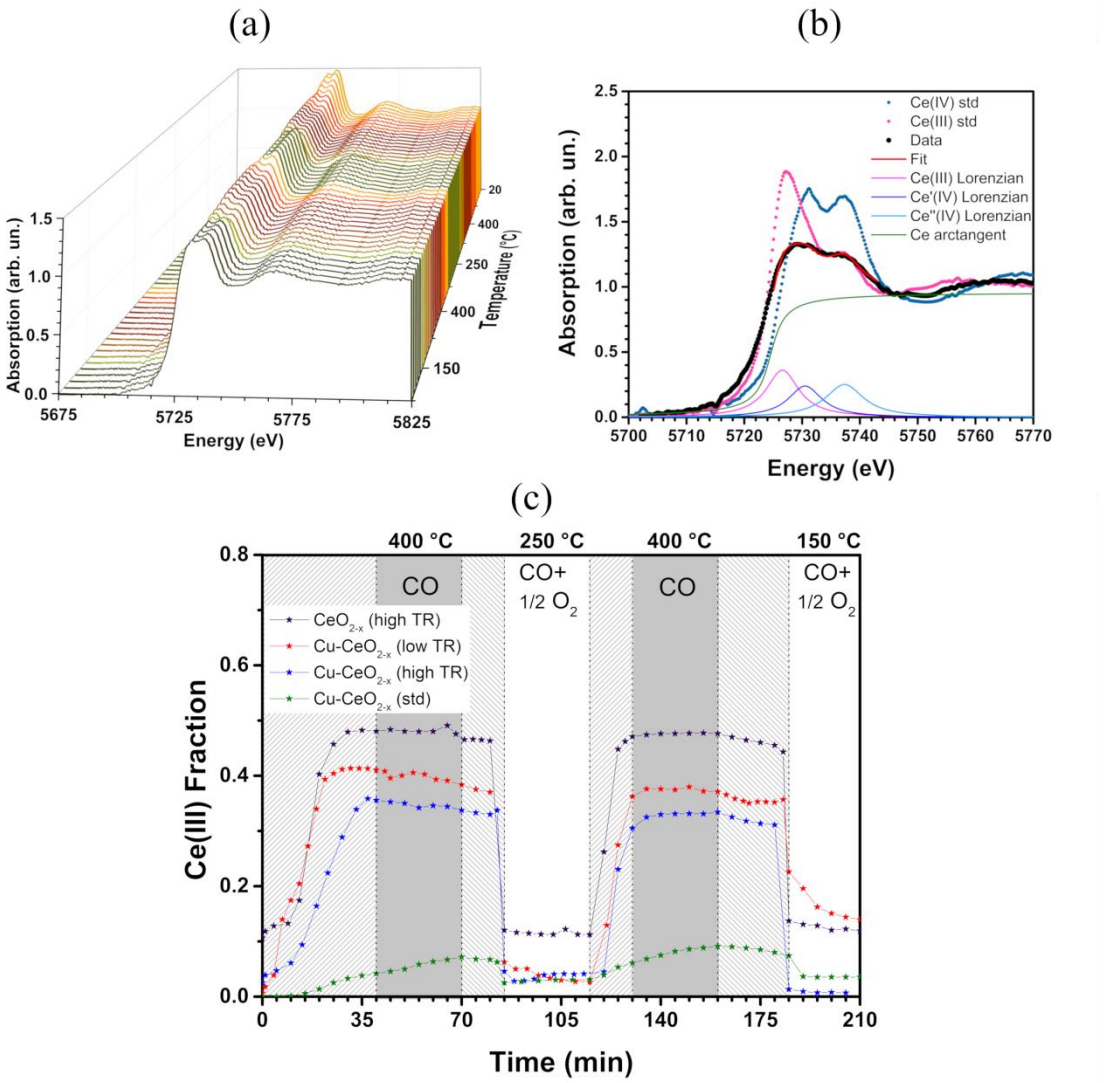

Figure 5.11: (a) *In situ* time-resolved XANES spectra measured at the Ce L_3 edge of the Cu-CeO_{2-x} (low TR) nanoparticles during the full thermal treatment applied. The spectra in orange, brown and dark green represent the heating treatment in CO atmosphere, the isothermal reduction treatment in CO atmosphere and the isothermal CO oxidation reaction in CO + ½ O_2 atmosphere, respectively. (b) Typical XANES spectrum at the Ce L_3 edge and the respective fitting for the CeO_{2-x} (low TR) nanoparticles at 400 °C exposed to the CO reducing atmosphere, and the CeO_2 and $CeOHCO_3$ standards spectra, related to the Ce(IV) and Ce(III) oxidation states, respectively. (c) Time evolution of the Ce(III) fraction for the nanoparticles as a function of the time, related to the temperature and atmosphere used as presented in Figure 4.3. The region filled with diagonal lines refers to the heating (diagonal lines increasing to the right) and cooling (diagonal lines increasing to the left) under CO atmosphere. The areas filled with solid colors refers to the isothermal processes related to the reduction at 400 °C under CO atmosphere (gray area) and the CO oxidation reaction at 250 °C and 150 °C under CO + ½ O_2 atmosphere (white area).

During the CO oxidation reaction, represented in dark green, the XANES spectra becomes, again, similar to that of the Ce(IV) standard, showing an oxidation of the CeO_{2-x} nanoparticles. The oxidation and reduction processes occur for all Cu-CeO_{2-x} nanoparticles during the thermal treatment.

In order to quantify the Ce(III) fraction as a function of the temperature and atmosphere used in the experiments, the *in situ* XANES spectra were fitted to 3 Lorentzian and 1 arctangent function, as described in Section 4.7 [88]. Figure 5.11 (b) shows a typical fitting of the XANES spectrum at the Ce L_3 edge for the Cu-CeO_{2-x} (low TR) nanoparticles during the reduction treatment at 400 °C. Figure 5.11 (c) shows a comparison of the Ce(III) fraction among the different nanoparticles as a function of time during reduction and CO oxidation reactions.

During the CO reduction treatment, the CeO_{2-x} from the Cu-CeO_{2-x} (low TR) nanoparticles starts to reduce before the other nanoparticles, in a lower temperature (around 110 °C), which was observed in the previous study [34]. In fact, it represents the lowest reduction temperature among the nanoparticles synthesized in the previous work [34]. The Cu-CeO_{2-x} (low TR) nanoparticles present the highest Ce(III) fraction during reduction treatment among the nanoparticles with Cu investigated in this work. In the previous work [34] it was observed that the CeO_{2-x} (high TR) nanoparticle (without Cu) presented the highest Ce(III) fraction at 400 °C under a CO atmosphere between the synthesized nanoparticles. Moreover, during the reduction treatment, the CeO_{2-x} (high TR) nanoparticles present a Ce(III) fraction higher than that of the Cu-CeO_{2-x} (high TR) nanoparticles. These two observations show that the Cu nanoparticles change the reduction properties of the CeO_{2-x} nanoparticles. This change is explained by a charge transfer process, where the CeO_{2-x} nanoparticles transfer electrons to the Cu nanoparticles. In fact, it was already suggested for this kind of system in the previous work of the group [53]. This process occurs for all synthesized Cu-CeO_{2-x} nanoparticles. However, in the previous work of the group [34], it was observed that only the CeO_{2-x} (high TR) nanoparticles presented mesopores (see Figure 4.1), with a mean diameter similar to that obtained by TEM for the Cu nanoparticles. Hence, some of these Cu nanoparticles may be located inside the mesopores, which decreases the sintering of the Cu nanoparticles during the reduction treatment in the Cu-CeO_{2-x} (high TR) nanoparticles. This sintering process occurs in the other nanoparticles due to the high temperatures involved [98], decreasing the contact area between the Cu and CeO_{2-x} nanoparticles, thus decreasing the charge transfer rate. This change in the contact area may explain also the change in the relative Ce(III) fraction of the Cu-CeO_{2-x} (low TR) and Cu-CeO_{2-x} (high TR) nanoparticles when compared to the previous work [34].

It was observed that the synthesized nanoparticles present a higher Ce(III)

fraction during the reduction treatment than the Cu-CeO_{2-x} (std) nanoparticles. The Cu-CeO_{2-x} (low TR) nanoparticles, which presents the highest reactivity towards CO oxidation, presents also the highest Ce(III) fraction during the reduction treatment between the Cu-CeO_{2-x} nanoparticles, meaning it has the highest O vacancy population available. The Cu-CeO_{2-x} (std) nanoparticles, that shows the lowest reactivity towards CO oxidation, presents the lowest Ce(III) fraction during the reduction treatment. It indicates that there is a direct relation between the initial Ce(III) fraction (before reaction and at the end of reduction treatment) and the reactivity of the Cu-CeO_{2-x} nanoparticles for the CO oxidation reaction. It is known from the literature that the O vacancy population of CeO_{2-x} is important for the CO oxidation reaction and that a higher O vacancy population at the beginning of the reaction would increase the reactivity of the nanoparticles [32]. During the CO oxidation reaction, at 250 °C, the Cu-CeO_{2-x} nanoparticles presented a similar Ce(III) fraction, lower than 5 %, showing the CeO_{2-x} nanoparticles oxidize rapidly in the presence of O_2 atmosphere.

On the other hand, in the CO oxidation reaction at 150 °C is observed that the Cu-CeO_{2-x} (high TR) nanoparticles, which have the highest reactivity in this temperature, was also the sample with the lowest Ce(III) fraction between the synthesized nanoparticles. Interestingly, these nanoparticles have a Ce(III) fraction similar to the Cu-CeO_{2-x} (std) nanoparticles, where the reactivity is negligible. Note that there is a different dependence of the reactivity towards CO oxidation and the Ce(III) fraction at 250 °C and 150 °C. It shows that the O vacancies population itself cannot explain the reactivity results observed and there are other important factors to be taken into account. However, for both temperatures (150 °C and 250 °C) the sample with the highest reactivity presents a small Ce(III) fraction of around 5 % during the CO oxidation reaction. It shows that the re-oxidation of the CeO_{2-x} nanoparticles is also important for the CO oxidation reaction occurrence, then filling the CeO_{2-x} lattice with O ions that participate on the reaction directly [36] or participate on the re-oxidation of the Cu atoms [38]. In both CO oxidation mechanism (see Section 2.5), a high O ions population available in the CeO_{2-x} lattice is a key factor for the reaction to occur, being the oxidation of the nanoparticles the limiting step for the CO oxidation reaction [49]. Sayle et al. [33] studied the activation energy for the CO oxidation reaction over CeO_{2-x} nanoparticles by molecular dynamics calculations. The authors observed that the activation energy for the CO oxidation reaction on CeO_{2-x} nanoparticles changes with

the nanoparticle size, the presence of mesoporous and the Ce(III) fraction. Thus, there is an ideal Ce(III) fraction during the CO oxidation reaction that optimize the catalytic results and this fraction is dependent on the morphology of the CeO_{2-x} nanoparticles. The authors concluded that the lowest activation energy was achieved by small CeO_{2-x} nanoparticles (d = 3.5 nm) with a low Ce(III) fraction (4 % - 10 %). This size is similar to the Cu-CeO_{2-x} (high TR) nanoparticle that presents the highest reactivity at 150 °C. However, at 250 °C, other effects related to the interaction between the Cu and CeO_{2-x} nanoparticles become important and should be considered.

Considering this and in order to analyze how the oxidation state of the Cu nanoparticles evolutes during the thermal treatment applied, time-resolved *in situ* XANES measurements at the Cu K edge were performed.

5.2.2.2 Cu K edge

Figure 5.12 (a) shows a typical time-evolution of the XANES spectra at the Cu K edge for the Cu-CeO_{2-x} (low TR) nanoparticles during reduction and CO oxidation reactions. The Cu nanoparticles are initially fully oxidized, presenting a XANES spectrum (measured at room temperature) very similar to the CuO standard spectrum, which presents an intense peak after the absorption edge. During the first heating process to 400 °C with the sample exposed to a CO atmosphere (orange spectra), the XANES fingerprint changes with the decrease of the intensity in the peak after the absorption edge. The Cu K edge represents a transition from the 1s to 4p electronic level. Thus, the reduction of the intensity of this peak is related to the occupation of the Cu 4p electronic level, then showing the reduction of the Cu nanoparticles. Besides that, it is possible to notice a shift in the absorption edge energy during the reduction treatment to smaller energies, again in accordance to the results expected for the reduction of Cu atoms. In fact, the XANES spectra during reduction treatment present the same fingerprints than the Cu(0) standard spectrum (Figure 5.8). The Mass Spectrometry measurements during the reduction treatment (not shown here) show a small CO_2 signal that appears due to the reaction between the CO and the O present in the Cu or CeO_{2-x} nanoparticles since both Cu and Ce atoms are reducing.

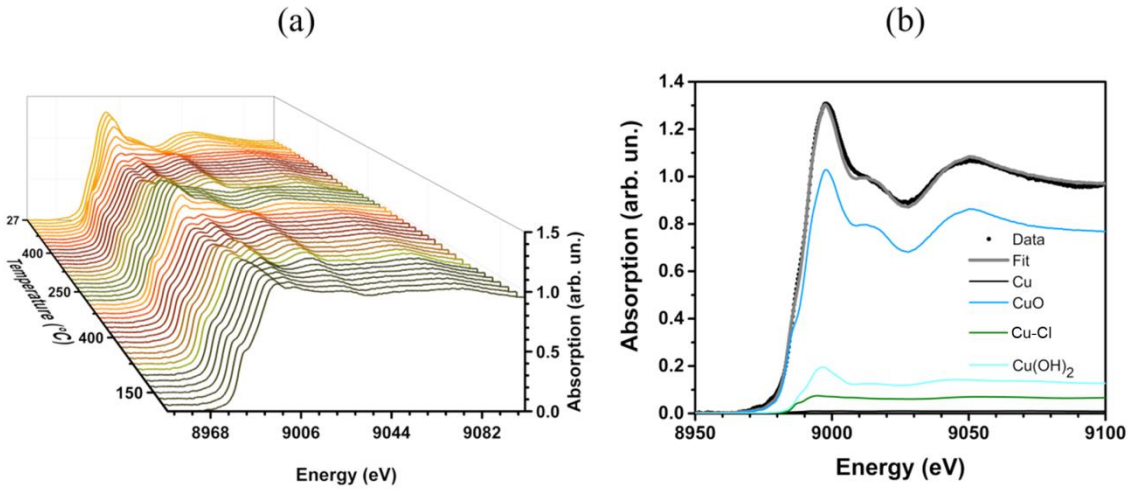

Figure 5.12: (a) Typical *in situ* time-resolved XANES spectra measured at the Cu K edge of the Cu-CeO_{2-x} (low TR) nanoparticles during the full thermal treatment applied. The spectra in orange, brown and dark green represent the heating treatment in CO atmosphere, the isothermal reduction treatment in CO atmosphere and the isothermal CO oxidation reaction in CO + 1/2 O_2 atmosphere, respectively. (b) XANES measurement at the Cu K edge and the respective fitting for the as-prepared Cu-CeO_{2-x} (low TR) nanoparticles and the Cu, CuO, Cu-Cl and $Cu(OH)_2$ standard spectra.

In the dark green regions of Figure 5.12(a), corresponding to the CO oxidation reaction at 250 °C (first treatment) and 150 °C (second treatment), it is possible to see that the intensity of the peak after the absorption edge increases, which is related to an increase on the number of empty electronic states at the Cu 4p level, then indicating the oxidation of the Cu nanoparticles. This increase is more evident in the reaction at 250 °C, indicating a stronger oxidation of the Cu nanoparticles during the CO oxidation reaction at 250 °C than at 150 °C.

In order to quantify the Cu compounds fraction present in the Cu nanoparticles as a function of time, a linear combination fitting of the XANES spectra was performed. Figure 5.12 (b) presents a typical fitting of the XANES spectrum for the as-prepared Cu-CeO_{2-x} (low TR) nanoparticles. The fraction of each component is schematically represented by the intensity of the corresponding XANES spectrum of the standard used in the fitting procedure. Figure 5.13 presents a comparison between the evolution of the Cu compounds fraction, namely CuO, Cu_2O and Cu(0), as a function of the temperature and atmosphere exposure of the nanoparticles. The Cu nanoparticles initially have a high amount of CuO (between 70% and 80%). Moreover, there is also a small amount of Cu-Cl and $Cu(OH)_2$ (lower than 20 %), as presented in Table 5.6. However, during the reduction treatment, the Cu-Cl and $Cu(OH)_2$ compounds fractions go rapidly to zero (not shown here).

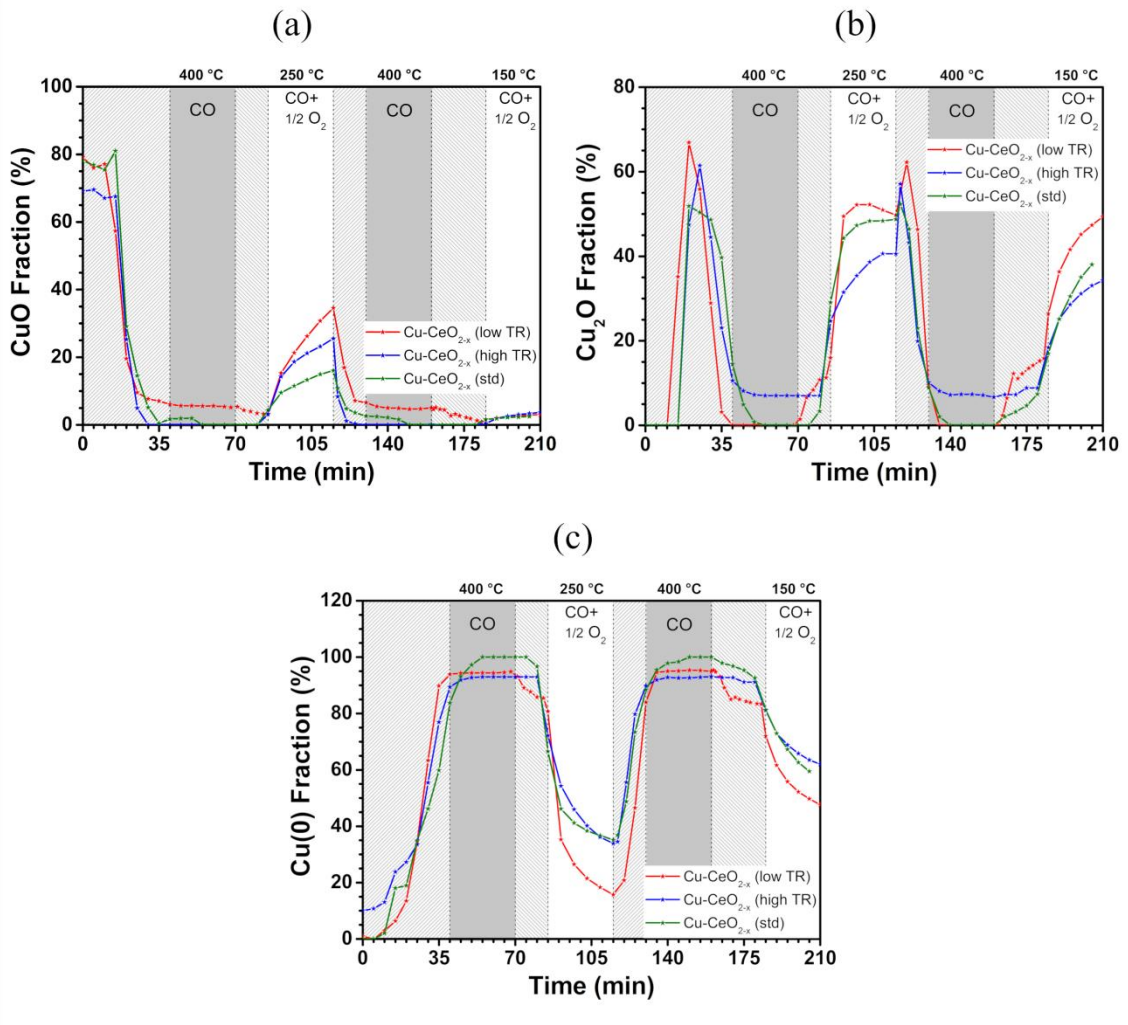

Figure 5.13: Time evolution of the (a) CuO, (b) Cu_2O and (c) Cu(0) compounds fractions obtained from the fit of the time-resolved *in situ* XANES spectra measured at the Cu K edge. The region filled with diagonal lines refers to the heating (diagonal lines increasing to the right) and cooling (diagonal lines increasing to the left) under CO atmosphere. The areas filled with solid colors refers to the isothermal process related to the reduction at 400 °C under CO atmosphere (gray area) and the CO oxidation reaction at 250 °C and 150 °C under CO + ½ O_2 atmosphere (white area).

It can be observed that during the reduction treatment the Cu nanoparticles change from CuO to Cu_2O and lastly to Cu(0), as expected [54, 99]. The reduction temperature of the Cu nanoparticles is obtained from the inflection point of the curve related to the CuO fraction as a function of temperature (Figure 5.13 (a)). The Cu-CeO_{2-x} (low TR) nanoparticles presented the smaller reduction temperature of the Cu nanoparticles, starting to reduce at around 200 °C. The Cu-CeO_{2-x} (high TR) and Cu-CeO_{2-x} (std) nanoparticles started to reduce at around 230 °C. The change in the reduction temperature is directly related to the reduction temperature of the CeO_{2-x} nanoparticles used (see Figure 5.11) and is related to the interaction between the Cu and CeO_{2-x}

nanoparticles since the reduction of the Cu-CeO_{2-x} nanoparticle starts at the interface between the Cu and CeO_{2-x} nanoparticles [56]. It can be seen that all nanoparticles at 400 °C are essentially reduced, presenting a high Cu(0) fraction. The Cu-CeO_{2-x} (std) nanoparticles are fully reduced, while the other two samples present almost the same fraction of Cu(0) of around 90 %. It is interesting to note the presence of around 10% CuO and Cu_2O for the Cu-CeO_{2-x} (low TR) and Cu-CeO_{2-x} (high TR) nanoparticles, respectively. The difference in the oxidation state of the Cu-CeO_{2-x} nanoparticles is related to the charge transfer from the CeO_{2-x} to the Cu nanoparticle, discussed in Section 5.2.2.1. It is observed that the Cu-CeO_{2-x} (low TR) nanoparticles, which have the highest Ce(III) fraction, presents 10 % CuO compound at 400 °C, while the Cu-CeO_{2-x} (high TR), which presents an intermediate Ce(III) fraction, presents 10 % of Cu_2O compound, meaning it is less oxidized due to a lower charge transfer rate. Lastly, the Cu-CeO_{2-x} (std), which presents 100 % Cu(0), presents the lowest Ce(III) fraction, thus, the lowest charge transfer rate between the Cu and Ce atoms. During the cooling process to 250 °C and 150 °C with exposure to the CO atmosphere, the Cu nanoparticles remained with the same oxidation state, with exception of the Cu-CeO_{2-x} (low TR) nanoparticles. This sample presented an indicative of a decrease on the Cu(0) and CuO fractions and an increase of the Cu_2O fraction. Note that the same effect is present in the two different cooling process performed in this sample (from 400 °C to 250 °C and to 150 °C). The oxidation of the Cu nanoparticles during cooling in a reduction atmosphere is an indicative of the geometrical factor of the SMSI effect [51], which starts to occur in the Cu-CeO_{2-x} (low TR) nanoparticles after 30 minutes of reduction at 400 °C. The SMSI effect is characterized by two factors, an electronic and a geometrical one. The electronic effect is related to a charge transfer between the support and the metallic nanoparticle. In a previous work of the group, it was observed a charge transfer from the metallic nanoparticle to the support for Au-based nanoparticles supported on CeO_2 [50] and a charge transfer from the support to the metallic nanoparticles for Cu-Ni [54] and Ni [53] nanoparticles supported on CeO_2. In this work, the discussion presented in Section 5.2.2.1 is consistent with the charge transfer from the support to the metallic nanoparticles at temperatures smaller than 400 °C. The geometrical factor of the SMSI is characterized by the presence of a capping layer from the support surrounding the metallic nanoparticles. It occurs for temperatures higher than those where the electronic effect occurs [52]. This effect is only observed when the sample is exposed to a reducing atmosphere. The capping layer is removed when the

nanoparticles are exposed to O_2 [100]. Thus, it should not influence on the reactivity of the Cu-CeO_{2-x} (low TR) nanoparticles on the CO oxidation reaction since the nanoparticles are highly oxidized in this case.

During the CO oxidation reaction at 250 °C it is possible to observe that the Cu-CeO_{2-x} (high TR) nanoparticles oxidize slower than the other nanoparticles, while the Cu-CeO_{2-x} (low TR) nanoparticles present the fastest decrease in the Cu(0) fraction. The Cu-CeO_{2-x} (low TR) nanoparticles present the highest Cu_2O and CuO fractions during the CO oxidation reaction at 250 °C. The Cu-CeO_{2-x} (high TR) nanoparticles present the lowest Cu_2O fraction, while the Cu-CeO_{2-x} (std) presents the lowest CuO fraction during the CO oxidation reaction at 250 °C. The difference in the reduction and oxidation properties of the Cu nanoparticles occurs due to the interaction of the Cu nanoparticles with the CeO_{2-x} nanoparticles. Also, many different effects take place when the nanoparticles are heated to high temperatures, such as 400 °C, under a reductive atmosphere such as sintering [98] and change on the shape of the nanoparticles [101]. These effects influence on the interaction between the Cu and CeO_{2-x} nanoparticles, then changing the oxidation states.

The Mass Spectrometry measurements (Figure 5.9) showed that the Cu-CeO_{2-x} (low TR) nanoparticles presented the highest reactivity towards the CO oxidation reaction, followed by the Cu-CeO_{2-x} (high TR) and Cu-CeO_{2-x} (std) nanoparticles at 250 °C. The trend meets that observed for the CuO fraction during the CO oxidation reaction at 250 °C, indicating that the CuO compound plays a key role for the CO oxidation reaction. It shows that the CO oxidation reaction on Cu-CeO_{2-x} nanoparticles occurs following the Mechanism I [38, 7, 39, 40] presented in Section 2.5, where the CO adsorption occurs at the Cu(II) species. After this, the reaction occurs with the O donated by the Cu nanoparticles. Finally, the re-oxidation of the Cu nanoparticles occurs with the O given by the CeO_{2-x} nanoparticle, which adsorbs the O from the atmosphere. The O donated to the Cu nanoparticle comes from the O ions adsorbed in the O vacancies of the CeO_{2-x} nanoparticles which explains the differences in the CuO fraction between the nanoparticles. It is observed that the nanoparticles with the highest O vacancies population before reaction (Cu-CeO_{2-x} (low TR)) present the highest CuO fraction, while that with the lowest O vacancies population (Cu-CeO_{2-x} (std)) presents the lowest CuO fraction.

It is possible to notice that the nanoparticles present essentially the same CuO fraction of around 5 % during the CO oxidation reaction at 150 °C. This fraction is much smaller than that present in the Cu nanoparticles during the CO oxidation reaction at 250 °C (higher than 10%). Moreover, the Cu-CeO_{2-x} (low TR) nanoparticles presented the highest Cu_2O fraction, while the Cu-CeO_{2-x} (high TR) nanoparticles presented the lowest one. For this temperature, the Mass Spectrometry measurements showed that the Cu-CeO_{2-x} (high TR) nanoparticles presented the highest reactivity towards CO oxidation reaction and the Cu-CeO_{2-x} (std) nanoparticles the lowest one among the nanoparticles containing Cu. These results indicate that the Cu_2O compound does not participate actively in the CO oxidation reaction over Cu-CeO_{2-x} nanoparticles, as proposed by the Mechanism II described in Section 2.5 [36, 37, 42, 43], then confirming that the CuO is the active compound for the CO oxidation reaction. Since at 150 °C all nanoparticles presented the same CuO fraction, the difference in the reactivity comes due to differences in the oxidation state of the CeO_{2-x} nanoparticles during the CO oxidation reaction. The nanoparticles with highest reactivity (Cu-CeO_{2-x} (high TR)) have the optimal Ce(III) fraction of around 5 % proposed by Sayle et al [33]. Also, in this temperature the CeO_{2-x} nanoparticle donates O to the Cu atoms, following the same mechanism presented for the CO oxidation reaction at 250 °C, but in lower rates due to the lower temperature, thus forming a small CuO concentration. Moreover, it is possible to notice that the sample without Cu nanoparticles, CeO_{2-x} (high TR), presents the highest Ce(III) fraction, indicating that the re-oxidation does not occur significantly since there is CO and O_2 available to reduce and oxidize the CeO_{2-x} nanoparticles in this case, instead of only an O_2 atmosphere due to the interaction between CO and Cu in the Cu-CeO_{2-x} (high TR) nanoparticles.

In order to observe how the local atomic order around the Cu atoms changes during the reduction treatment and CO oxidation reaction, a Fourier Transform of the EXAFS oscillations, extracted from the time-resolved XAS spectra obtained, was performed. Figure 5.14 presents a typical time-evolution of the Fourier Transform of the EXAFS oscillations displayed in Figure 5.12 (a). The change in the peak position of the coordination shell indicates a change on the distance between the absorbing and scattering atoms, which is related to a change in the scattering neighbor element. Also, the intensity of the peak is related to the coordination number around the Cu atoms. Initially (Fourier Transform in orange in Figure 5.14 (a)), the most intense peak

observed is due to a Cu-O scattering. During the reduction treatment, the Cu-O scattering peak decreases and a Cu-Cu scattering peak appears, indicating the reduction of the Cu nanoparticles. In the CO oxidation reaction at 250 °C, the Cu nanoparticles oxidize again, increasing the peak related to the Cu-O scattering component. In the second reduction treatment applied (Figure 5.14 (b)), the Fourier Transform is similar to that of the first reduction treatment, showing qualitatively that the reduction treatment returns the local atomic order to that found during the first reduction treatment. During the CO oxidation reaction at 150 °C, the peak related to the Cu-Cu scattering is more intense than that related to the Cu-O scattering peak, in opposition to the behavior observed at 250 °C. It shows that the Cu nanoparticles during the CO oxidation reaction at 150 °C oxidize less than during the CO oxidation reaction at 250 °C, as observed in the XANES analysis at the Cu K edge (Figure 5.13). Then the local atomic order around Cu atoms plays a key role on the reactivity towards CO oxidation reaction for Cu-CeO_{2-x} nanoparticles.

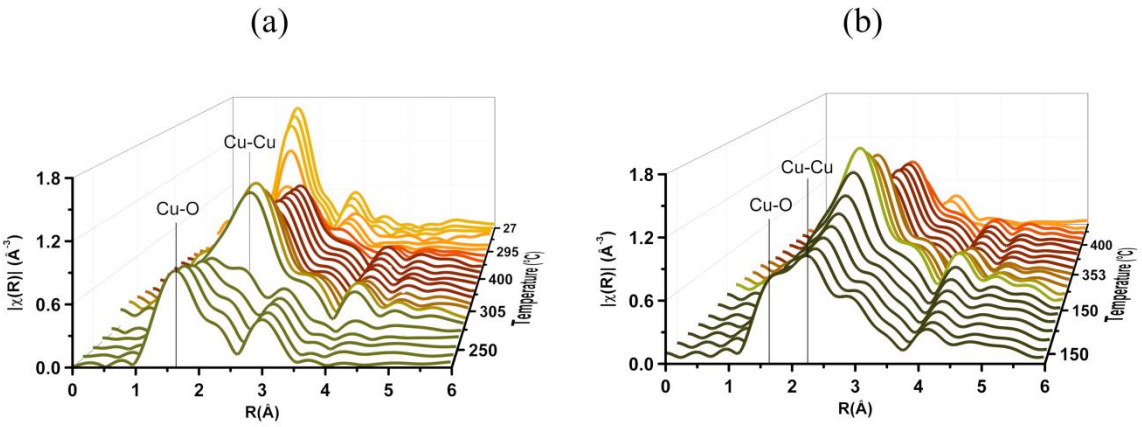

Figure 5.14: Typical time-evolution of the Fourier Transform obtained from the EXAFS oscillations of the *in situ* XAS spectra measured at the Cu K edge during reduction treatment at 400 °C and CO oxidation reaction at (a) 250 °C and (b) 150 °C for the Cu-CeO_{2-x} (low TR) nanoparticles.

Aiming to obtain quantitative information about the local atomic order around the Cu atoms from the Fourier Transforms obtained from the XAS spectra, high resolution measurements were performed at the XAFS2 beamline at LNLS, during the reduction treatment and the CO oxidation reaction.

5.2.3 *In situ* EXAFS measurements

Figure 5.15 (a) and (b) presents a comparison of the EXAFS oscillations and the

respective Fourier Transform at the Cu K edge between the Cu-CeO_{2-x} nanoparticles during reduction treatment at 400 °C and the Cu(0) standard. The EXAFS oscillations and the Fourier Transforms are very similar to the Cu(0) standard but with damped oscillations. It is related to a smaller number of scattering neighbors (related to a smaller size) and/or a higher thermal and structural disorder. Also, it is possible to observe that the Cu-CeO_{2-x} (std) nanoparticles present the smaller intensity of the Cu-Cu scattering peak between the samples, which is related to a higher structural disorder when compared to the other synthesized nanoparticles. Additionally, it is possible that the mean size of the Cu nanoparticles changed due to the sintering process [98] which depends on the nature of the Cu-CeO_{2-x} interface, then changing the coordination number of the Cu-Cu scattering path. It can be observed that the Cu-CeO_{2-x} (low TR) and Cu-CeO_{2-x} (std) nanoparticles present also a small contribution from the Cu-O scattering. Based on the XANES analysis, the Cu-O scattering probably comes from the small amount of Cu_2O detected.

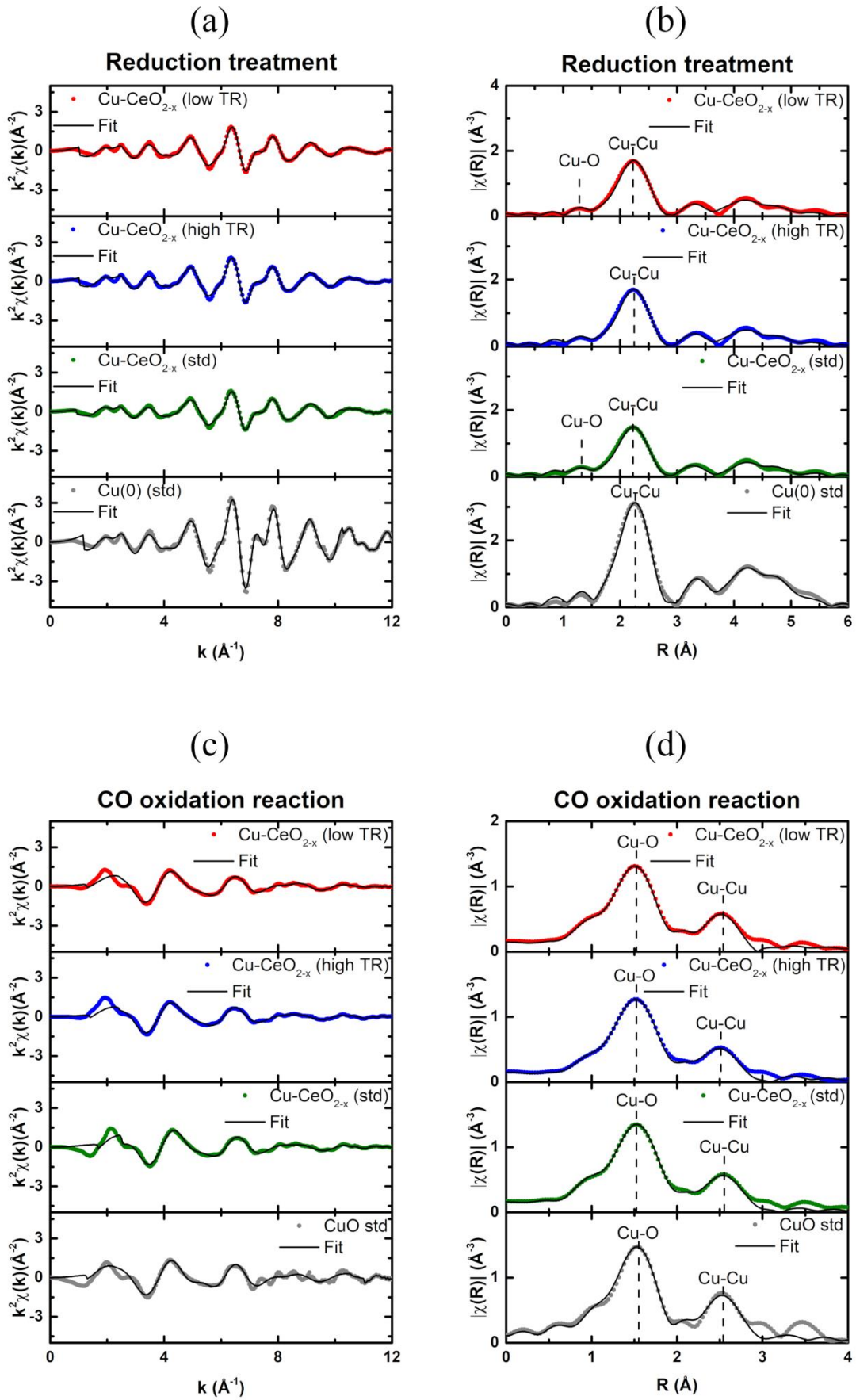

Figure 5.15: EXAFS oscillations ((a) and (c)) and the corresponding Fourier Transforms ((b) and (d)) at the Cu K edge during reduction treatment ((a) and (b)) and CO oxidation reaction ((c) and (d)) at 250 °C.

Figure 5.15 (c) and (d) presents a comparison of the EXAFS oscillations and the respective Fourier Transform between the Cu-CeO_{2-x} nanoparticles during CO oxidation reaction at 250 °C and the CuO standard. The Fourier Transforms for the Cu-CeO_{2-x} nanoparticles are similar to that obtained from the CuO standard, in accordance to the result observed in the *in situ* time-resolved XANES spectra (Figure 5.13). Moreover, the Fourier Transform presents the intensity of the Cu-O and Cu-Cu scattering paths slightly smaller than that of the CuO standard, which comes mainly from the higher temperature of the measurement. In spite of this, since the intensities are similar, it shows that the disorder factor and the coordination number around Cu atoms are not very different to the CuO standard. It indicates the occurrence of sintering in the Cu nanoparticles induced by the O_2 atmosphere. In order to obtain quantitative information from the EXAFS analysis, the EXAFS oscillations and the Fourier Transform were fitted. Table 5.7 and Table 5.8 present the parameters (coordination shell) obtained from the fitting procedure of the EXAFS oscillations and the Fourier Transform during reduction treatment and CO oxidation reaction, respectively.

Table 5.7: Parameters obtained from the quantitative analysis of the EXAFS data for the Cu-CeO_{2-x} nanoparticles measured at the Cu K edge during reduction treatment at 250 °C.

Scattering Path		**Cu(0) standard**	**Cu-CeO_{2-x} (low TR)**	**Cu-CeO_{2-x} (high TR)**	**Cu-CeO_{2-x} (std)**
Cu-O	N	-	0.20 ± 0.09	-	0.1 ± 0.1
	R (Å)	-	1.45 ± 0.06	-	1.8 ± 0.1
	σ^2(Å^2)	-	0.02 ± 0.01	-	0.01± 0.01
Cu-Cu	N	12	9.8 ± 0.3	9.9 ± 0.3	8.3 ± 0.2
	R (Å)	2.547 ± 0.002	2.538 ± 0.002	2.541 ± 0.002	2.536 ± 0.002
	σ^2(Å^2)	0.0083 ± 0.0002	0.0128 ± 0.0003	0.0130 ± 0.0003	0.0124 ± 0.0003

Table 5.8: Parameters obtained from the quantitative analysis of the EXAFS data for the Cu-CeO_{2-x} nanoparticles measured at the Cu K edge during CO oxidation reaction at 250 °C.

Scattering Path		CuO standard	Cu- CeO_{2-x} (low TR)	Cu- CeO_{2-x} (high TR)	Cu- CeO_{2-x} (std)
Cu-O	N	4	3.7 ± 0.1	3.4 ± 0.1	3.39 ± 0.09
	R (Å)	1.946 ± 0.003	1.942 ± 0.004	1.950 ± 0.003	1.953 ± 0.003
	σ^2(Å^2)	0.0055 ± 0.0006	0.0063 ± 0.0006	0.0060 ± 0.0005	0.0054 ± 0.0005
Cu-Cu	N	4	3.5 ± 0.4	3.3 ± 0.3	3.2 ± 0.3
	R (Å)	2.876 ± 0.009	2.93 ± 0.01	2.9 ± 0.1	2.925 ± 0.008
	σ^2(Å^2)	0.013 ± 0.001	0.013 ± 0.001	0.012 ± 0.002	0.011 ± 0.001

During reduction treatment, the Cu-CeO_{2-x} nanoparticles present a Cu-Cu coordination number smaller than that found for the Cu(0) standard. It is expected since the coordination number decreases with the nanoparticle's size [102]. Besides that, all nanoparticles present a high Debye-Waller factor associated to the Cu-Cu scattering when compared to the Cu(0) standard, which is explained by the high thermal disorder of the Cu nanoparticles at 250 °C and the intrinsic structural disorder. The structural disorder was also observed indirectly in the XRD measurements of the as-prepared nanoparticles (Section 5.1.3) since the Cu nanoparticles of the Cu-CeO_{2-x} (low TR) and Cu-CeO_{2-x} (high TR) present a crystallite size smaller than the mean diameter obtained by TEM (Table 5.2). This difference is related to defects in the crystalline structure of the as-prepared Cu nanoparticles. The results related to the structural disorder obtained by XRD, for the as-prepared nanoparticles, and by EXAFS, during reduction treatment, present the same trend. Also, the Cu-CeO_{2-x} nanoparticles present the Cu-Cu scattering distance very similar to the Cu(0) standard one, but slightly shorter. This difference in the Cu-Cu distance, when compared to the Cu(0) standard, increases slightly for the Cu nanoparticles presenting the Cu-O scattering (Cu-CeO_{2-x} (low TR) and Cu-CeO_{2-x} (std)), besides the uncertainty associated to the fitting procedure applied.

Table 5.8 shows that the Cu-CeO_{2-x} (low TR) nanoparticles present the highest value for the coordination number and Debye-Waller factor associated to the Cu-O

scattering during CO oxidation reaction, while the Cu-CeO_{2-x} (std) nanoparticles present the lowest ones. The opposite trend is observed for the Cu-O scattering distance between the samples. For the Cu-Cu scattering, the same trend for the coordination number and Debye-Waller factor occurs but it is hard to conclude it due to the great uncertainty associated in these cases. For the Cu-O and Cu-Cu Debye-Waller factors, the nanoparticles present similar values than that obtained for the CuO standard, showing the samples are not much disordered, even at higher temperatures. It can be caused by the sintering of the Cu nanoparticles induced by the O_2 atmosphere. The sintering process occurs due to two factors, temperature and time. Considering the full time of the EXAFS measurement at 250 ^{o}C (it takes around 2 hours), it induces the sintering process in the nanoparticles.

The comparison between the results from the EXAFS and the Mass Spectrometry analysis shows that, in spite of the uncertainties, the nanoparticles with the highest reactivity towards CO oxidation reaction presents the highest coordination number and Debye-Waller factors related to the Cu-O and Cu-Cu scatterings during the CO oxidation reaction. Additionally, it is interesting to note that, in spite of the uncertainties associated, there is a trend of the shorter the Cu-O distance the higher the reactivity towards CO oxidation reaction. This result follows the opposite trend found for Cu/CeO_2 nanoparticles in the Water Gas-Shift (WGS) reaction, where the Cu-O distance increased due to the interaction with small CeO_{2-x} nanoparticles [103]. It shows the local atomic order plays a key role on controlling the reactivity of Cu/CeO_{2-x} nanoparticles.

5.2.4 XPS measurements

Figure 5.16 presents the XPS measurements at the Ce 3d region for the Cu-CeO_{2-x} nanoparticles after reduction treatment. As explained before, the relative intensity of the *u'''* peak indicates the oxidation state of the CeO_{2-x} nanoparticles. It is possible to notice that all nanoparticles present a similar oxidation state at the CeO_{2-x} surface.

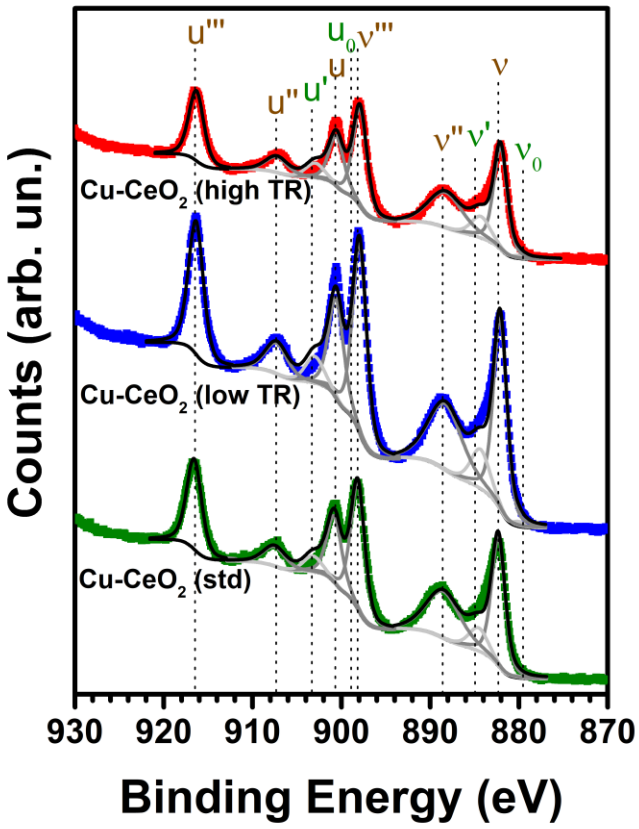

Figure 5.16: Ce 3d XPS spectra for the Cu-CeO_{2-x} nanoparticles after reduction treatment. The black points represent the Shirley background used, the black solid line the total fit performed using the dark gray (corresponding to Ce(IV) component) and light gray (corresponding to the Ce(III) component) peaks.

In order to obtain the Ce(III) fraction of the nanoparticles, the same procedure applied in the XPS spectra of the as-prepared nanoparticles was performed. Table 5.9 presents the results obtained from the fitting procedure. It is possible to notice that all nanoparticles have a small Ce(III) fraction of around 10 %. The small Ce(III) fraction obtained by XPS in comparison to the *in situ* XANES measurements comes from the exposure of the sample to the atmosphere after reduction treatment and before the XPS measurements. Interestingly, by comparing the results obtained by the XPS analysis for the as-prepared nanoparticles and after reduction treatment, it is possible to notice that the Cu-CeO_{2-x} (low TR) and Cu-CeO_{2-x} (high TR) nanoparticles present a smaller Ce(III) fraction after reduction treatment than the corresponding as-prepared nanoparticles. A possible explanation relies on the changes in the composition or morphology of the Cu-CeO_{2-x} nanoparticles during reduction treatment.

Table 5.9: Ce(III) fraction at the surface of the Cu-CeO_{2-x} nanoparticles obtained from the Ce 3d XPS spectra after reduction treatment. The typical uncertainty associated to the analysis is around 10% of the values obtained.

Sample	% Ce(III)
Cu-CeO_{2-x} (low TR)	11
Cu-CeO_{2-x} (high TR)	10
Cu-CeO_{2-x} (std)	09

Figure 5.17 presents the XPS measurements at the Cu $2p_{3/2}$ region after reduction treatment. It is possible to notice that all spectra present two components related to different oxidation states of the Cu atoms, as observed in the XPS measurements of the as-prepared samples. The chemical component with smaller binding energy at around 933 eV is related to the Cu(I) component, corresponding to the Cu-Cl bonding. The presence of Cl atoms after reduction treatment was observed in the Long Scan measurement as well (not shown here). This element might come from the NaCl compound, observed in the XRD measurements of the as-prepared nanoparticles, which decomposes around 1450 °C, then being stable at 400 °C. The Cu-Cl bonding occurs at the surface region since no Cu-Cl evidence is observed in the XANES spectra during reduction treatment. The other chemical component is related to Cu(II), which can be associated to the presence of CuO or $Cu(OH)_2$ compounds, both related to the exposure of the nanoparticles to the atmosphere. The quantification of the Cu compound fraction is presented in Table 5.10. It is possible to observe that the Cu nanoparticles present a high Cu(II) fraction. Also, it is observed that the Cu(I) fraction, related to the Cu-Cl bonding, is inversely proportional to the reactivity towards CO oxidation. This bonding decreases the number of Cu atoms available for the adsorption of the CO molecule during the CO oxidation reaction. Also, it is observed that all nanoparticles present a high amount of the Cu-O compound after exposition to the atmosphere at room temperature and the Cu(II) fraction obtained by XPS follows the same trend obtained by XANES during CO oxidation reaction at 250 °C. As observed in the XANES analysis, the CO oxidation reaction occurs by the adsorption of the CO molecule at the Cu(II) species [38]. The catalytic reaction occurs at the nanoparticle's surface, thus the XPS measurements confirm the XANES analysis.

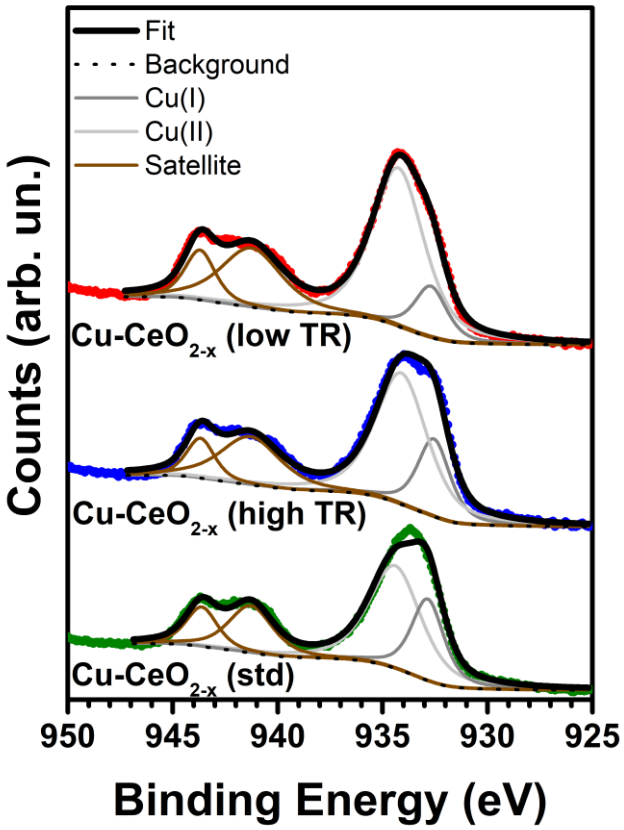

Figure 5.17: Cu $2p_{3/2}$ XPS spectra of the Cu-CeO_{2-x} (low TR), Cu-CeO_2.x (high TR) and Cu-CeO_2.x (std) nanoparticles after reduction treatment. The black points represent the Shirley background, the black solid line the fit obtained, the dark gray solid line the Cu(I) component, the light gray solid line the Cu(II) component and the brown solid line the Cu $2p_{3/2}$ satellites.

Table 5.10: Percentage of the chemical components used in the fitting of the Cu $2p_{3/2}$ XPS region for the Cu-CeO_{2-x} nanoparticles after reduction treatment.

	Cu(I)	**Cu(II)**
Cu-CeO_{2-x} (low TR)	17 %	83 %
Cu-CeO_{2-x} (high TR)	27 %	73 %
Cu-CeO_{2-x} (std)	33 %	67 %

In order to elucidate details about the atomic arrangement and the interaction between the Cu and CeO_{2-x} nanoparticles, the normalized intensity ratio of the Cu and Ce XPS signals was calculated. The ratio was obtained for two different probing depths by changing the kinetic energy of the photoelectrons that comes from different electronic levels (Cu 2p, Cu 3p, Ce 3d and Ce 4d) and are excited by the same photon energy. From the universal curve presented in Figure 3.11, it is possible to observe that

the inelastic mean free paths are $\lambda_{IMFP} \approx 11$ Å (photoelectrons from the Cu 2p and Ce 3d electronic levels), and $\lambda_{IMFP} \approx 22$ Å (photoelectrons from the Cu 3p and Ce 4d electronic levels). In order to compare the Cu/Ce atomic ratio at these probing depths, the intensities of the Cu 2p, Cu 3p, Ce 3d and Ce 4d XPS regions were normalized by the photoionization differential cross section values, obtained using Equation (3.10) and a theoretical database for the cross section values [104]. The photon flux and analyzer efficiency of detection were considered constant in all cases, thus were not considered in the calculation. Table 5.11 presents the Cu 2p/Ce 3d and Cu 3p/Ce 4d normalized ratios for the as-prepared and after reduction treatment nanoparticles.

Table 5.11: (Cu 2p)/(Ce 3d) ($\lambda_{IMFP} \approx 11$ Å) and (Cu 3p)/(Ce 4d) ($\lambda_{IMFP} \approx 22$ Å) normalized ratios obtained from the XPS measurements of the as-prepared and after reduction treatment Cu-CeO_{2-x} nanoparticles.

Sample	**As prepared**		**After reduction**	
	$\lambda_{IMFP} \approx 11$ Å	**$\lambda_{IMFP} \approx 22$ Å**	**$\lambda_{IMFP} \approx 11$ Å**	**$\lambda_{IMFP} \approx 22$ Å**
Cu-CeO_{2-x} (low TR)	2.21	1.70	3.73	2.36
Cu-CeO_{2-x} (high TR)	0.98	0.73	1.40	1.07
Cu-CeO_{2-x} (std)	1.19	0.70	2.16	1.10

The results presented in Table 5.11 show that in all cases, for a given probed depth, there is an increase of the Cu 2p/Ce 3d or Cu 3p/Ce 4d normalized ratio after reduction treatment in comparison to the corresponding as prepared case. It means there is a higher amount of Cu and/or a lower amount of Ce at the surface of the sample after reduction treatment. This increase of the Cu/Ce ratio after reduction treatment is related to the change of the Cu nanoparticles shape, which spreads over the CeO_{2-x} nanoparticles. Then, part of the CeO_{2-x} nanoparticles is now covered by the Cu nanoparticle spread over the CeO_{2-x} surface, then increasing the Cu 2p/Ce 3d and Cu 3p/Ce 4d normalized ratios after reduction treatment. It is confirmed by comparing the Cu/Ce normalized ratio at the two different depths probed for a given condition fixed. The increase of the probed depth (from $\lambda_{IMFP} \approx 11$ Å to $\lambda_{IMFP} \approx 22$ Å) gives a decrease on the Cu/Ce normalized ratio in all cases, then consistent with probing a higher amount of Ce atoms in a deeper region of the sample. In order to prove the proposed model, HRTEM with EDS linescan measurements were performed.

5.2.5 HRTEM measurements

Figure 5.18 (a) presents a typical HRTEM image of the Cu-CeO_{2-x} nanoparticles after reduction treatment, in this case for the Cu-CeO_{2-x} (std) nanoparticles. The Figure 5.18 (b) presents the EDS linescan that is obtained by scanning the red line region presented in Figure 5.18 (a). The EDS linescan is an EDS measurement mode where the electron beam moves through a determined line in the sample. In this way, it is possible to obtain chemical information through the linescan. It is possible to see that there is a Cu signal between 7.5 and 10 nm after the beginning of the arrow that represents the line where the EDS measurements were performed. This signal indicates the presence of a Cu nanoparticle in the region. The Ce signal observed in the same region indicates the presence of the CeO_{2-x} nanoparticle, probably behind the observed Cu nanoparticle. Figure 5.18 (c) was artificially colored in accordance to the elemental composition, obtained from the EDS linescan measurements. The blue and orange colors represent the CeO_{2-x} and Cu nanoparticles, respectively. It is possible to observe that the Cu nanoparticle does not show the sphere shape as shown in the as-prepared TEM images (Figure 5.1 (c)), but it spreads over the CeO_{2-x} nanoparticle presenting a flat surface. It means that Cu nanoparticles after reduction treatment cover a higher surface area of the CeO_{2-x} nanoparticles than in the as-prepared nanoparticles. This result is in accordance with the XPS measurements that showed an increase of the Cu 2p/Ce 3d and Cu 3p/ Ce 4d normalized ratios after reduction treatment, showing a decrease of the Ce signal at the surface region. It can be explained by the increase of the CeO_{2-x} area covered by the Cu nanoparticles. Also, it is possible to notice that the Cu nanoparticle is impregnated in the CeO_{2-x} support, which might occur due to the reduction temperature used. These factors change the interaction and contact area between the Cu and CeO_{2-x} nanoparticles, which explains the lower Ce(III) fraction observed by XPS in the Cu-CeO_{2-x} (low TR) and Cu-CeO_{2-x} (high TR) nanoparticles after the reduction treatment compared to the as-prepared nanoparticles. Since the interaction from the Cu-CeO_{2-x} interface is enhanced, the Ce(III) state changes to Ce(IV) state by the presence of O from CuO compound.

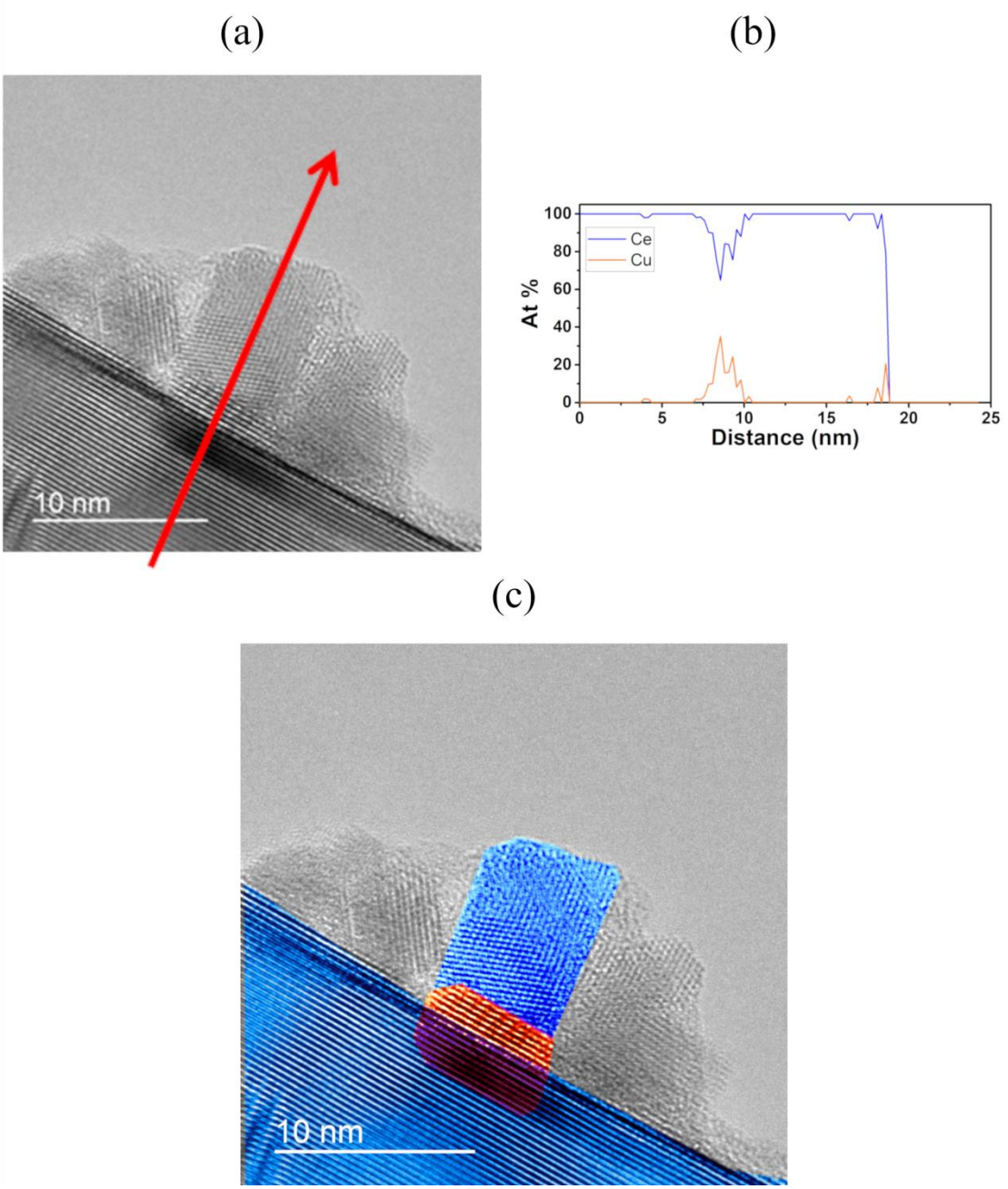

Figure 5.18: (a) HRTEM and (b) EDS linescan measurements performed in the Cu-CeO_{2-x} (std) nanoparticles after the reduction treatment under CO atmosphere for 30 min at 400 °C. The red arrow presented in (a) represent the line scan and direction of the EDS measurements. (c) Representation of the CeO_{2-x} nanoparticles, in blue, and Cu nanoparticle, in orange.

The change in the Cu morphology would be observed in the EXAFS measurements as a decrease in the coordination number of the Cu-Cu scattering path compared to the as-prepared sample, as observed in the literature for Ni/CeO_2 nanoparticles [101]. The authors used EXAFS measurements to study how the coordination number of the Ni-Ni scattering path changes with the different thermal treatments applied. The samples were exposed to H_2, CH_4 + H_2O and CH_4 + CO_2

atmosphere during heating to 750 °C and then cooled to room temperature. The authors concluded that the coordination number decreases with the reduction treatment at temperatures higher than 700 °C under a H_2 atmosphere. This decrease on the coordination number, when compared to the Ni/CeO_2 sample at 600°C, was attributed to the spread of the Ni nanoparticles over the CeO_2 nanoparticles. In this work the fitting procedure of the EXAFS oscillations of the as-prepared Cu-CeO_{2-x} nanoparticles was not performed due to the complex initial mixture of Cu-Cl, $Cu(OH)_2$ and CuO compounds. The comparison of the coordination numbers between the samples should be performed with the same compounds present, like the Ni(0) [101]. In spite of this, the Cu-CeO_{2-x} (std) presents the lowest coordination number for the Cu-Cu scattering path between the nanoparticles, indicating that this sample would present the highest amount of Cu nanoparticles spread over CeO_{2-x}, while the other two nanoparticles present a similar coordination number for the Cu-Cu scattering path. In previous works from the group, it was observed that changing the metallic nanoparticle from Ni to Cu [53] or changing the surface composition of the bimetallic Cu-Ni nanoparticle [54] influences on the metal-oxide interaction. The same factors may influence on the spreading of the metallic nanoparticles over the oxide, since the effect is also somehow related to a metal-oxide interaction.

5.3 Atomic model for the CO oxidation reaction of Cu-CeO_{2-x} nanoparticles

The results obtained from the Mass Spectrometry measurements during the CO oxidation reaction at 250 ºC show that the highest reactivity occurs for the Cu-CeO_{2-x} (low TR) nanoparticles. These nanoparticles present the highest Ce(III) fraction after reduction treatment. The XANES measurements at the Ce L_3 edge showed that the Ce(III) fraction after reduction treatment follows the same trend as the reactivity of the samples at 250 °C, showing that a high Ce(III) fraction is directly related to the reactivity towards CO oxidation reaction of the nanoparticles. It occurs because these nanoparticles have an improved redox capacity, which is essential for the CO oxidation reaction takes place. Also, it is observed that during the CO oxidation reaction at 250 °C, all Cu-CeO_{2-x} nanoparticles presented the same Ce(III) fraction, showing that the CeO_{2-x} nanoparticles oxidize after exposure to the O_2 present in the atmosphere during

the CO oxidation reaction.

The *in situ* XANES measurements at the Cu K edge at 250 °C shows that the CuO amount during CO oxidation reaction is directly related to the reactivity of the nanoparticles, then indicating that the CO oxidation reaction occurs following the Mechanism I presented in Section 2.5. In this mechanism, the CO molecule is adsorbed in the Cu(II) specie, and the O for the CO oxidation reaction is given to the CO molecule by the Cu nanoparticle, reducing the Cu(II) species to Cu(I). Then the support transfer O atoms to re-oxidize the Cu nanoparticles and an improved redox property of the support allows the mechanism to occur. The support is re-oxidized by the O_2 molecules present in the CO oxidation reaction atmosphere. These atomic events are associated to a change on the local atomic order around Cu atoms, then influencing on the reactivity towards CO oxidation reaction. The local atomic order around Cu atoms during CO oxidation reaction plays an important role on the reactivity results. It was observed an indicative that a higher coordination number and smaller Debye-Waller factor related to the Cu-O and Cu-Cu scattering paths, besides shorter distances related to the Cu-O scattering path increase the reactivity of the nanoparticles.

On the other hand, in the CO oxidation reaction at 150 °C, it was observed the highest reactivity for the Cu-CeO_{2-x} (high TR) nanoparticles. Before the CO oxidation reaction at 150 °C, all nanoparticles present the same Ce(III) fraction observed before the reaction at 250 °C. However, the Cu-CeO_{2-x} (high TR) nanoparticles presented the smaller Ce(III) fraction during reaction at 150 °C, similar to the fraction present during the reaction at 250 °C. On the other hand, at 150 °C none of the nanoparticles present a significant amount of the CuO compound and the difference in the reactivity towards CO oxidation reaction is related only to the oxidation state of the CeO_{2-x} nanoparticles during reaction. The results show that there is an optimal O vacancy population for the CeO_{2-x} during the CO oxidation reaction, as proposed theoretically in [33].

In this way, there are four key factors that influence on the reactivity towards the CO oxidation reaction: (i) CuO fraction during reaction, (ii) Ce(III) fraction before reaction, (iii) local atomic order around Cu atoms during reaction and (iv) Ce(III) fraction during reaction. The (i), (ii) and (iii) factors were discovered analyzing the data at 250 ^{o}C, where the Ce(III) fraction is constant during reaction, and the factor (iv) was obtained analyzing the data at 150 °C where the CuO fraction is constant during

reaction.

The Mass Spectrometry measurements of the Cu-CeO_{2-x} (high TR) and CeO_{2-x} (high TR) nanoparticles indicate that the interaction between the Cu and CeO_{2-x} nanoparticles increases the reactivity of the Cu-CeO_{2-x} samples towards the CO oxidation reaction. Moreover, this interaction influences on the oxidation state of the Cu and CeO_{2-x} nanoparticles during the reduction treatment and the CO oxidation reaction. Also, the oxidation state of the Cu nanoparticles changes with the CeO_{2-x} nanoparticle used. The results obtained indicate that the reactivity of the nanoparticles for the CO oxidation reaction increases for the CeO_{2-x} nanoparticles synthesized in comparison to the CeO_{2-x} commercial standard. Besides this, the O vacancy population in the CeO_{2-x} nanoparticles is directly related to the reactivity observed in the nanoparticles and this parameter is easily controlled by the synthesis of the nanoparticles and the temperature used during the CO reduction treatment [34]. In this way, it was possible to control the reactivity of Cu-CeO_{2-x} nanoparticles by changing the parameters used in the CeO_{2-x} nanoparticles synthesis.

6. CONCLUSIONS AND PERSPECTIVES

The main goal of the present work was to study the influence of the electronic and structural properties of the CeO_{2-x} nanoparticles on the reactivity of systems containing Cu-CeO_{2-x} nanoparticles in the CO oxidation reaction. The higher reactivity of the Cu-CeO_{2-x} nanoparticles in the CO oxidation reaction the higher the O vacancy population during the reduction treatment (before the CO oxidation reaction). Moreover, the improved reactivity occurs also for small Ce(III) fractions (around 5%) during the CO oxidation reaction. The reactivity is directly related to a higher CuO fraction, Cu-O and Cu-Cu coordination numbers and Debye-Waller factors and shorter Cu-O distances. It was demonstrated that the atomic mechanism of the CO oxidation reaction with Cu-CeO_{2-x} nanoparticles occurs following the Mechanism I presented in Section 2.5, where there is the adsorption of the CO molecule on the Cu(II) species. The Cu(II) specie is responsible for providing the O atom to the CO molecule, then forming CO_2. The CO_2 molecule is then desorbed from the Cu nanoparticle's surface, reducing it from Cu(II) to Cu(I). The re-oxidation of the Cu nanoparticles occurs with the O given by the CeO_{2-x} nanoparticles. The O that participates of the re-oxidation of the Cu nanoparticles is the O ion present in the CeO_{2-x} lattice.

Finally, the Cu-CeO_{2-x} nanoparticles containing the synthesized CeO_{2-x} nanoparticles present higher reactivity in the CO oxidation reaction than nanoparticles containing the CeO_{2-x} commercial standard at both 250 °C and 150 °C. It is important to stress out that the temperatures used in the present study are smaller than those typically observed in the literature. It means there is no need of high temperatures to create O vacancies in CeO_{2-x} whether the nanoparticles synthesized in the present study are used. It is different of using CeO_2 standard that reduces at very high temperatures (higher than 800 ^{o}C). It was observed that the electronic and morphological properties of the CeO_{2-x} nanoparticles influence directly on the reactivity of the Cu-CeO_{2-x} nanoparticles towards CO oxidation reaction. Thus the Cu-CeO_{2-x} nanoparticles can be optimized for the CO oxidation reaction by tuning the CeO_{2-x} nanoparticle's properties.

Future perspectives for this study include the catalytic activity measurements during the CO oxidation reaction and the TEM measurements after thermal treatment, allowing to study a possible Cu sintering process due to the temperatures used.

BIBLIOGRAPHY

[1] World Health Organization, Regional Office for Europe, Air quality guidelines for Europe, 2nd ed., Copenhagen: WHO Regional Office for Europe., 2000.

[2] K. Sircar, J. Clower, M. k. Shin, C. Bailey, M. King and F. Yip, "Carbon monoxide poisoning deaths in the United States, 1999 to 2012," *The American journal of emergency medicine,* vol. 33, no. 9, pp. 1140-1145, 2015.

[3] S. Omaye, "Metabolic Modulation of Carbon Monoxide Toxicity," *Toxicology,* vol. 180, pp. 139-150, 2002.

[4] World Health Organization (WHO), Regional Office for Europe, WHO guidelines for indoor air quality: selected pollutants, Copenhagen, 2010.

[5] D. J. Jacob, Introduction to Atmospheric Chemistry, Princeton University Press, 1999.

[6] P. Novelli, K. Masarie, P. Tans and P. Lang, "Recent Changes in Atmospheric Carbon Monoxide," *Science,* vol. 263, no. 5153, pp. 1587-1590, 1994.

[7] T. Holloway, H. Levy II and K. Prasad, "Global distribution of carbon monoxide," *Journal of Geophysical Research: Atmospheres,* vol. 105, no. D10, pp. 12123-12147, 2000.

[8] United States Environmental Protection Agency (EPA), "Understanding Global Warming Potentials," [Online]. Available: https://www.epa.gov/ghgemissions/understanding-global-warming-potentials. [Accessed 13 01 2020].

[9] Brasil, *Lei nº 8.723 de 28 de outubro de 1993. Dispõe sobre a redução de emissão de poluentes por veículos automotores e dá outras providências.*, Diário Oficial da União, 29 de outubro de 1993..

[10] União Européia , *Diretiva 2010/75/EU do Parlamento Europeu e do Conselho de 24 de novembro de 2010. Relativa às emissões industriais (prevenção e controle integrados da poluição).,* Jornal Oficial da União Europeia, 17 de dezembro de 2010..

[11] Brasil, *Resolução/CONAMA nº 003 de 28 de junho de 1990,* Diário Oficial da União, 22 de agosto de 1990, Seção I.

[12] União Européia, *Diretiva 2008/50/CE do Parlamento Europeu e do Conselho de 21 de maio de 2008. Relativa a qualidade do ar ambiente e a um ar mais limpo na Europa.,* Jornal Oficial da União Europeia, 11 de junho de 2008..

[13] Cestesb - Companhia Ambiental do Estado de São Paulo, "Relatório das Emissões Veiculares no Estado de São Paulo (2017)," 2018. [Online]. Available: https://cetesb.sp.gov.br/veicular/relatorios-e-publicacoes/. [Accessed 10 08 2019].

[14] K. N. Rao, P. Bharali, G. Thrimirthulu and B. Reddy, "Supported copper-ceria catalysts for low temperature CO oxidation.," *Catalysis Communications,* vol. 11, pp. 863-866, 2010.

[15] G. Rothenberg, Catalysis, Concepts and Green Aplications, John Wiley & Sons, 2015.

[16] M. E. Davis and R. J. Davis, Fundamentals of chemical reaction engineering, McGraw-Hill Higher Education, 2003.

[17] W. D. Callister Jr. and D. G. Rethwisch, Materials Science and Engineering: An Introduction, 8ª ed., John Wiley & Sons, 2009.

[18] J. Kaspar, P. Fornasiero and N. Hickey, "Automotive catalytic converters: current status and some perspectives," *Catalysis Today,* vol. 77, pp. 419-449, 2003.

[19] J. Hromádko, P. Miler, J. Hromádko, V. Hönig and M. Schwarzkopf, "The influence of three-way catalysts on harmful emission production," *Transportation Research Part D,* vol. 15, pp. 103-107, 2010.

[20] R. M. Heck and R. J. Farrauto, "Automobile exhaust catalysts," *Applied Catalysis A: General,* vol. 221, pp. 443-457, 2001.

[21] J. Kubsh, "Advanced Three-Way Catalyst Technology," MECA, [Online]. Available: http://www.meca.org/resources/featured-article. [Accessed 07 09 2019].

[22] Ş. C. Bobaru, "High-pressure STM studies of oxidation catalysis.," PHD Thesis, Faculty of Mathematics and Natural Sciences, Leiden University, 2006.

[23] L. A. Petrov, "Gold based environmental catalyst.," *Studies in Surface Science and*

Catalysis, vol. 130, pp. 2345-2350, 2000.

[24] F. Gao, S. Mcclure, Y. Cai, K. Gath, Y. Wang, M. Chen, Q. Guo and D. Goodman, "CO oxidation trends on Pt-group metals from ultrahigh vacuum to near atmospheric pressures: A combined in situ PM-IRAS and reaction kinetics study," *Surface Science,* vol. 603, pp. 65-70, 2009.

[25] T. Montini, M. Melchionna, M. Monai and P. Fornasiero, "Fundamentals and Catalytic Applications of CeO2-Based Materials," *Chemical reviews,* vol. 116, no. 10, pp. 5987-6041, 2016.

[26] G. Kim, "Ceria-Promoted Three-Way Catalysts for Auto Exhaust Emission Control," *Industrial & Engineering Chemistry Product Research and Development,* vol. 21, no. 2, pp. 267-274, 1982.

[27] E. Murray, T. Tsau and S. Barnett, "A Direct-Methane Fuel Cell with a Ceria-Based Anode," *Nature,* vol. 400, pp. 649-651, 1999.

[28] B. Choudhury and A. Choudhury, "Ce3+ and Oxygen Vacancy Mediated Tuning of Structural and Optical Properties of CeO2 Nanoparticles.," *Materials, Chemistry and Physics,* vol. 131, pp. 666-671, 2012.

[29] A. Trovarelli, "Catalytic Properties of Ceria and CeO2-Containing Materials," *Catalysis Review,* vol. 38, no. 4, pp. 439-520, 1996.

[30] S. Carrettin, P. Concepción, A. Corma, J. M. Lopez Nieto and V. F. Puntes, "Nanocrystalline CeO2 increases the activity of Au for CO oxidation by two orders of magnitude.," *Angewandte Chemie International Edition,* vol. 43, no. 19, pp. 2538-2540, 2004.

[31] C. Sun, H. Liab and L. Chenab, "Nanostructured ceria-based materials: synthesis, properties, and applications," *Energy & Enviromental Science,* vol. 5, pp. 8475-8505, 2012.

[32] M. Breysse, M. Guenin, B. Claudel and J. Veron, "Catalysis of Carbon Monoxide Oxidation by Cerium Dioxide: II. Microcalorimetric Investigation of Adsorption and Catalysis.," *Journal of Catalysis,* vol. 28, pp. 54-62, 1973.

[33] T. X. T. Sayle, F. Caddeo, X. Zhang, T. Sakthivel and S. Das, "Structure−Activity Map of Ceria Nanoparticles, Nanocubes, and Mesoporous Architectures," *Chemistry of Materials,* vol. 28, pp. 7287-7295, 2016.

[34] G. B. Della Mea, L. P. Matte, A. S. Thill, F. O. Lobato, E. V. Benvenutti, L. T. Arenas, A. Jürgensen, R. Hergenröder, F. S. Poletto and F. Bernardi, "Tuning the oxygen vacancy population of cerium oxide (CeO2-x, 0 < x < 0.5) nanoparticles," *Applied Surface Science*, vol. 422, pp. 1102-1112, 2017.

[35] M. Cargnello, V. Doan-Nguyen, T. Gordon, R. Diaz, E. Stach, G. Raymond, P. Fornasiero and C. Murray, "Control of metal nanocrystal size reveals metal-support interface role for ceria catalysts.," *Science,* vol. 341, no. 6147, pp. 771-773, 2013.

[36] A. P. Jia, S. Y. Jiang, J. Q. Lu and M. F. Luo, "Study of catalytic activity at the CuO− CeO2 interface for CO oxidation," *The Journal of Physical Chemistry C,* vol. 114, no. 19, pp. 21605-61610, 2010.

[37] S. Zeng, Y. Wang, S. Ding, J. J. H. B. Sattler, E. Borodina, L. Zhang, B. M. Weckhuysen and H. Su, "Active sites over CuO/CeO2 and inverse CeO2/CuO catalysts for preferential CO oxidation," *Journal of Power Sources,* vol. 256, pp. 301-311, 2014.

[38] M. Moreno, L. Bergamini, G. T. Baronetti, M. A. Laborde and F. J. Mariño, "Mechanism of CO oxidation over CuO/CeO2 catalysts," *International journal of hydrogen energy,* vol. 35, no. 11, pp. 5918-5924, 2010.

[39] S. Yao, K. Mudiyanselage, W. Xu, A. Johnston-Peck, J. Hanson, T. Wu, D. Stacchiola, J. A. Rodriguez, H. Zhao, K. A. Beyer, K. W. Chapman, P. J. Chupas, A. Martínes-Arias, R. Si, T. B. Bolin, W. Liu and S. D. Senanayake, "Unraveling the dynamic nature of a CuO/CeO2 catalyst for CO oxidation in operando: a combined study of XANES (fluorescence) and DRIFTS.," *ACS Catalysis,* vol. 4, no. 6, pp. 1650-1661, 2014.

[40] F. Wang, R. Büchel, A. Savitsky, M. Zalibera, D. Widmann, S. E. Pratsinis, W. Lubitz and F. Schüth, "In situ EPR study of the redox properties of CuO–CeO2 catalysts for preferential CO oxidation (PROX).," *ACS Catalysis,* vol. 6, no. 6, pp. 3520-3530, 2016.

[41] P. G. Harrison, I. K. Ball, W. Azelee, W. Daniell and D. Goldfarb, "Nature and Surface Redox Properties of Copper(II)-Promoted Cerium(IV) Oxide CO-Oxidation Catalysts," *Chemistry of materials,* vol. 12, no. 12, pp. 3715-3725, 2000.

[42] M. Lykaki, E. Pachatouridou, S. A. C. Carabineiro, E. Iliopouloub, C. Andriopoulou, N. Kallithrakas-Kontos, S. Boghosian and M. Konsolakis, "Ceria nanoparticles shape effects on the structural defects and surface chemistry:

Implications in CO oxidation by Cu/CeO2 catalysts.," *Applied Catalysis B: Environmental,* vol. 230, pp. 18-28, 2018.

[43] A. Martínez-Arias, D. Gamatta, M. Fernández-García, X. Wang, J. Hanson and J. Rodriguez, "Comparative study on redox properties of nanosized CeO2 and CuO/CeO2 under CO/O2," *Journal of Catalysis,* vol. 240, pp. 1-7, 2006.

[44] M. Konsolakis, "The role of Copper-Ceria interactions in catalysis science: recent theoretical and experimental advances," *Applied Catalysis B: Enviromental,* vol. 198, pp. 49-66, 2016.

[45] C. Maciel, T. F. Silva, M. I. Hirooka, M. N. Belgacem and J. M. Assaf, "Effect of nature of ceria support in CuO/CeO2 catalyst for PROX-CO reaction," *Fuel,* vol. 97, pp. 245-252, 2012.

[46] X. Tang, B. Zhang, Y. Li, Y. Xu, Q. Xin and W. Shen, "Carbon monoxide oxidation over CuO/CeO2 catalysts.," *Catalysis Today,* vol. 93, pp. 191-198, 2004.

[47] X. Zhang, X. Zhang, L. Song, F. Hou, Y. Yang, Y. Wang and N. Liu, "Enhanced catalytic performance for CO oxidation and preferential CO oxidation over CuO/CeO2 catalysts synthesized from metal organic framework: effects of preparation methods.," *International Journal of Hydrogen Energy,* vol. 43, no. 39, pp. 18279-18288, 2018.

[48] C. Lu, W. Chang and M. Wey, "CuO/CeO2 catalysts prepared with different cerium supports for CO oxidation at low temperature," *Materials Chemistry and Physics,* vol. 141, pp. 512-518, 2013.

[49] A. Martınez-Arias, M. Fernández-Garcıa, O. Gálvez, J. M. Coronado, J. A. Anderson, J. C. Conesa, J. Soria and G. Mubuera, "Comparative Study on Redox Properties and Catalytic Behavior for CO Oxidation of CuO/CeO2 and CuO/ZrCeO4 Catalysts," *Journal of Catalysis,* vol. 195, no. 1, pp. 207-216, 2000.

[50] A. S. Thill, A. S. Kilian and F. Bernardi, "Key role played by metallic nanoparticles on the ceria reduction," *The Journal of Physical Chemistry C,* vol. 121, no. 45, pp. 25323-25332, 2017.

[51] S. J. Tauster, "Strong Metal-Support Interactions," *Accounts of Chemical Research,* vol. 20, no. 11, pp. 389-394, 1987.

[52] S. Bernal, J. Calvino, M. Cauqui, J. Gatica, C. Cartes, J. Omil and J. Pintado, "Some

contributions of electron microscopy to the characterisation of the strong metal–support interaction effect," *Catalysis Today,* vol. 77, no. 4, pp. 385-406, 2003.

[53] L. Matte, A. Kilian, L. Luza, M. Alves, J. Morais, D. Baptista, J. Dupont and F. Bernardi, "Influence of the CeO2 Support on the Reduction Properties of Cu/CeO2 and Ni/CeO2 Nanoparticles," *The Journal of Physical Chemistry C,* vol. 45, pp. 26459-26470, 2015.

[54] W. T. Figueiredo, G. Basso Della Mea, M. Segala, D. L. Baptista, C. Escudero, V. Pérez-Dieste and F. Bernardi, "Understanding the Strong Metal-Support Interaction (SMSI) Effect in CuxNi1-x/CeO2 (0< x< 1) Nanoparticles for Enhanced Catalysis.," *ACS Applied Nano Materials.,* vol. 2, no. 4, pp. 2559-2573, 2019.

[55] W. T. Figueiredo, "Elucidation of catalytic events at atomic level in CuxNi1-x/CeO2 (0 < x < 1) nanoparticles applied to the reverse water-gas shift (RWGS) reaction," Master Dissertation, Instituto de Física, UFRGS, Porto Alegre, 2017.

[56] A. Martinez-Arias, A. B. Hungria, M. Fernandez-Garcia and J. C. a. M. G. Conesa, "Interfacial Redox Processes under CO/O2 in a Nanoceria-Supported Copper Oxide Catalystnterfacial Redox Processes under CO/O2 in a Nanoceria-Supported Copper Oxide Catalyst," *Journal of Physical Chemistry B,* vol. 108, pp. 17983-17991, 2004.

[57] Y. Xie, J. Wu, G. Jing, H. Zhang, S. Zeng, X. Tian, X. Zou, J. Wen, H. Su, C. Zhong and P. Cui, "Structural origin of high catalytic activity for preferential CO oxidation over CuO/CeO2 nanocatalysts with different shapes," *Applied Catalysis B: Environmental,* vol. 239, pp. 665-676, 2018.

[58] D. Williams and C. Carter, Transmission Electron Microscopy, Second Edition ed., vol. Part 1: Basics, Springer, 2000.

[59] "How Are Light Microscopes And Electron Microscopes Similar," [Online]. Available: http://infoupdate.org/how-are-light-microscopes-and-electron-microscopes-similar/. [Accessed 12 05 2019].

[60] R. Egerton, Physical Principles of Electrons Microscopy, Springer, 2005.

[61] T. Wen and K. Krishnan, "Thermal Stability and Morphological Transformations of Au core−Co shell Nanocrucibles," *J. Phys. Chem. C,* vol. 114, pp. 14838-14842, 2010.

[62] L. Reimer and H. Kohl, Transmission Electron Microscopy: physics of image

formation., 5ª ed., Springer, 2008.

[63] "Bragg's Law," [Online]. Available: http://hyperphysics.phy-astr.gsu.edu/hbase/quantum/bragg.html. [Accessed 10 05 2019].

[64] B. B. He, Two-Dimensional X-Ray Diffaction, Hoboken, New Jersey : John Wiley & Sons, Inc, 1954.

[65] B. D. Cullity, Elements of X-Ray Diffraction, 2ª ed., Addison-Wesley Publishing Company Inc, 1978.

[66] Charles University: Surface Physics Group, "XPS: Principles of photoemission spectroscopy," [Online]. Available: https://physics.mff.cuni.cz/kfpp/povrchy/method/xps-ma. [Accessed 26 09 2019].

[67] C. D. Wagner, W. M. Riggs, L. E. Davis, J. F. Moulder and G. E. Muilenberg, Handbook of X-ray Photoelectron Spectroscopy, Eden Prairie, MN: Perkin-Elmer Corporation, 1979.

[68] J. W. Niemantsverdriet, Spectroscopy in catalysis: an introduction, 3ª ed., John Wiley & Sons, 2007, pp. 39-59.

[69] C. R. Brundler and A. D. Baker, Electron Spectroscopy: Theory, Techniques and Application, Academic Press, 1977.

[70] J. F. Watts and J. Wolstenholme, An Introduction to Surface Analysis by XPS and AES, Wiley, 2003.

[71] "State Physics at the Friedrich-Alexander-University Erlangen-Nuremberg," [Online]. Available: https://www.fkp.uni-erlangen.de/methoden/2ppetutor/setup.html. [Accessed 20 05 2019].

[72] W. E. Wallace, "NIST Chemistry WebBook, NIST Standard Reference Database Number 69,," National Institute of Standards and Technology, [Online]. Available: https://webbook.nist.gov/cgi/cbook.cgi?ID=C124389&Units=SI&Mask=200#Notes. [Accessed 07 05 2019].

[73] E. Hoffmann and V. Stroobant, Mass Spectrometry: principles and application, 3ª ed., Wiley, 2007.

[74] "How it Works: From Blood Sample to Results," Hemavault Labs, 21 08 2014.

[Online]. Available: https://labdothemavudotcom.wordpress.com/2014/08/21/how-it-works-from-blood-sample-to-results/. [Accessed 10 05 2019].

[75] P. Willmott, An Introduction to Synchrotron Radiation: Techniques and Applications, John Wiley & Sons, 2011.

[76] J. Als-Nielsen and D. Des McMorrow, Elements of modern X-ray physics., John Wiley & Sons, 2011.

[77] J. Cezar, N. Souza-Neto, C. Piamonteze, E. Tamura, F. Gárcia, E. Carvalho, R. Neueschwander, A. Ramos, H. Tolentino, A. Carneiro, N. Massa, M. Martinez-Lope, J. Alonso and J. Itié, "Energy-dispersive X-ray absorption spectroscopy at LNLS: investigation on strongly correlated metal oxie," *Journal of Synchrotron Radiation,* vol. 17, pp. 93-102, 2010.

[78] J. Rehr and R. Albers, "Theoretical Approaches to X-Ray Absorption Fine Structure," *Revies of Modern Physics,* vol. 3, pp. 621-654, 2000.

[79] D. Koningsberger, B. Mojet, G. van Dorssen and D. Ramaker, "XAFS spectroscopy: Fundamental Principles and Data Analysis," *Topics in Catalysis,* pp. 143-155, 2000.

[80] D. E. Sayers, E. A. Stern and a. F. W. Lytle, "New technique for investigating noncrystalline structures: Fourier analysis of the extended x-ray—absorption fine structure.," *Physical review letters,* vol. 27, no. 18, p. 1204, 1971.

[81] B. Ravel, "A practical introduction to multiple scattering theory," *Journal of Alloys and Compounds,* vol. 401, p. 118–126, 2005.

[82] G. Bergerhoff, I. D. Brown and I. D. Allen, "Crystallographic databases.," *International Union of Crystallography,* vol. 360, pp. 77-95, 1987.

[83] J. Rodriguez-Carvajal, "FullProof Program," 1998. [Online]. Available: http://www.ill.eu/sites/fullprof.

[84] P. Thompson, D. E. Cox and J. B. Hastings, "Rietveld refinement of Debye–Scherrer synchrotron X-ray data from Al2O3..].," *Journal of Applied Crystallography,* vol. 20, no. 2, p. 79– 83, 1987.

[85] K.-D. Schierbaum, "Ordered ultra-thin cerium oxide overlayers on Pt (111) single crystal surfaces studied by LEED and XPS.," *Surface Science,* vol. 399, no. 1, pp.

29-38, 1998.

[86] P. Burroughs, A. Hamnett, A. F. Orchard and G. Thornton, "Satellite structure in the X-ray photoelectron spectra of some binary and mixed oxides of lanthanum and cerium," *Journal of the Chemical Society,* vol. 17, pp. 1686-1698, 1976.

[87] B. Ravel and M. Newville, "ATHENA, ARTEMIS, HEPHAESTUS: data analysis for X-ray absorption spectroscopy using IFEFFIT," *Journal of Synchrotron Radiation,* vol. 12, pp. 537-541, 2005.

[88] Y. Takahashi, H. Sakami and M. Nomura, " Determination of the oxidation state of cerium in rocks by Ce LIII-edge X-ray absorption near-edge structure spectroscopy.," *Analytica Chimica Acta,* vol. 468, no. 2, pp. 345-354, 2002.

[89] S. J. A. Figueroa, J. C. Mauricio, J. Murari, D. B. Beniz, J. R. Piton, H. H. Slepicka, M. F. d. Sousa, A. M. Espídola and A. P. S. Levinsky, "Upgrades to the XAFS2 beamline control system and to the endstation at the LNLS," *Journal of Physics: Conference Series,* vol. 712, no. 1, p. 012022, 2016.

[90] M. Breintbach, D. Bathen and H. Shmidt-Traub, "Effect of Ultrasound on Adsorption and Desorption Processes," *Ind. Eng. Chem. Res,* vol. 42, pp. 5635-5646, 2003.

[91] S. Rege, R. Yang and C. Cain, "Desorption by Ultrasound: Phenol on Activated Carbin and Polymeric Resin," *AICHE Journal,* vol. 44, no. 7, pp. 1519-1528, 1998.

[92] S. Deshpande, S. Patil, S. V. N. T. Kuchibhatla and S. Seal, "Size dependency variation in lattice parameter and valency states in nanocrystalline cerium oxide," *Applied Physics Letters,* vol. 87, no. 13, p. 133113, 2005.

[93] M. Mogensen, N. Sammes and G. Tompsett, "Physical, chemical and electrochemical properties of pure and doped ceria," *Solid State Ionics,* no. 129, pp. 63-94, 1999.

[94] S. Tanuma, C. J. Powell and D. R. Penn, "Calculations of electron inelastic mean free paths. V. Data for 14 organic compounds over the 50–2000 eV range.," *Surface and interface analysis,* vol. 21, no. 3, pp. 165-176, 1994.

[95] R. P. Vesquez, "CuCl by XPS," *Surface Sciene Spectra,* vol. 2, no. 2, pp. 138-143, 1993.

[96] R. P. Velasquez, "CuO by XPS," *Surface Science Spectra,* vol. 5, no. 4, pp. 262-266, 1998.

[97] R. P. Velasquez, "Cu(OH)2 by XPS," *Surface Science Spectra,* vol. 5, no. 4, pp. 267-272, 1998.

[98] H. Zhu, "Sintering processes of two nanoparticles: a study by molecular dynamics simulations.," *Philosophical Magazine Letters,* vol. 73, no. 1, pp. 27-33, 1996.

[99] X. Wang, J. C. Hanson, A. I. Frenkel, J. Y. Kim and J. A. Rodriguez, "Time-resolved Studies for the Mechanism of Reduction of Copper Oxides with Carbon Monoxide: Complex Behavior of Lattice Oxygen and the Formation of Suboxide," *The Journal of Physical Chemistry B,* vol. 108, pp. 13667-13673, 2004.

[100] A. Maubert, G. A. Martin, H. Praliaud and P. Turlier, "CeO2-supported nickel catalysts. Evidence of a strong metal-support ineraction," *Reaction Kinetics and Catalysis Letters,* vol. 24, no. 1-2, pp. 183-186, 1984.

[101] V. M. Gonzalez-DelaCruz, J. P. Holgado, R. Pereñíguez and A. Caballero, "Morphology changes induced by strong metal–support interaction on a Ni–ceria catalytic system.," *Journal of Catalysis,* vol. 257, no. 2, pp. 307-314, 2008.

[102] A. M. Beale and B. M. Weckhuysen, "EXAFS as a tool to interrogate the size and shape of mono and bimetallic catalyst nanoparticles.," *Physical Chemistry Chemical Physics* , vol. 12, no. 21, pp. 5562-5574, 2010.

[103] P. C. Caldas, J. M. R. Gallo, A. Lopez-Castillo, D. Zanchet and J. M. C. Bueno, "The structure of the Cu–CuO sites determines the catalytic activity of cu nanoparticles," *ACS Catalysis,* vol. 7, no. 4, pp. 2419-2424, 2017.

[104] J. Yeh and I. Lindau, "Atomic subshell photoionization cross sections and asymmetry parameters: 1⩽ Z⩽ 103," *Atomic data and nuclear data tables,* vol. 32, no. 1, pp. 1-155, 1985.